

Key Points:

- Pervasive folding in shale-rich orogen interior differs from typical fold-thrust system in thick-bedded accreted strata of the Vandam Zone
- Atypical negative thermochronometric age-elevation relationships explained as a product of fold limb rotation using novel modeling method
- Thermochronometric evidence for out-of-sequence deformation in orogen interior after Vandam Zone accretion, maintaining critical taper

Supporting Information:

Supporting Information may be found in the online version of this article.

Correspondence to:

A. R. Tye,
alex.tye@utahtech.edu

Citation:

Tye, A. R., Niemi, N. A., Cowgill, E., Kadirov, F. A., & Babayev, G. R. (2022). Diverse deformation mechanisms and lithologic controls in an active orogenic wedge: Structural geology and thermochronometry of the eastern Greater Caucasus. *Tectonics*, *41*, e2022TC007349. <https://doi.org/10.1029/2022TC007349>

Received 11 APR 2022

Accepted 7 NOV 2022

Author Contributions:

Conceptualization: A. R. Tye, N. A. Niemi, E. Cowgill

Data curation: A. R. Tye, N. A. Niemi

Funding acquisition: A. R. Tye, N. A. Niemi

Investigation: A. R. Tye, N. A. Niemi, E. Cowgill

Methodology: A. R. Tye, N. A. Niemi

Resources: N. A. Niemi, F. A. Kadirov, G. R. Babayev

Software: A. R. Tye

Supervision: N. A. Niemi, E. Cowgill

Visualization: A. R. Tye

Writing—original draft: A. R. Tye

Writing—review and editing: A. R. Tye, N. A. Niemi, E. Cowgill

© 2022 The Authors.

This is an open access article under the terms of the [Creative Commons Attribution-NonCommercial License](#), which permits use, distribution and reproduction in any medium, provided the original work is properly cited and is not used for commercial purposes.

Diverse Deformation Mechanisms and Lithologic Controls in an Active Orogenic Wedge: Structural Geology and Thermochronometry of the Eastern Greater Caucasus

A. R. Tye^{1,2} , N. A. Niemi¹ , E. Cowgill³ , F. A. Kadirov⁴ , and G. R. Babayev⁴ 

¹Department of Earth and Environmental Sciences, University of Michigan, Ann Arbor, MI, USA, ²Now at Department of Earth and Environmental Sciences, Utah Tech University, St. George, UT, USA, ³Department of Earth & Planetary Sciences, University of California, Davis, CA, USA, ⁴Institute of Geology and Geophysics, Azerbaijan National Academy of Sciences, Baku, Azerbaijan

Abstract Orogenic wedges are common at convergent plate margins and deform internally to maintain a self-similar geometry during growth. New structural mapping and thermochronometry data illustrate that the eastern Greater Caucasus mountain range of western Asia undergoes deformation via distinct mechanisms that correspond with contrasting lithologies of two sedimentary rock packages within the orogen. The orogen interior comprises a package of Mesozoic thin-bedded (<10 cm) sandstones and shales. These strata are deformed throughout by short-wavelength (<1 km) folds that are not fault-bend or fault-propagation folds. In contrast, a coeval package of thick-bedded (up to 5 m) volcanoclastic sandstone and carbonate, known as the Vandam Zone, has been accreted and is deformed via imbrication of coherent thrust sheets forming fault-related folds of 5–10 km wavelength. Structural reconstructions and thermochronometric data indicate that the Vandam Zone package was accreted between ca. 13 and 3 Ma. Following Vandam Zone accretion, thermal modeling of thermochronometric data indicates rapid exhumation (~0.3–1 mm/yr) in the wedge interior beginning between ca. 6 and 3 Ma, and a novel thermochronometric paleo-rotation analysis suggests out-of-sequence folding of wedge-interior strata after ca. 3 Ma. Field relationships suggest that the Vandam Zone underwent syn-convergent extension following accretion. Together, the data record spatially and temporally variable deformation, dependent on both the mechanical properties of deforming lithologies and perturbations such as accretion of material from the down-going to the overriding plate. The diverse modes of deformation are consistent with the maintenance of critical taper.

Plain Language Summary In tectonically active mountain belts, the crust deforms internally to maintain a characteristic wedge geometry during growth. Such deformation is accommodated by a variety of mechanisms including faulting, folding, and dissolution of rock. New structural and thermochronometric data from the eastern Greater Caucasus of Azerbaijan characterize the influence of mechanical properties of deforming rock on the modes of active deformation. The eastern Greater Caucasus contains two major sedimentary rock packages with distinct lithologic properties that have been deformed via different mechanisms. The orogen interior consists of thin sandstone and shale beds deformed primarily by short-wavelength folding. A package of thick-bedded volcanoclastic sediment known as the Vandam Zone is deformed via slip of coherent thrust sheets. The contrasting modes of deformation that have affected these rock packages confirm the influence of lithologic properties on deformation processes and mountain belt structure. Thermochronometric data record the propagation of deformation into the Vandam Zone strata as well as subsequent deformation and accelerated exhumation within the mountain belt interior. The spatiotemporal distribution of deformation functioned to maintain the tapering wedge geometry of the deforming crust.

1. Introduction

Orogenic wedges are tapered, internally deforming tectonic features that form as a result of convergent tectonic motion and crustal shortening (Dahlstrom, 1969, 1970; DeCelles & Mitra, 1995; Hubbard et al., 2015; G. F. Moore et al., 2009; Singh et al., 2008, 2011). Over time, orogenic wedges grow via propagation of deformation into undeformed crust (e.g., Graveleau et al., 2012; Malavieille, 2010) and are thought to undergo internal deformation to maintain a characteristic shape as they increase in volume (Chapple, 1978; Davis et al., 1983). Growth

Visualization: A. R. Tye, E. Cowgill
Writing – original draft: A. R. Tye
Writing – review & editing: A. R. Tye,
N. A. Niemi, E. Cowgill, F. A. Kadirov,
G. R. Babayev

and deformation of wedges have been described at the whole-orogen scale using both frictional (Dahlen, 1990; Dahlen et al., 1984; Davis et al., 1983) and viscous (e.g., Emerman & Turcotte, 1983) models of deformation.

The mechanisms by which orogenic wedges deform internally to maintain their self-similar geometry are highly varied (Figure 1). For example, shortening in many wedges is accommodated by tectonic transport of regionally coherent thrust sheets that form imbricate fans and duplexes (Figure 1a; Boyer & Elliott, 1982; Butler, 1987; Dahlstrom, 1970; Lavé & Avouac, 2000; McQuarrie, 2004; Mulugeta & Koyi, 1992; Suppe, 1981; Uba et al., 2009). In some other wedges, notably some accretionary prisms above subduction zones, layers are structurally thickened during transportation toward the wedge interior, with only minor fault offset (Figures 1b and 1c; Ghisetti et al., 2016; Singh et al., 2008, 2011). Such thickening likely reflects short-wavelength folding observed in some exhumed accretionary prisms (e.g., Ditullio & Byrne, 1990). Correspondingly, wedges exhibit multiple modes of accretion of new material (e.g., Malavieille, 2010). New material can undergo basal accretion, in which it is underthrust beneath the wedge before being accreted, often leading to the formation of antiformal stacks of thrust sheets and focused thickening in the prism interior (Figure 1a; Lavé & Avouac, 2000; Platt et al., 1985; Sample & Fisher, 1986). Alternatively, new material can undergo frontal accretion, in which it is added to the toe of the wedge after being subjected to minor or no underthrusting (Figures 1b and 1c; Gulick et al., 1998; Singh et al., 2011). Characterizing the controls on these various modes of deformation is key to understanding the evolution of orogens.

Because wedge mechanics are well-described at the whole-orogen scale (e.g., Dahlen, 1990; Davis et al., 1983; Emerman & Turcotte, 1983), differences in internal wedge deformation likely arise from variations in internal properties and/or surface boundary conditions. For instance, surface erosion is thought to control first-order material flow and structural architecture in orogens (Bonnet et al., 2007; Malavieille, 2010; Willett, 1999; Willett & Brandon, 2002), and mechanisms of erosion are dramatically different in subaerial and submarine wedges (Platt, 1986; Willett, 1999; Yamada et al., 2010). Pore-fluid pressure, often elevated in subaqueous orogens due to subduction of fluid-saturated sediment and mineral dewatering (J. C. Moore & Vrolijk, 1992), is thought to play a crucial role in defining orogenic wedge structure (e.g., Westbrook & Smith, 1983). Finally, the mechanical properties of the geologic materials incorporated into the orogenic wedge, such as bedding thickness and strength of potential slip planes, have been demonstrated to influence the structural style and distribution of faults in orogens (Casciello et al., 2009; Fitz-Diaz et al., 2012).

The eastern Greater Caucasus of Azerbaijan, part of the Arabia-Eurasia collision zone (e.g., Philip et al., 1989), presents an opportunity to assess the effect of lithologic properties on modes of deformation within an orogenic wedge. Due to the inheritance of a complex system of relict rift and/or ocean basins (Cowgill et al., 2016; Vincent et al., 2016), the eastern Greater Caucasus is composed of structural packages with markedly different lithologic properties. The interior of the orogen consists of a succession of thin-bedded, marine sandstones and shales that is structurally juxtaposed against an accreted succession of thick-bedded, volcanoclastic sandstones and tuffs known as the Vandam Zone (Alizadeh et al., 2016; Bairamov et al., 2008). Differences in deformation mechanism between these structural packages, which share equivalent tectonic and erosional boundary conditions, are likely due to distinct lithologic properties.

We use new geologic mapping and thermochronometry data to investigate the tectonic evolution of the eastern Greater Caucasus and the influence of lithologic variation on deformation within the wedge. We present new geologic mapping transects that traverse the width of the Greater Caucasus in Azerbaijan (Figure 2) and characterize the gross structural geometry of the orogen. To constrain the evolution of the orogen, the structural data are combined with thermochronometric analyses from across the range, including a novel analysis of post-cooling deformation and its effects on age-elevation trends in thermochronometric transects. We find evidence of first-order lithologic controls on orogen structure and mode of accretion.

2. Geological Background

The WNW-striking Greater Caucasus orogen is located within the Arabia-Eurasia collision zone and accommodates convergence between Eurasia to the north and the Lesser Caucasus continental block to the south (Figure 2a; Adamia et al., 2011; Cowgill et al., 2016; Forte et al., 2022; Mosar et al., 2010, 2022; Philip et al., 1989; Tibaldi et al., 2020; Vincent et al., 2016, 2007; Zonenshain & Pichon, 1986). The Caucasus region has a complex tectonic history, with multiple episodes of subduction, terrane accretion, and rifting during Phanerozoic time (Adamia

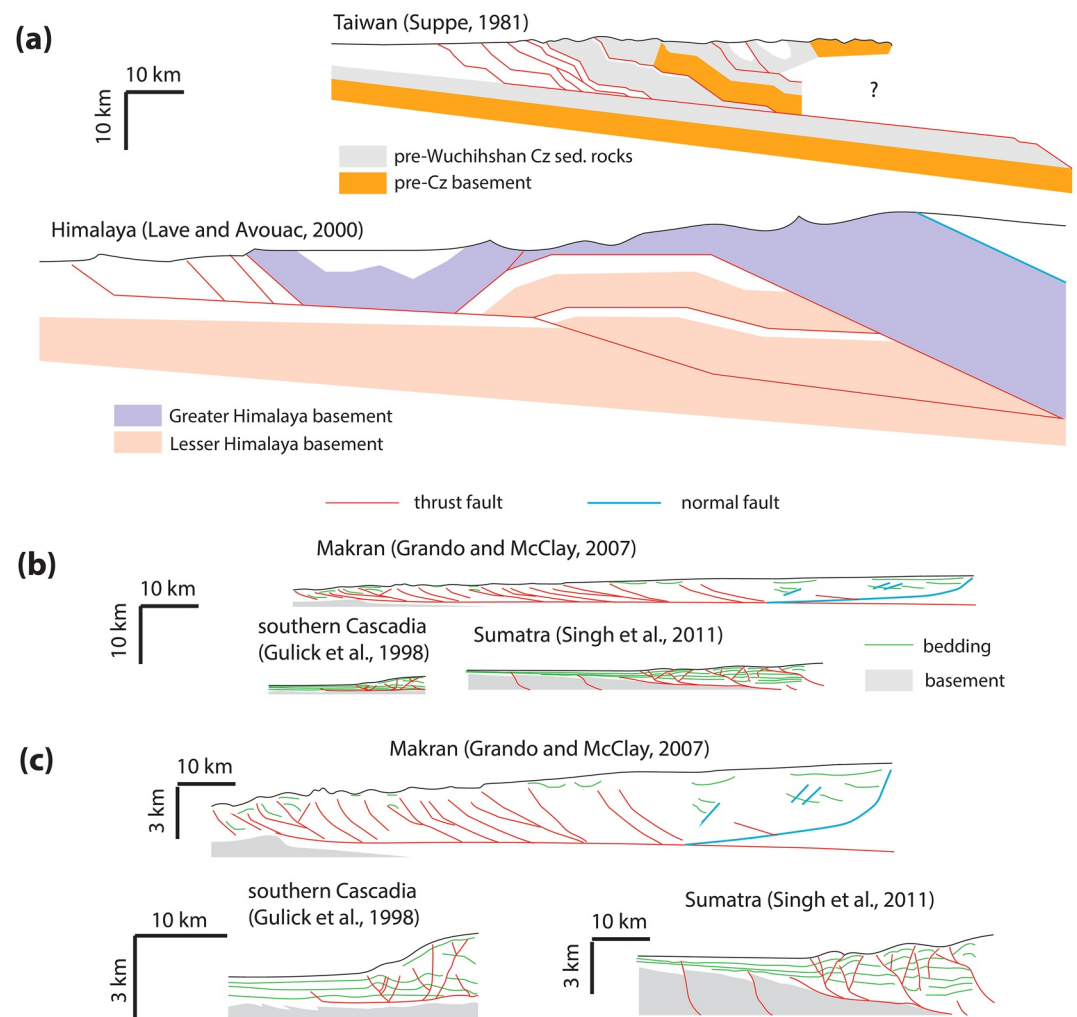


Figure 1. Cross-sections comparing structure of several orogenic wedges, including (a) examples where shortening is accommodated by major thrusts and (b) examples where thrusting accounts for a relatively smaller portion of shortening. (c) Vertically exaggerated cross-sections of the wedges shown in (b).

et al., 2011; Şengör, 1984; Stampfli, 2013; Vasey et al., 2020). The successions of marine sedimentary rocks and volcanoclastic rocks exposed across the majority of the orogen record Jurassic to Eocene deposition in a backarc basin, termed the Greater Caucasus Basin, on the Eurasian margin north of the Jurassic to Eocene Lesser Caucasus magmatic arc (Figure 2; Cowgill et al., 2016; Nalivkin, 1976; Tye et al., 2021; Vasey et al., 2021; Vincent et al., 2016; Zonenshain & Pichon, 1986). The Greater Caucasus Basin was subsequently closed during the Cenozoic Arabia-Eurasia collision (Adamia et al., 2011; Cowgill et al., 2016; Khain, 1975; Vincent et al., 2007).

The tectonic setting of the Greater Caucasus varies along strike (Figure 2a; Forte et al., 2014). The western Greater Caucasus accommodates 4 mm/yr convergence (Reilinger et al., 2006; Sokhadze et al., 2018), is characterized structurally by coherent macro-scale thrust sheets of 2–10 km thickness (Trexler et al., 2022), and has earthquake depths of <20 km (Mumladze et al., 2015). In contrast, the eastern Greater Caucasus is accommodating convergence rates of 10–12 mm/yr (Figure 2a; Kadirov et al., 2012, 2015; Reilinger et al., 2006) and earthquake depths of up to >100 km have been recorded north of the range (Burmin et al., 2019; Gunnels et al., 2021; Mellors et al., 2012; Mumladze et al., 2015). Recent tomographic results indicate that the Kura foreland basin, which is being underthrust beneath the eastern Greater Caucasus, is floored by thin (<20 km thick), mafic crust (Figure 2b; Gunnels et al., 2021). Seismic tomographic imaging and the distribution of deep earthquakes suggest the presence of north-dipping, subducted Kura basement beneath the eastern Greater Caucasus (Figure 2b; Mellors et al., 2012; Mumladze et al., 2015; Skobeltsyn et al., 2014). Relocated earthquakes suggest the existence

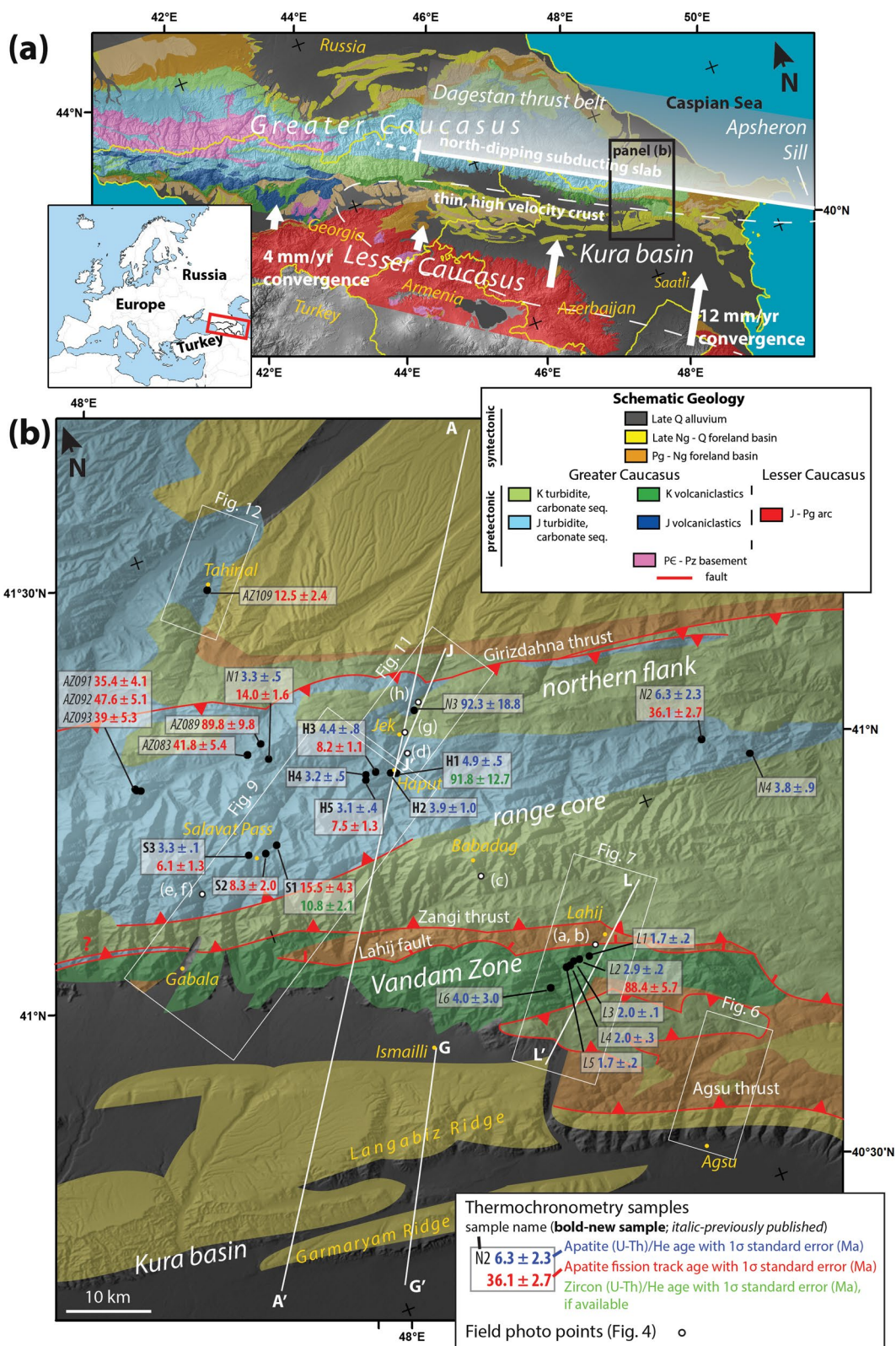


Figure 2.

of two parallel seismogenic layers beneath the eastern Greater Caucasus, one in the upper plate and a second in a subducting lower plate (Gunnels et al., 2021). These data suggest that subduction is active beneath the eastern Greater Caucasus (Figure 2a).

The eastern Greater Caucasus mountains exclusively expose Middle Jurassic and younger sedimentary rocks (Figures 2b and 3; Alizadeh et al., 2016; Azizbekov, 1968; Bairamov et al., 2008; Nalivkin, 1976). Three broad stratigraphic packages crop out across the range: (a) a northern flank succession of thinly bedded sandstone and shale with massive carbonate intervals (Alizadeh et al., 2016; Bairamov et al., 2008; Cumberpatch et al., 2021; Nalivkin, 1976; Figure 3a); (b) a range-core succession of thinly bedded sandstone, shale, and carbonate (Alizadeh et al., 2016; Bairamov et al., 2008; Nalivkin, 1976; Figure 3b); and (c) located at the southern toe of the orogen, the Vandam Zone succession, which comprises volcanoclastic sandstone and conglomerate, volcanic tuff and flows, sandstone, shale, and carbonate (Alizadeh et al., 2016; Bairamov et al., 2008; Kopp, 1985; Nalivkin, 1976; Figure 3c). A buried fourth succession has been revealed by deep drilling in the Kura foreland basin to the south, comprising volcanic, volcanoclastic, siliciclastic, and carbonate strata (Alizadeh et al., 2016; Figure 3d), similar to strata exposed within the Vandam Zone.

The sedimentary facies of the northern flank succession and range-core succession (Figures 3a and 3b) suggest deposition in continental shelf, slope, and deep marine environments (Alizadeh et al., 2016; Cumberpatch et al., 2021; Gavrilov, 2018). Stratigraphic architecture suggests that these strata were deposited offshore of a south-facing continental margin (Cumberpatch et al., 2021; Gavrilov, 2018). Detrital zircon U-Pb age distributions with peaks at ca. 450 Ma and ca. 360 Ma indicate that clastic sands of the northern flank and range-core successions were derived from Scythia, to the north (Allen et al., 2006; Tye et al., 2021), which formed the southern margin of Eurasia at the time of deposition (Saintot, Stephenson, et al., 2006).

The lithologic contrast between the range-core (Figure 3b) and Vandam Zone (Figure 3c) successions suggests different depositional settings for the two packages. The occurrence of Mesozoic igneous rocks in the Vandam Zone (Figure 3c), Kura basin strata (Figure 3d), and the Lesser Caucasus (Figure 2a; Kopp & Shcherba, 1985; Rolland et al., 2011; Sosson et al., 2010) suggests that volcanic and volcanoclastic strata of the Vandam Zone may represent arc-derived sediment. Alternatively, igneous rocks of the Vandam Zone could have been derived from more local, rift-related volcanic sources. Detrital zircon grains from Vandam Zone strata cluster at ca. 104 Ma (Tye et al., 2021), consistent with a different sediment source than the northern flank or range-core packages. In this study, we revisit the structural position of the Vandam Zone and its relationship to the range-core succession using new geologic mapping and thermochronometry.

3. Methods

3.1. Geologic Mapping and Cross-Section Construction

We present 1:50,000-scale geologic mapping along five swath transects that together span the across-strike extent of the eastern Greater Caucasus in Azerbaijan (Figure 2b). This mapping is based mostly on field measurements and observations (e.g., Figure 4), supplemented with freely available satellite imagery in some areas. The full size geologic map and additional structural data are available at <https://doi.org/10.6084/m9.figshare.19469873.v2> (Tye et al., 2022). We defined lithostratigraphic units (Table 1) based on field observations and our units often encompass multiple formations as defined by previous authors (e.g., Bochud, 2011), although many stratigraphic intervals in the region are not named. Previous work establishes the litho-, bio-, and chronostratigraphic framework of the eastern Greater Caucasus (Alizadeh et al., 2016, and references therein), which we rely on in this study. Available geologic maps for the eastern Greater Caucasus are chronostratigraphic (Bairamov et al., 2008; Khain & Shardanov, 1960; Nalivkin, 1976). While mapped ages are broadly consistent between available maps,

Figure 2. (a) Map showing the Greater Caucasus, a WNW-trending mountain belt in western Asia that accommodates NNE-SSW-directed shortening. Schematic geology is shown following the key in (b), based on previous regional mapping (Nalivkin, 1976). White annotation shows geodetic convergence rates (Reilinger et al., 2006), location of a high crustal seismic velocity zone beneath the Kura and South Caspian basins inferred to reflect mafic (possibly oceanic) composition (Gunnels et al., 2021), and the along-strike extent of a subducting slab inferred beneath the range from deep earthquakes (Mumladze et al., 2015). (b) Map showing schematic geology of the eastern Greater Caucasus study area, modified after Bairamov et al. (2008) and Nalivkin (1976), using the same symbology as in (a). White rectangles show extents of structural mapping transects. New and existing (Avdeev, 2011; Bochud, 2011) thermochronometric ages are shown using black circles, with sample mean ages and standard errors displayed in text boxes following the legend shown in the lower righthand corner. Field photo (Figure 4) locations are shown by open, white circles. Lines of cross sections J-J', L-L', and A-A' (this study), as well as G-G' (Forte et al., 2013), are shown in white. Approximate locations of major faults and tectonostratigraphic successions (Figure 3) are labeled.

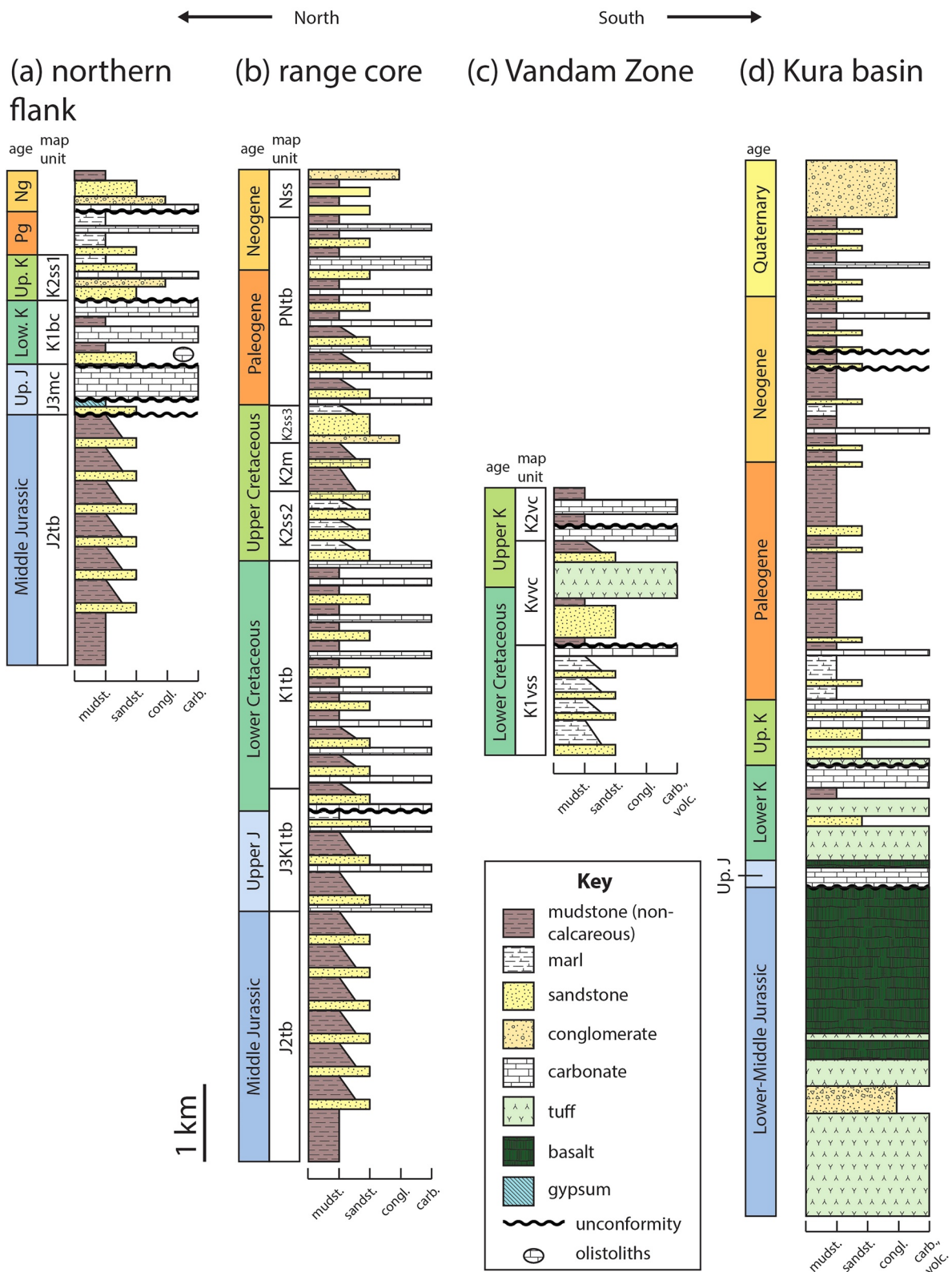


Figure 3. Generalized stratigraphy for (a) the northern flank, (b) range core, (c) Vandam Zone, and (d) Kura basin successions. (a–c) are modified after Bochud (2011) using descriptions from Alizadeh et al. (2016). (d) is based on data from a deep borehole at Saatli (see Figure 2a), modified after Alizadeh et al. (2016, 2000).

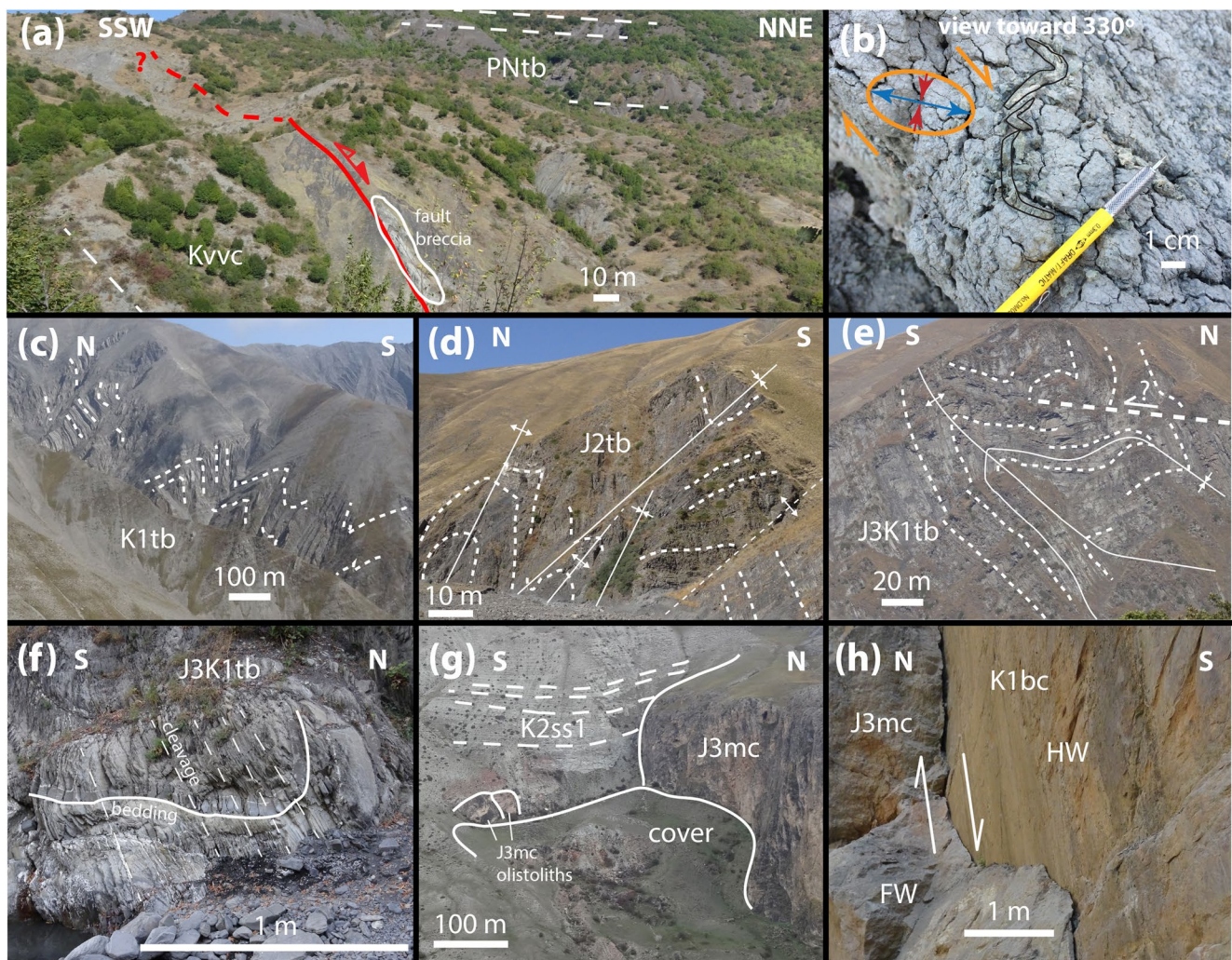


Figure 4. Photographs of important field relations in the eastern Greater Caucasus; see Figure 2 for locations and Table 1 for full unit names and descriptions. In all panels except (f), dashed white lines indicate the trace of sedimentary bedding. (a) North-dipping Lahij fault, which defines the northern margin of the exposed Vandam Zone tectonostratigraphic package (Figure 2b). (b) Folded clast of laminated mudstone within the Lahij fault zone indicating north-side-down, normal-sense slip. At this location, the Lahij fault is a zone of sheared, mud-rich rocks with a block-in-matrix texture that is ~10 m thick. (c) Tight, asymmetric folds deform unit K1tb at Babadag, with wavelengths <1 km. (d) Upright tight to isoclinal folds with wavelengths of order 100 m characteristic of the northern portion of the deformed eastern Greater Caucasus range core. (e) Multiple generations of folding and faulting within unit J3K1tb southwest of Salavat Pass. (f) Axial-plane cleavage in unit J3K1tb. (g) Buttress unconformity in the northern part of the range, where Upper Jurassic massive carbonate (J3mc) is unconformably overlain by Lower to Upper Cretaceous strata (K1bc and K2ss1) containing olistoliths of J3mc. It is possible that the large J3mc outcrop on the right is itself a large olistolith (Cumberpatch et al., 2021). (h) Steeply dipping normal fault in the northern part of the range juxtaposing Upper Jurassic massive carbonate (J3mc) in the footwall (FW) against Lower Cretaceous bedded carbonate (K1bc) in the hanging wall (HW).

minor discrepancies exist, and we generally defer to more recent interpretations of Bairamov et al. (2008). Where available, geochronologic data (Cowgill et al., 2016; Trexler et al., 2022; Tye et al., 2021) are in broad agreement with map age interpretations (Bairamov et al., 2008; Khain & Shardanov, 1960; Nalivkin, 1976). Our mapping effort focuses on characterizing the gross structural architecture of the range.

We constructed geologic cross-sections based on field mapping and structural measurements, with reference to prior studies (Bairamov et al., 2008; Bochud, 2011; Cowgill et al., 2016; Forte et al., 2013; Golubjatnikov & Dubogryzova, 1959; T. Green et al., 2009; Khain & Shardanov, 1960; Nalivkin, 1976; Voronin et al., 1959). Unit thicknesses are derived from our mapping and are consistent with previously reported thicknesses (Bairamov et al., 2008; Bochud, 2011; Golubjatnikov & Dubogryzova, 1959; T. Green et al., 2009; Khain & Shardanov, 1960; Nalivkin, 1976; Voronin et al., 1959). However, subsurface interpretations are inherently uncertain due to the lateral variability in thickness and facies within the sedimentary rocks of the eastern Greater

Table 1
Lithostratigraphic Unit Descriptions

Symbol	Name	Description
All areas		
Qss	Quaternary sandstone	Coarse to fine sandstone, locally conglomeratic, with discontinuous silt to clay horizons, channel forms
Nss	Neogene sandstone	30 cm–2 m thick, coarse to medium, lithic-rich, gray-tan sandstones
PNtb	Paleogene to Neogene sandstones and shales	Dark gray to black shales with sparse, 2–10 cm thick, lithic-rich, coarse to fine sandstone beds, locally turbiditic. Rare intervals are sandstone-rich. Normal grading and flame structures are common in sandstone beds
Vandam Zone		
K2vc	Upper Cretaceous Vandam carbonates	Blue-gray lithic-rich, calcareous, ~10 cm bedded sandstone-shale sequence transitioning upward into blue-gray muddy carbonate
Kvvc	Middle Cretaceous Vandam volcanoclastic succession	10 cm–5 m thick, lithic-rich, volcanoclastic, coarse to medium sandstone beds with thin shale interbeds and some conglomeratic intervals. Normal grading, load casts on some beds. 1–10 m thick intervals of volcanic breccia, flows, tuffs. Carbonate olistoliths to 10 m in size
K1vss	Lower Cretaceous Vandam sandstone	3–10 cm gray-white, calcareous, coarse to fine sandstone with thin (~2 cm) gray shale interbeds, locally with pebble conglomerate with lithic and clay clasts
Range core		
K2ss3	Upper Cretaceous sandstone 3	Blue to white sandstone beds dominantly 3–10 cm thick (rarely 1 m thick) interbedded with 5–10 cm, gray shale to white marl beds. Normal grading, cross beds, and load casts common
K2mfb	Upper Cretaceous brecciated mudstone	Brecciated K2m involved in faulting. Chaotic folding and shearing of clay horizons, fracturing of sandstones
K2m	Upper Cretaceous mudstone	Alternating red and blue mudstone sequence, locally interbedded with blue-gray, medium to fine sand horizons 3–10 cm thick
K2ss2	Upper Cretaceous sandstone 2	Blue-gray sandstone beds, 3–10 cm thick (up to 1 m in rare cases), interbedded with 5–10 cm shale beds in turbidite successions. Normal grading, cross beds, and load casts common
K1tb	Lower Cretaceous sandstones and shales	Locally turbiditic successions of brown, 3–10 cm sandstone beds interbedded with 5–10 cm, light to dark gray shale intervals. Cone-in-cone structures and load casts observed, calcareous cementation
J3K1tb	Upper Jurassic-Lower Cretaceous (?) calcareous sandstones and shales	Locally turbiditic, 2–10 cm, fine to medium, lithic-to quartz-rich sandstone beds interbedded with 5–10 cm mudstone intervals. Normal grading, load casts, and cross beds are common. Lithologically similar to J2tb except carbonate cement is common, fine-grained intervals are often dominantly carbonate mud

Table 1
Continued

Symbol	Name	Description
Northern flank		
K2ss1	Upper Cretaceous sandstone 1	2–10 cm, red to white sandstone beds interbedded with gray shales ~5 cm thick. Basal boulder conglomerate of dominantly carbonate clasts, intervals of cobble to boulder conglomerates
K1bc	Lower Cretaceous bedded carbonate	Bedded oolitic carbonate and gray mudstone. At southern end of exposed area, gray mudstone is dominant, with 10 cm–2 m, oolitic limestone beds at irregular intervals with pervasive ripup clasts. At northern end of exposure area, 1–10 m, oolitic carbonate beds dominant with minor gray to red mudstone. Isolated beds of poorly sorted pebble to boulder conglomerate, clasts include J3mc carbonate, siltstone
K1mo	Lower Cretaceous massive olistolith	km-scale olistolith detached from nearby J3mc
J3mc	Upper Jurassic massive carbonate	Massive carbonates, wackestone to grainstone, grains 1–10 cm, often ambiguous bedding
J2tb	Middle Jurassic organic-rich sandstones and shales	Locally turbiditic medium, quartz-rich, sandstone to black shale. Sandstone intervals dominantly 2–3 cm thick, up to 10 m in a handful of cases. Cross bedding, flame structures, load casts, cone-in-cone structures. Local concretions

Note. Age determinations follow previous mapping and geological descriptions (Alizadeh et al., 2016; Khain & Shardanov, 1960; Nalivkin, 1976), although these lithostratigraphic units may differ from units defined by previous workers. The units are separated based on the portion of the orogen in which they appear. See Figure 6b for unit correlation.

Caucasus, lack of undeformed stratigraphic reference sections, and lack of publicly available subsurface data (Bairamov et al., 2008; Bochud, 2011; Golubjatnikov & Dubogryzova, 1959; T. Green et al., 2009; Khain & Shardanov, 1960; Voronin et al., 1959). For simplicity, pre-Cenozoic unit thicknesses are held constant within our cross sections, except where observations require otherwise. Cross sections were line-balanced graphically using vector graphics software.

3.2. Thermochronometry Data and Interpretation

To investigate exhumation in the eastern Greater Caucasus we report 13 new low-temperature thermochronometric sample cooling ages (Table 2, Tables S1 and S2) and integrate these data with 19 sample cooling ages available in Ph.D. dissertations (Avdeev, 2011; Bochud, 2011; Figure 2). Thermochronometric ages in natural samples are determined by the time-temperature histories of sampled rocks and can thus constrain the history of exhumation in orogens (Reiners & Brandon, 2006). Thermochronometric systems analyzed in this study include (U-Th-Sm)/He in apatite (AHe; closure temperature ~40°C–80°C; e.g., Ehlers & Farley, 2003; Farley, 2002; Flowers et al., 2022) and (U-Th)/He in zircon (ZHe; closure temperature ~160°C–200°C; e.g., Reiners, 2005; Reiners et al., 2004), as well as apatite fission track (AFT; closure temperature ~80°C–120°C; Donelick et al., 2005). Thermochronometric data from new samples include 6 AHe and 2 ZHe sample cooling ages (Table S1) and 5 AFT pooled ages (Table S2). Our new samples were collected in two vertical transects (Figure 2). All samples discussed were collected from Mesozoic sandstones, and sample thermochronometric ages are younger than depositional ages for all samples. The lack of Cenozoic volcanism within the study area (Figure 2b) suggests that burial and exhumation are the drivers of sample temperature variation and thermochronometric ages. Analyses were often limited by sample mineral yield, particularly apatite quality, quantity, and grain-size, such that not all thermochronometric systems were analyzed for each sample. Mineral separations were performed on crushed and pulverized samples using standard magnetic susceptibility and heavy liquid density separation techniques at the University of Michigan. Mineral grains were hand-selected for AHe and ZHe analysis based on size (width \geq 80 μ m), clarity, and morphology. Many analyzed grains were highly abraded and/or broken, which likely reflects the texture of sampled sandstones and perhaps the effects of physical disaggregation. Limited mineral yields led to the selection

of some analyzed grains that contained small inclusions, as noted in Table S1. He measurements for new samples were conducted at the University of Michigan Thermochronology Lab (see Niemi & Clark, 2018, and Supporting Information for detailed analytical procedures). Mineral dissolution as well as U, Th, and Sm measurements were conducted at the University of Arizona Radiogenic Helium Dating Laboratory (Reiners & Nicolescu, 2006). New AFT data were collected at the University of Arizona Fission Track Lab, following the procedure of Thomson et al. (2013; and see Supporting Information). AHe and AFT data of Avdeev (2011) were collected at Caltech and Apatite to Zircon, Inc., respectively, using methods described in detail in Avdeev and Niemi (2011). Reported helium ages were corrected for alpha ejection using equations of Ketcham et al. (2011). Sampling and analysis methods of Bochud (2011) are described therein. Sample preparation and data reduction methods are similar between the available data sets, such that direct comparison of measured ages is possible.

We use multiple methods to make tectonic interpretations based on thermochronometric dates. For samples with paired AHe and AFT ages that were both reset prior to exposure at the surface, we use the age differences and nominal closure temperatures for the two systems (60°C and 110°C, respectively; Reiners & Brandon, 2006) to obtain a first-order estimate of the long-term cooling rate. We convert these long-term cooling rates into apparent exhumation rates using an assumed geothermal gradient of 20–30°C/km, which was inferred for the Cascadia accretionary wedge (Brandon et al., 1998), an accretionary orogen that is underlain by a subducting slab, similar to the eastern Greater Caucasus (Gunnels et al., 2021; Muñladze et al., 2015). These apparent exhumation rates are time-averaged rates that assume simple, monotonic T-t pathways, and such rates are only calculated for samples with young (<10 Ma) AFT and AHe ages, and where available thermal models are consistent with such monotonic histories. Given the ongoing active deformation we demonstrate in the eastern Greater Caucasus, these calculated exhumation rates are probably reasonable approximations despite their caveats and limitations.

We also infer apparent exhumation rates from the slope of elevation versus age for multiple, vertically arrayed samples (e.g., Farley et al., 2001). Making such inference involves caveats related to sample tectonic transport vectors and isotherm geometry (e.g., Huntington et al., 2007; Stuwe et al., 1994). For our vertically arrayed samples, horizontal offsets between samples are mostly parallel to the orogen (Figure 2b), limiting bias associated with orogen-scale isotherm topography (Huntington et al., 2007). Locally differing isotherm depths beneath ridges and valleys may impact our thermochronometric dates (e.g., House et al., 1998; Reiners, 2007). However, published numerical modeling suggests that for the topography of our sample areas (interfluves with ~1 km vertical relief and 5–10 km horizontal width; Figure 2b) and the exhumation rates we infer below ($\lesssim 1$ mm/yr), the effect is probably minimal (perhaps 10%; Stuwe et al., 1994). As shown below, the potential effect of local isotherm variation is dwarfed by exhumation rate uncertainties, which are greater than half an order of magnitude.

3.3. Thermal Modeling

Because the relationship between rock time-temperature histories and resultant thermochronometric ages is complex (Wolf et al., 1998), we use a Bayesian inverse thermal modeling method, implemented in the program “QTQt”, to determine permissible cooling histories consistent with measured thermochronometric ages (Gallagher, 2012). Apatite and zircon He diffusion kinetics were modeled according to the equations of Farley (2000) and Reiners et al. (2004), respectively. Apatite fission track annealing was calculated using the algorithms of Ketcham et al. (2007). Thermal modeling parameters, including permissible ranges of and constraints on time and temperature, were varied based on observed thermochronometric ages, available thermochronometric systems, and time and temperature periods of interest (see Table S3 and Supporting Information for details). Applicable radiation damage models (Flowers et al., 2009; Guenther et al., 2013) were used where justified by positive age-eU trends (e.g., Flowers & Kelley, 2011; Figure S1). We report thermal models for samples where the Bayesian routine converged and models generally fit the data to within uncertainties (Figure S2). AHe ages in some samples are overdispersed compared to the variation that can be accounted for by thermal models (Figure S2), which may be caused by recognized or unrecognized microinclusions, or uncertainties in crystal geometry due to sedimentary abrasion of the sampled grains (Table S1; Flowers et al., 2022).

3.4. Block Rotation Modeling of Thermochronometric Data

The two vertical thermochronometry transects we present show negative correlations between elevation and thermochronometric ages, opposite of the expected correlation for vertical exhumation of a block of crust

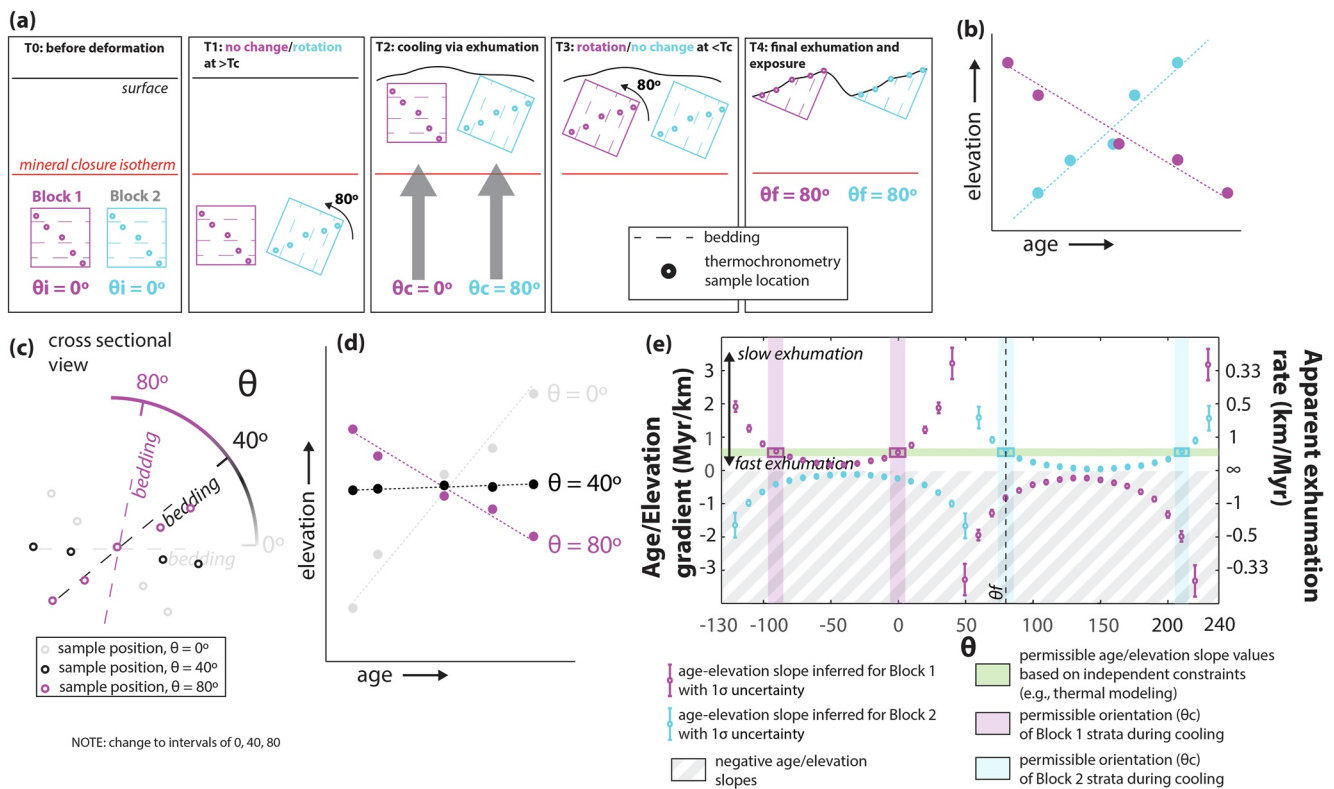


Figure 5. Conceptual model illustrating novel method used to constrain block rotation of rocks sampled for thermochronometry. (a) Cross-sectional diagram of two distinct deformation histories, which involve tilting and exhumation, affecting rock packages Block 1 and Block 2. Block 2 is tilted prior to cooling, whereas Block 1 is tilted following cooling. The orientation of bedding of the tilted blocks is described by the variable θ , which is defined such that $\theta = 0$ corresponds with horizontal, upright bedding and positive θ corresponds with counterclockwise tilt. θ_i is bedding orientation during formation, assumed to be zero throughout the paper; θ_c is bedding orientation during cooling, and θ_f is modern bedding orientation. Whereas θ_i and θ_f can be assumed or measured in the field, θ_c is unknown for natural samples. (b) Observed ages and elevations for samples from Block 1 and Block 2 follow distinct age-elevation relationships, with tilting after cooling (Block 1) resulting in a negative age-elevation slope. (c) Plot that shows in cross section how the locations of samples in Block 1 are affected by various values of θ . (d) Variation in θ affects the elevation-age slope inferred from the Block 1 thermochronometric sampling transect in complex ways. Effects on the elevation-age slope in general are highly dependent on sample locations. Note that changes in the y-intercept of the age-elevation relationship as a result of changing θ are not shown or interpreted. (e) The relationship between age-elevation slope (a proxy for exhumation rate, subject to the caveats described in the Methods section) and tilt magnitude θ can be used together with available independent constraints on exhumation rate (e.g., thermal modeling results or differences between ages of multiple thermochronometers from a single sample) to infer the orientation of the sampled block during cooling, θ_c . The plot shows the slope of the age-elevation relationship and associated apparent exhumation rate (units are arbitrary) calculated as a function of θ for Blocks 1 and 2 (symbols), along with independent constraints on exhumation rate (green bar) and modern orientation θ_f . Values of θ_c , for which the age-elevation slope is consistent with the independent exhumation-rate constraints (green bar), are marked with pink (Block 1) and blue (Block 2) bars. In this example, sampled ages of Block 1 are consistent with cooling while bedding was horizontal ($\theta_c = 0$), and sampled ages of Block 2 are consistent with cooling while bedding was tilted 80° ($\theta_c = 80^\circ$), as shown in (a). The plots show that in some cases, these solutions are not unique and, in natural samples, additional information may be required to justify preference for one solution. In natural samples with unknown deformation histories, this inference method constrains block orientation during cooling, with implications for the magnitude and relative timing of episodes of tilting and cooling. See text for further discussion.

(e.g., Brandon et al., 1998; Farley et al., 2001). Due to pervasive folding in the study area, as demonstrated by observations shown below, we hypothesize that the negative age-elevation correlations may have resulted from fold-related tilting of sampled strata after thermochronometric cooling (Figures 5a and 5b). Existing modeling approaches for vertically arrayed samples do not incorporate changes in relative sample position during or after cooling and therefore are of limited use in interpreting these data. We apply a novel block-rotation modeling method that treats the thermochronometric transect sample locations as fixed relative to one another and examines how rotation of the group of sample locations affects the age-elevation relationship, a proxy for vertical exhumation rate (Figures 5c and 5d). Rotations occur in a cross-sectional reference frame that is perpendicular to dominant measured fold axis orientations at each transect location (Figure 5c), testing the effect of rotating the relative sample positions about the dominant fold axis. Rotations are parameterized by the variable θ , with $\theta = 0$ defined to correspond to horizontal bedding and positive θ corresponding to counterclockwise rotation within the cross-sectional reference frame (Figure 5c). Variation in θ causes variation in the age-elevation relationship of a

set of samples (Figure 5d), such that apparent exhumation rates can be calculated as a function of θ (Figure 5e). θ changes during the deformation history of a sampled block. θ_i , defined as initial θ prior to deformation, is assumed to be zero (Figure 5a). θ_f , the final orientation of the sampled block, is the dominant bedding orientation measured in the sampled field area (Figure 5a). By comparing apparent exhumation rate as a function of θ with independent constraints on exhumation rates from thermal modeling or intra-sample age differences, permissible values of θ during thermochronometric system closure (cooling) can be solved for (Figure 5e). These permissible values of θ during cooling are referred to as θ_c (see further discussion in Appendix A, including of assumptions and limitations). We apply this approach to the two vertical thermochronometric age transects and one horizontal transect reported in this study.

4. Structural and Thermochronometric Results and Interpretation

We collected new structural and thermochronometric data from the eastern Greater Caucasus to constrain the timing and mode(s) of deformation. The data are presented and interpreted in a series of mapped transects from the southern foreland, through the interior, and across the northern flank of the orogen. Where possible, thermochronometric data and thermal models are presented together with structural data (Figure 2). Thermochronometric results from samples within the study area (Figure 2b) but outside of our mapping transects are discussed at the end of the section.

4.1. Agsu Transect

The Agsu transect starts at the southern range boundary of the eastern Greater Caucasus and extends 15 km northeast into the range (Figures 2b and 6). The transect includes folded and faulted Cretaceous to Quaternary strata (Figure 6; Table 1; Khain & Shardanov, 1960; Nalivkin, 1976; Voronin et al., 1959). No thermochronometric analyses were completed for the Agsu transect.

4.1.1. Geological Description

In the southern portion of the transect, Miocene to Pliocene (Nss) and Quaternary (Qss) sandstones are folded into an overturned syncline beneath the south-vergent Agsu thrust (Figure 6; Khain & Shardanov, 1960; Nalivkin, 1976; Voronin et al., 1959). The Agsu thrust places unit PNtb, which encompasses strata of the Koun Suite and Maikop Series of Eocene to Miocene age (Figure 3d; Alizadeh et al., 2016; Khain & Shardanov, 1960; Nalivkin, 1976; Voronin et al., 1959), over unit Nss. The thrust is marked by a zone of chaotically folded and brecciated sandstone and black shale of unit PNtb. The hanging wall of the Agsu thrust is folded into a syncline cored by Qss, which is both folded and overlies PNtb across an angular unconformity (Figure 6). Within this syncline, bedding dip of PNtb is greater than bedding dip of Qss by 31° and 48° on the southern and northern limbs, respectively (Figure 6). Farther north, PNtb is overlain across another angular unconformity by sandstone unit Nss, locally reported as having a latest Miocene biostratigraphic age (Figure 6; Khain & Shardanov, 1960; Nalivkin, 1976; Voronin et al., 1959). At the north end of the Agsu transect, unit PNtb is overthrust by gently north-dipping, Upper Cretaceous marine sandstone (K2ss3; Figure 6; Nalivkin, 1976).

4.1.2. Structural Interpretation

Along the Agsu traverse, deformation commenced prior to latest Miocene time and persisted into Quaternary time, as indicated by the angular unconformity between unit PNtb and units Nss and Qss and the folding of these reportedly latest Miocene (Nss) and Quaternary (Qss) units (Nalivkin, 1976; Voronin et al., 1959). Restoration of bedding in Qss in the hanging wall syncline above the Agsu thrust does not fully restore the fold in the underlying unit (PNtb), indicating folding began prior to and continued after Qss deposition. This latest Miocene to Quaternary folding was likely accommodated by coeval slip on the underlying Agsu thrust. The Cretaceous strata at the northern end of the transect are part of a structural klippe known as the Basgal nappe (Figure 2b; Alizadeh et al., 2016; Bochud, 2011; Khain, 2007).

4.2. Lahij Transect

The Lahij transect lies ~25 km to the NW of the Agsu transect and contains rocks that structurally overlie those exposed on the Agsu transect (Figures 2b and 7a). Folded and faulted Cretaceous and Cenozoic rocks are exposed

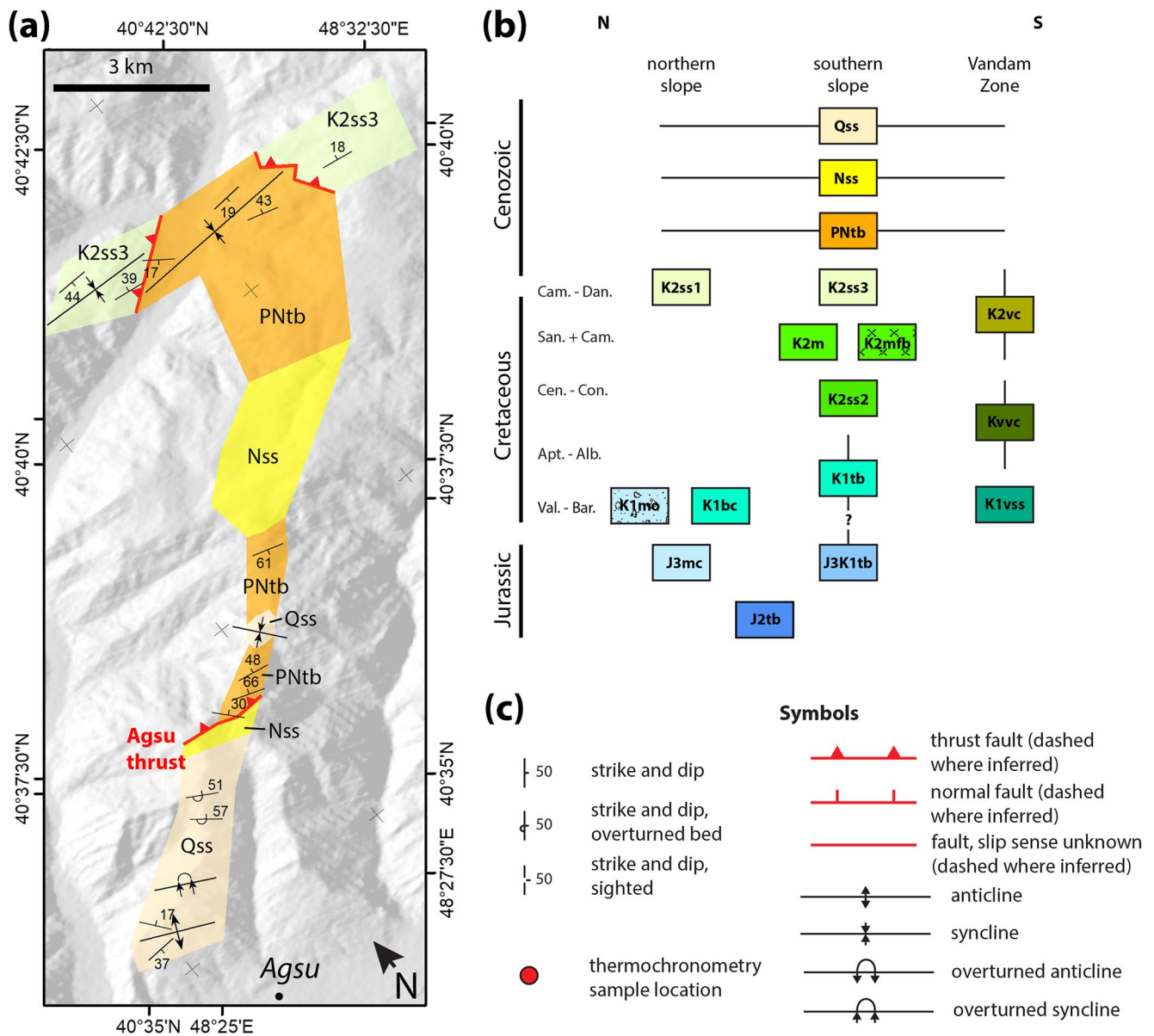


Figure 6. (a) Simplified geologic map of the Agsu transect. See Figure 2b for location. The full size map, with additional structural data, can be found at <https://doi.org/10.6084/m9.figshare.19469873.v2>. (b) Correlation of lithostratigraphic units mapped and described in the text. See Figure 3 for simplified lithology. Complete lithological descriptions can be found in Table 1. (c) Map symbols for geologic maps shown in this and subsequent figures.

along the Lahij transect (Figure 7a). Our structural interpretation is informed by prior work on the fold-thrust belt in the area of the Langabiz and Garmaryam ridges (Forte et al., 2013), which is laterally equivalent to the deformation system in the Agsu transect, but which is located SW of the Lahij transect (Figure 2b). Forte et al. (2013) concluded that folding and thrusting of Neogene to Quaternary strata exposed in the Langabiz and Garmaryam ridges accounted for 18 km of horizontal shortening and was controlled by a north-dipping detachment. This interpretation informs our structural model of the Lahij transect (Figure 7b). Six samples yielded thermochronometric ages along the Lahij transect (Figures 2b and 7a).

4.2.1. Geological Description

The Lahij transect comprises four fault-bounded and lithologically distinct structural panels. From south to north these are the Basgal Nappe (and structurally underlying rock of unit PNtb), Cretaceous carbonate and volcaniclastic strata of the Vandam Zone, a panel of PNtb bounded to the south by the Lahij fault and to the north by the

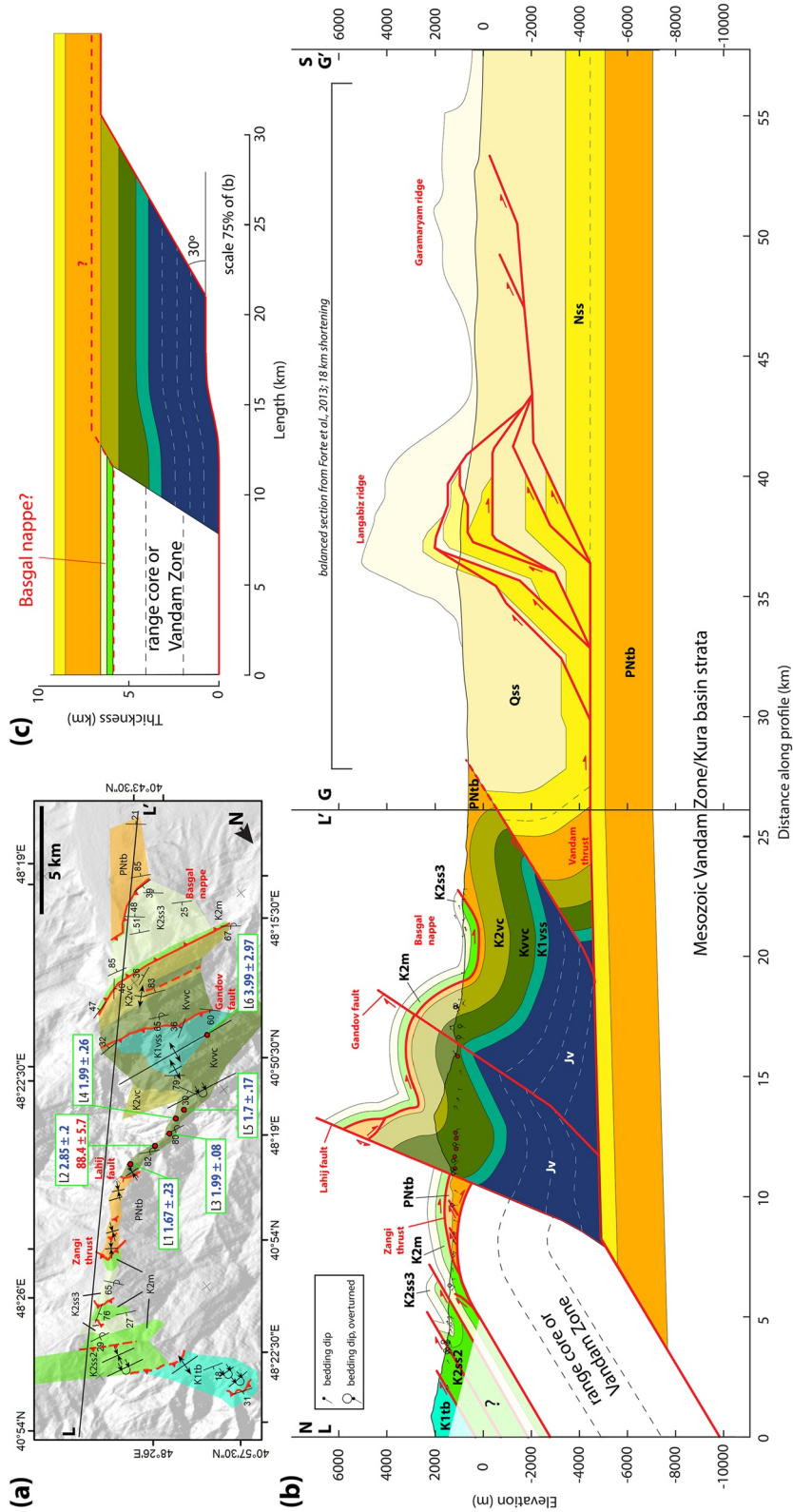


Figure 7. (a) Simplified geologic map and thermochronometric ages of the Lahij transect. See Figure 2b for location and <https://doi.org/10.6084/m9.figshare.19469873.v2> for the full size map with additional data. Thermochronometric samples are shown in red circles with labels formatted as in Figure 2b. (b) Composite cross-section of the Lahij transect along lines L-L' and G-G' (Figure 2b). Geologic units are as depicted in (a), with the addition of Jv, the Jurassic succession of the Vandam Zone. Although we did not encounter unit Jv at the surface, it is reported to crop out west of the study area (Khain & Shardanov, 1960; Nalivkin, 1976). Thickness variations in Jv are attributed to trishear deformation, as illustrated by dashed white form lines. Section G-G' is modified after Forte et al. (2013) and was balanced and restored therein. Approximate locations of thermochronometric samples are shown by red circles projected onto the section. (c) Schematic depiction of accreted strata of the Vandam Zone prior to deformation, shown at 75% scale of (b).

Table 2
Thermochronometry Sample Locations and Mean Sample Age Data

Collection name	Publication name	Longitude (E)	Latitude (N)	Elevation (m)	AHe mean age (Ma)	AHe age standard error (Ma)	ZHe mean age (Ma)	ZHe age standard error (Ma)	AFT pooled age (Ma)	AFT pooled age error (Ma)	AFT ages passed chi-square test	Source
17HAP02	H5	48.1777593679405	41.1447223040639	2,806	3.1	0.4	-	-	7.5	1.3	Yes	This study
17HAP03	H4	48.1802618686079	41.1510243641968	2,539	3.2	0.5	-	-	-	-	-	This study
17HAP04	H3	48.1932958960693	41.1505345674961	2,284	4.4	0.8	-	-	8.2	1.1	Yes	This study
17HAP05	H2	48.2101617098332	41.1428264854645	1,964	3.9	1	-	-	-	-	-	This study
17HAP06	H1	48.2169089747968	41.1397564040707	1,796	4.9	0.5	91.8	12.7	-	-	-	This study
16XIN04	S1	48.0443142731584	41.1064153726049	2,556	-	-	10.8	2.1	15.5	4.3	Yes	This study
16XIN07	S3	48.0068288088407	41.1064256820322	3,251	3.3	0.1	-	-	6.1	1.3	Yes	This study
16XIN08	S2	48.0279032611516	41.1010000340523	3,017	-	-	-	-	8.3	2	Yes	This study
AB0867	L1	48.366586	40.84032	1,173	1.7	0.2	-	-	-	-	-	Avdeev (2011)
AZ0605	L2	48.353808	40.841153	1,188	2.9	0.2	-	-	88.4	5.7	Yes	Avdeev (2011)
AB0866	L3	48.345823	40.841128	1,098	2	0.1	-	-	-	-	-	Avdeev (2011)
AB0855	L4	48.339746	40.838003	1,101	2	0.3	-	-	-	-	-	Avdeev (2011)
AB0862	L5	48.334866	40.837371	1,138	1.7	0.5	-	-	-	-	-	Avdeev (2011)
AB0856	L6	48.307258	40.819571	1,082	4	3	-	-	-	-	-	Avdeev (2011)
AB0890	N1	48.071838	41.21152	2,558	3.3	0.5	-	-	14	1.6	No	Avdeev (2011)
AZ0619	N2	48.592548	41.048605	1,176	6.3	2.3	-	-	36.1	2.7	No	Avdeev (2011)
AZ0620	N3	48.265042	41.206848	1,622	92.3	18.8	-	-	-	-	-	Avdeev (2011)
AB0888	N4	48.643753	41.011043	1,259	3.8	0.9	-	-	-	-	-	Avdeev (2011)
AZ083	AZ083	48.04839	41.2257	2,745	-	-	-	-	41.8	5.4	No	Bochud (2011)
AZ089	AZ089	48.06897	41.23285	3,080	-	-	-	-	89.8	9.8	No	Bochud (2011)
AZ091	AZ091	47.90098	41.23344	3,947	-	-	-	-	35.4	4.1	No	Bochud (2011)
AZ092	AZ092	47.90223	41.23085	3,805	-	-	-	-	47.6	5.1	No	Bochud (2011)
AZ093	AZ093	47.90676	41.22879	3,629	-	-	-	-	39	5.3	No	Bochud (2011)
AZ109	AZ109	48.07161	41.43801	954	-	-	-	-	12.5	2.4	Yes	Bochud (2011)

Note. See Supporting Information (Tables S1 and S2) for complete thermochronometry data.

Zangi thrust, and Lower to Upper Cretaceous strata in the hanging wall of the Zangi thrust (Figures 2b and 7a; Khain & Shardanov, 1960; Nalivkin, 1976).

In the southern part of the transect, Cenozoic strata (PNtb; locally reported to be Late Miocene in age; Khain & Shardanov, 1960) in the hanging wall of the Agsu thrust are structurally overlain by a thrust sheet of Upper Cretaceous strata known as the Basgal nappe (Figures 2b and 7; Alizadeh et al., 2016; Bochud, 2011; Khain, 2007; Khain & Shardanov, 1960; Nalivkin, 1976). In the study area, rocks at the base of the Basgal Nappe comprise >10 m of chaotically folded and brecciated red and blue shales and sandstones (K2mfb), which are overlain by thin- to medium-bedded mudstone and white sandstone (K2ss3; Figures 3b and 7; Khain & Shardanov, 1960; Nalivkin, 1976). The Basgal Nappe is folded into a syncline, with K2mfb outcropping on both the northern and southern limbs. Unit PNtb outcrops in a small area that is structurally beneath the northeastern edge of the mapped portion of the Basgal Nappe (Figure 7a).

North of and structurally beneath the Basgal Nappe and deformed PNtb strata, Lower to Upper Cretaceous volcanoclastic and carbonate strata of the Vandam Zone are folded and faulted (Figures 3c and 7; Khain, 2007; Khain & Shardanov, 1960; Kopp, 1985; Nalivkin, 1976). The Vandam Zone is composed of Lower Cretaceous calcareous, gray, thin-bedded sandstone and mudstone (K1vss), mid-Cretaceous thick-bedded volcanoclastic sandstone, tuff, and mudstone (Kvvc), and Upper Cretaceous blue calcareous sandstone to muddy carbonate (K2vc; Figures 3c and 7; Khain & Shardanov, 1960; Kopp, 1985; Nalivkin, 1976). The Vandam Zone strata generally deform coherently into south-vergent folds with 5–10 km wavelengths (Figure 7). A north-dipping fault that locally juxtaposes K1vss in its hanging wall against Kvvc in its footwall, indicating reverse slip, is referred to here as the Gandov fault (Figure 7). The location of the Gandov fault within the core of an overturned, south-vergent anticline is consistent with a propagating thrust breaching a fault-propagation fold (Figure 7).

The northern margin of the Vandam Zone is defined by a north-dipping zone of breccia herein named the Lahij fault that juxtaposes the limb of an overturned syncline of Vandam Zone strata in the footwall against tightly folded shale and sandstone of unit PNtb in the hanging wall (Figures 4a, 4b, and 7; Bairamov et al., 2008; Bochud, 2011; Khain & Shardanov, 1960; Nalivkin, 1976). The stratigraphic age juxtaposition across the fault, along with the geometry of a folded clay clast in the fault zone (Figure 4b), suggests normal-sense slip (Figure 7). In the hanging wall of the Lahij fault, fold limbs of PNtb strata are steeply to moderately dipping with fold axes dominantly trending WNW (Figure 7a).

Folded PNtb strata are truncated to the north by the north-dipping Zangi thrust, which carries Lower to Upper Cretaceous strata in the hanging wall (Figures 3b and 7; Khain, 2007; Khain & Shardanov, 1960; Nalivkin, 1976). The Zangi thrust is marked by a >500 m thick package of chaotically folded red and blue mudstone with brecciated sandstone interlayers (K2mfb; Figure 7; Khain, 2007; Khain & Shardanov, 1960; Nalivkin, 1976). Overlying units include Lower Cretaceous black shale and thin-bedded, turbiditic sandstone (K1tb), mid-Cretaceous, thin-bedded, blue sandstone and shale (K2ss2), Upper Cretaceous red and blue shale (K2m), and Upper Cretaceous, thin-bedded, blue-gray sandstone and shale (K2ss2; Figures 3b and 7; Khain & Shardanov, 1960; Nalivkin, 1976). These units are deformed by a series of south-vergent, overturned folds with wavelengths of 100 m to 1 km that are locally cut by north-dipping thrusts (Figure 7).

4.2.2. Structural Interpretation

The structure of the Lahij traverse is most simply interpreted as a thin-skinned fold-thrust belt (Figure 7). Based on the subsurface structure we interpret for the Lahij transect and balanced cross sections of the Langabiz-Garmaryam thrust system to the south (Forte et al., 2013), we infer that the fault system of the Lahij transect is kinematically linked via a basal detachment to the Langabiz-Garmaryam system (Figure 7). At the north end of the traverse, the Zangi thrust defines a key transition in structural style, from imbrication of coherent thrust sheets to the south to pervasive, internal folding, as well as thrusting, to the north. The following sections discuss key aspects of the structure shown in our cross-section of the Lahij transect (Figure 7).

4.2.2.1. Relationship Between the Vandam Zone and Strata North of the Zangi Thrust

As noted above, rock types contrast significantly between the Vandam Zone and equivalently aged strata north of the Zangi thrust, which are part of the range-core succession (Figure 3). The volcanoclastic and carbonate strata of the Vandam Zone show closer affinity to the Kura basin succession (Figure 3d) than to the range-core succession north of the Zangi thrust (Agabekov & Moshashvili, 1978; Alizadeh et al., 2016, 2000). This lithologic contrast

suggests the possibility of significant horizontal displacement on the Zangi thrust and/or the Lahij fault. Alternatively, a significant paleogeographic boundary, such as an ancient basin margin (e.g., Mosar et al., 2022), could be associated with either fault.

4.2.2.2. *Affinity of the Basgal Nappe and Emplacement Timing*

Late Cretaceous strata north of the Zangi thrust are lithologically similar to equivalently aged strata of the Basgal nappe (K2mfb, K2ss3; Figures 3 and 7a; Alizadeh et al., 2016). Lithologic correlation of the Basgal nappe with the Zangi thrust hanging wall implies southward emplacement of the nappe over the Vandam Zone package along the Zangi thrust (Figure 7; Bochud, 2011; Khain, 2007). The Basgal nappe was emplaced <12.7 Ma because strata immediately to the north of and structurally beneath the thrust sheet (PNtb) have reported biostratigraphic ages as young as Sarmatian (a Late Miocene regional stage of age 12.7–8.3 Ma; Gradstein et al., 2012; Khain & Shardanov, 1960).

4.2.2.3. *Subsurface Structure of the Lahij Transect*

Based on the surface geology along the Lahij transect (Figure 7a) and the structure of the foreland basin fold-thrust belt to the SW (Forte et al., 2013), we follow Forte et al. (2013) in interpreting major structures along the Lahij transect as rooting into a north-dipping basal detachment beneath the Greater Caucasus (Figure 7b). Balanced cross sections of the foreland fold-thrust belt indicate ~18 km of south-directed thrusting on a 4–5 km deep detachment (Figure 7b; Forte et al., 2013). We name this detachment the Vandam thrust and infer that this fault connects laterally with the Agsu thrust to the east (Figure 2b). The 18 km shortening inferred in Neogene and Quaternary foreland basin strata (Forte et al., 2013) requires that the Vandam Zone structural package has been thrust southwards along the Vandam thrust by at least this amount (Figure 7b). The hanging-wall ramp that truncates the Mesozoic Vandam Zone strata exposed along the Lahij transect is presumably located north of an antiformal stack at Langabiz ridge (Figure 7b) because this structure only exposes Neogene(?) to Quaternary strata and is interpreted to expose the deepest strata above the Vandam thrust at its location (Figure 7b; Forte et al., 2013). To minimize shortening and maintain thickness of units Nss and Qss, we position this hanging-wall ramp beneath the Basgal nappe (Figure 7b). We infer that the equivalent footwall ramp is located at least 18 km to the north, based on shortening in the foreland fold thrust belt (Forte et al., 2013), as depicted in Figure 7.

The thickness and composition of the Vandam Zone thrust sheet is constrained by the ages of strata exposed and their structural relief relative to undeformed strata in the footwall (Figure 7b). The presence of deformed Jurassic rock in the Vandam Zone thrust sheet (“Jv” in Figure 7b) can plausibly explain the elevation of the Cretaceous strata observed in the Vandam Zone, and is consistent with Jurassic exposures mapped within the Vandam Zone by some authors (Khain & Shardanov, 1960; Nalivkin, 1976), but other permissible models may exist.

The structure of the Zangi thrust hanging wall is constrained by observations from north of the Zangi thrust and within the Basgal nappe. A minimum offset on the Zangi thrust is constrained by the strike-perpendicular distance between the northernmost exposure of the Zangi thrust and the southernmost exposure of the Basgal nappe, ~16 km. Lithostratigraphic correlation of the Basgal nappe with the Zangi thrust hanging wall suggests that this portion of the fault is a hanging-wall flat (Figure 7b). The equivalent footwall flat must be underthrust at least 16 km north of the exposed Zangi thrust. The lithostratigraphy of rock beneath the footwall flat is not directly constrained, and could, in principle, have an affinity to either the range-core succession or the Vandam Zone succession, so this region is not assigned lithostratigraphic units when depicted in the subsurface (Figure 7b).

The slip sense and tectonic significance of the Lahij fault is somewhat enigmatic. The juxtaposition of Cenozoic strata (PNtb) in the hanging wall against Cretaceous Vandam Zone rocks in the footwall implies either normal faulting or out-of-sequence thrusting (Figures 4a, 4b, and 7; e.g., Morley, 1988). Extensional kinematic indicators reported for subsidiary faults cutting Vandam Zone strata (Bochud, 2011) and a deformed clay clast in the Lahij fault zone suggesting normal slip (Figure 4b) lead us to favor the normal faulting explanation (Figure 7b). A maximum age for faulting comes from a detrital zircon U-Pb maximum depositional age of ca. 32 Ma for hanging wall PNtb strata (Tye et al., 2021). Despite such evidence for normal-sense slip on the Lahij fault, the presence of an overturned, south-vergent, syncline-anticline pair in the footwall (Figure 7b) is suggestive of thrust propagation associated with the fault (e.g., Erslev, 1991; Suppe & Medwedeff, 1990). We, therefore, hypothesize that the Lahij fault likely formed as a propagating fault breaching a south-vergent anticline, similar to the Gandov fault, and subsequently underwent normal-sense reactivation. Syn-convergent extension is relatively common in orogenic belts, such as the Makran accretionary prism (Grando & McClay, 2007; Hosseini-Barzi &

Talbot, 2003), Himalaya (Lavé & Avouac, 2000; Figure 1a), and Taiwan (Malavieille et al., 2021), and is explored further in the Discussion.

4.2.2.4. Minimum Shortening Estimate

Summing estimated slip along the Vandam thrust, internal shortening of the Vandam Zone, and slip on the Zangi thrust yields a minimum shortening estimate for the Lahij transect of >34 km (Figure 7b). As noted above, we infer at least 18 km of slip on the Vandam thrust, based on shortening documented within the foreland basin fold-thrust belt to the south (Forte et al., 2013). Comparing the deformed to undeformed length of Vandam Zone strata indicates relatively minor (<5 km) shortening accommodated by folding and fault offset within the Vandam Zone (Figures 7b and 7c). Offset of the Basgal nappe from the Zangi thrust indicates at least 16 km of slip on the Zangi thrust (Figure 7), although total slip could be considerably higher. Shortening accommodated by complex internal deformation of the Zangi thrust hanging wall is estimated below.

4.2.3. Thermochronometric Results and Interpretation

Six samples from the Lahij transect, all from the mid-Cretaceous volcanoclastic succession (Kvvc) of the Vandam Zone, yielded thermochronometric ages (Avdeev, 2011; Table 2, Tables S1 and S2; Figure 2b). The analyzed apatite grains had euhedral shapes and were likely contributed to the Vandam Zone succession from volcanic sources (Avdeev, 2011). Mean AHe sample ages range between 1.6 and 4.0 Ma (Table 2, Table S1; Figures 2 and 7a). In addition, sample L2 yielded an AFT sample age of 88.4 ± 5.7 Ma (Table 2; Figures 2 and 7a), which is only slightly younger than either the mapped, biostratigraphic Cenomanian age of the rock (Khain & Shardanov, 1960) or the U-Pb age of detrital zircons derived from the volcanoclastic portions of the Vandam Zone (ca. 104 Ma; Tye et al., 2021). Mean fission track lengths are 12.21 ± 0.21 μm , shorter than lengths of ≥ 15 expected for unannealed samples (e.g., P. F. Green et al., 1986). We interpret the AFT age as recording apatite crystallization or volcanic cooling during Cretaceous deposition of volcanoclastic unit Kvvc. Based on the shortened track lengths and younger sample AHe age (2.9 ± 0.2 Ma), we infer that Cretaceous deposition was followed by heating to temperatures sufficient to reset the AHe age, but insufficient to reset the AFT age, prior to exhumation.

Because both AHe and AFT thermochronometers were analyzed for sample L2, we use inverse thermal modeling (Gallagher, 2012; parameter values in Table S3) to infer a set of time-temperature histories that are likely to have produced the Cretaceous AFT and Pliocene to Quaternary AHe ages observed in the sample (Table 2; Figure 8a). These histories are characterized by post-depositional heating to peak temperatures of 75°C–95°C from mid-Cretaceous time until between ca. 8 and 3 Ma (Figure 8a). Accepted thermal models show that the rate of heating was never greater than 10°C/Myr and averaged <1°C/Myr from ca. 95 Ma until <10 Ma (Figure 8a). The inflection point between heating and cooling occurs between ca. 8 and 3 Ma (Figure 8a). Beginning at this inflection point, modeled histories indicate cooling to surface temperatures at rates of 12–25°C/Myr (Figure 8a). For geothermal gradients of 20°C–30°C, total cooling of 75°C–95°C equates to 2.5–4.75 km exhumation at an average rate of 0.4–1.25 mm/yr.

4.2.3.1. Timing and Effects of Vandam Zone Accretion

We attribute Vandam Zone cooling between ca. 8 and 3 Ma (Figure 8a) to exhumation within the eastern Greater Caucasus orogen, requiring earlier breaking of the Vandam thrust (Figure 7b). Cooling of the Vandam Zone strata was probably driven by either erosional exhumation during and following fault-propagation folding, translation up the Vandam thrust footwall ramp, and/or by tectonic exhumation during normal-sense reactivation of the Lahij fault as described above. In any case, 3 Ma is a minimum age for incorporation of the Vandam Zone package into the orogenic wedge. Deformation of the Vandam Zone package folded the overlying Basgal Nappe thrust into a configuration unlikely to accommodate additional fault slip (Figure 7b). Thus, Vandam Zone accretion and deformation likely coincided with the end of slip on the Basgal Nappe thrust, which underlying strata indicate was emplaced <12.7 Ma (Khain & Shardanov, 1960). The thermochronometric results, combined with the constraints on Basgal Nappe thrust emplacement, thus bracket accretion of the Vandam Zone package to between ca. 12.7 and 3 Ma.

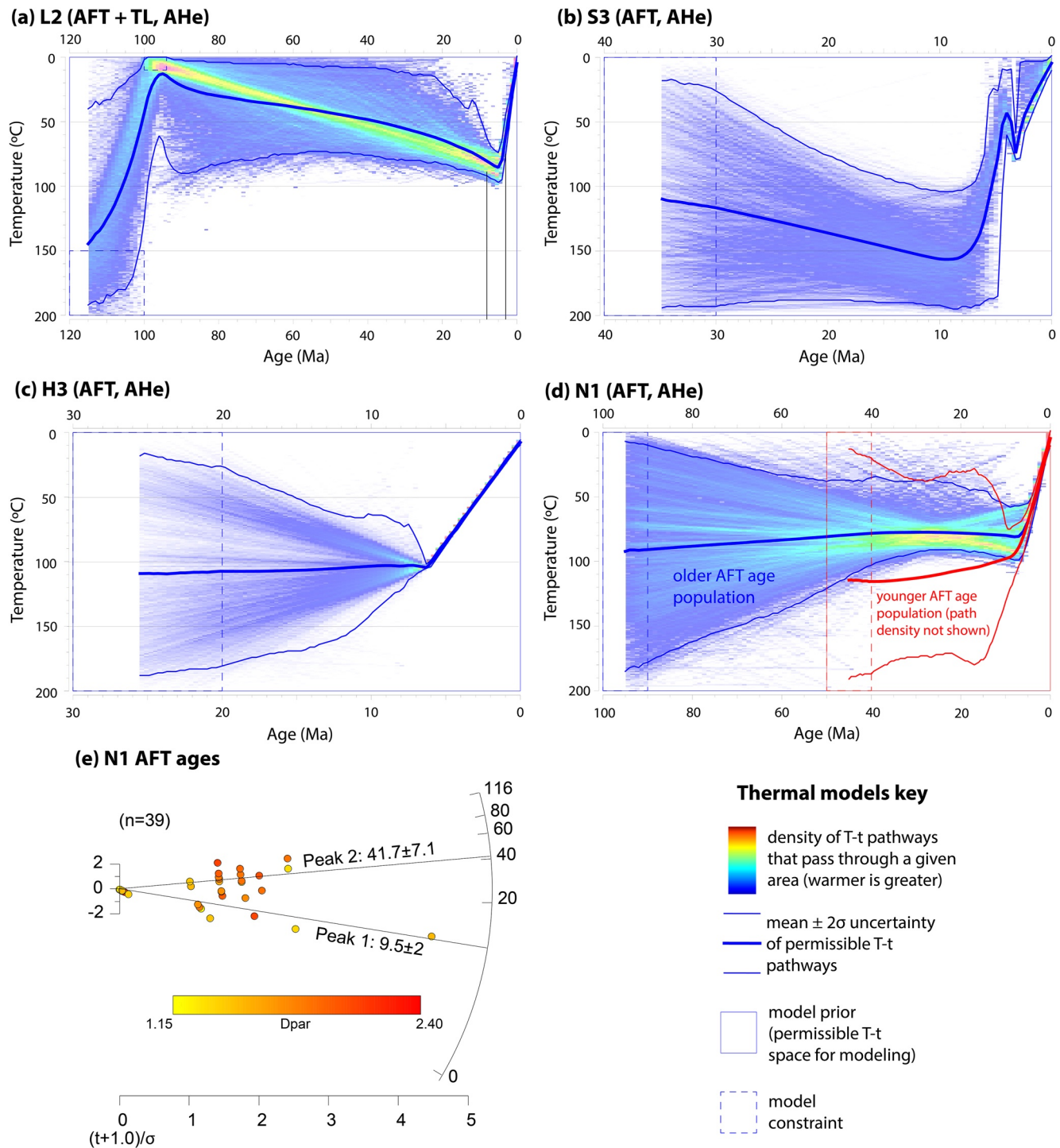


Figure 8. Permissible temperature-time (T-t) histories for selected thermochronometric samples, including L2 (Avdeev, 2011; a), S3 (b), H3 (c), and N1 (Avdeev, 2011; d). Radial plot of AFT age data for sample N1 is also shown (e), constructed using software RadialPlotter (Vermeesch, 2009). T-t histories were inferred using the Bayesian inverse thermal modeling software QTQt (Gallagher, 2012). For sample L2 (a), constraint boxes (dashed lines) are used to represent the likely crystallization ages of analyzed apatite grains and rock depositional age, which are comparable to measured AFT ages (a; Table 2). For other samples, constraints are used to ensure a sufficient model duration (b–d). AFT ages of sample N1 fail the chi-square test for population homogeneity (Table 2) and appear to define a bimodal distribution where age is poorly correlated with composition (e). Therefore, two separate data sets were used for thermal models of N1, one that included the AHe ages and young AFT ages (shown in red in d), and another that included the AHe ages and old AFT ages (shown in blue in d). The young and old AFT age populations both pass the chi-square test and yield similar results for the timing and rate of final sample cooling (d). See Supporting Information for additional discussion of thermal modeling procedure.

4.3. Range-Crest Transect

The range-crest transect is located about 40 km northwest along strike from the Lahij transect and extends from exposures of the Cretaceous Vandam Zone package in the south, across Jurassic siliciclastic strata exposed in the core of the eastern Greater Caucasus, to Jurassic and Cretaceous carbonate strata exposed on the northern flank of the orogen (Figures 2, 3, and 9a; Bairamov et al., 2008; Nalivkin, 1976). We report results for southern, central, and northern segments of the transect, which differ broadly from one another in terms of ages of exposed strata and structural style.

4.3.1. Southern Segment of the Range-Crest Transect

The southern segment of the range-crest transect extends from near Gabala in the south to ~1 km south of Salavat Pass in the north and crosses exposures of Upper Jurassic to Cretaceous strata (Figure 9; Nalivkin, 1976). Although samples were collected along this segment, no apatite or zircon grains of sufficient size and quality for thermochronometry were recovered.

4.3.1.1. Geological Description

The southernmost observed exposures are Lower Cretaceous calcareous sandstone (K1vss) and mid-Cretaceous volcanoclastic sandstone (Kvvc) of the Vandam Zone (Figure 9a; Nalivkin, 1976) deformed into asymmetric, south-vergent overturned folds with 5–10 km wavelengths. The structural style of the Vandam Zone package in the range-crest transect is similar to that observed in the Lahij transect (Figure 7b; Nalivkin, 1976).

Exposures to the north of the Vandam Zone include Lower Cretaceous, thin-bedded sandstone and shale of unit K1tb (Figure 9a; Bairamov et al., 2008; Nalivkin, 1976) that correlate with the northern portion of the Lahij transect above the Zangi thrust (Figures 7a and 9a). The contact between the Vandam Zone (units K1vss and Kvvc) and unit K1tb is not well-exposed in the range-crest transect. Observations permit a similar structural geometry as that observed along strike in the Lahij transect, characterized by a south-vergent fault-propagation fold cut by a normal fault (Figure 7b). To the north of unit K1tb is a succession of Upper Jurassic to Cretaceous(?) calcareous, thin-bedded, fine sandstones and shale with carbonate mudstone interlayers (J3K1tb; Figure 9a; Nalivkin, 1976).

Field observations and bedding measurements from the thin-bedded strata of K1tb and J3K1tb reveal intense deformation (Figures 4c, 4e, 4f, and 9c). Intra-formational, nearly isoclinal folds are overturned toward the south (Figures 4c, 4e, and 9c). These folds generally have wavelengths of 0.5–1 km (Figures 4c and 4e), an order of magnitude less than folds observed in the Vandam Zone strata. Axial-planar cleavage is well-developed throughout these units (Figure 4f). Because of the intense deformation and stratigraphic homogeneity of units K1tb and J3K1tb, constraints on the subsurface geometry from surface exposures are poor, and cross sections were not constructed for the southern segment of the range-crest transect.

4.3.2. Central Segment of the Range-Crest Transect

The central segment of the range-crest transect extends from ~1 km south of Salavat Pass to north of the town of Xinaliq on the northern flank of the eastern Greater Caucasus and crosses exposures of Jurassic strata (Figures 2 and 9a; Nalivkin, 1976). This segment contains two vertical thermochronometric transects.

4.3.2.1. Geological Description and Structural Interpretation

The central segment consists almost entirely of Middle Jurassic, organic-rich, thin-bedded sandstones and shales (J2tb; Nalivkin, 1976), which are pervasively deformed into asymmetric to symmetric, moderate to isoclinal folds ($\lambda = 0.5$ –1 km) and offset by thrusts (Figures 4d and 9b). Sandstone beds are typically thin (<10 cm), with several ~5 m thick beds that do not appear to be laterally continuous enough to be effective marker beds. One particularly large wavelength fold (~10 km) that we traced between the villages of Xinaliq and Jek in the northern part of the transect (Figure 9a) is cored by a >5 m thick sandstone bed. The apparent correlation of fold wavelength with bed thickness suggests that these folds formed by buckling (Butler et al., 2019; Espina et al., 1996), not solely as a result of fault propagation.

At the northern end of the central segment, the Middle Jurassic, organic-rich sandstone-shale succession (J2tb) is in contact with an Upper Jurassic, massive wackestone to grainstone carbonate package that dips northward (J3mc). Along this contact, localized areas of chaotic folding and color changes likely due to oxidation are present in unit J2tb. This contact has been previously mapped as both a fault (Bairamov et al., 2008; Bochud, 2011;

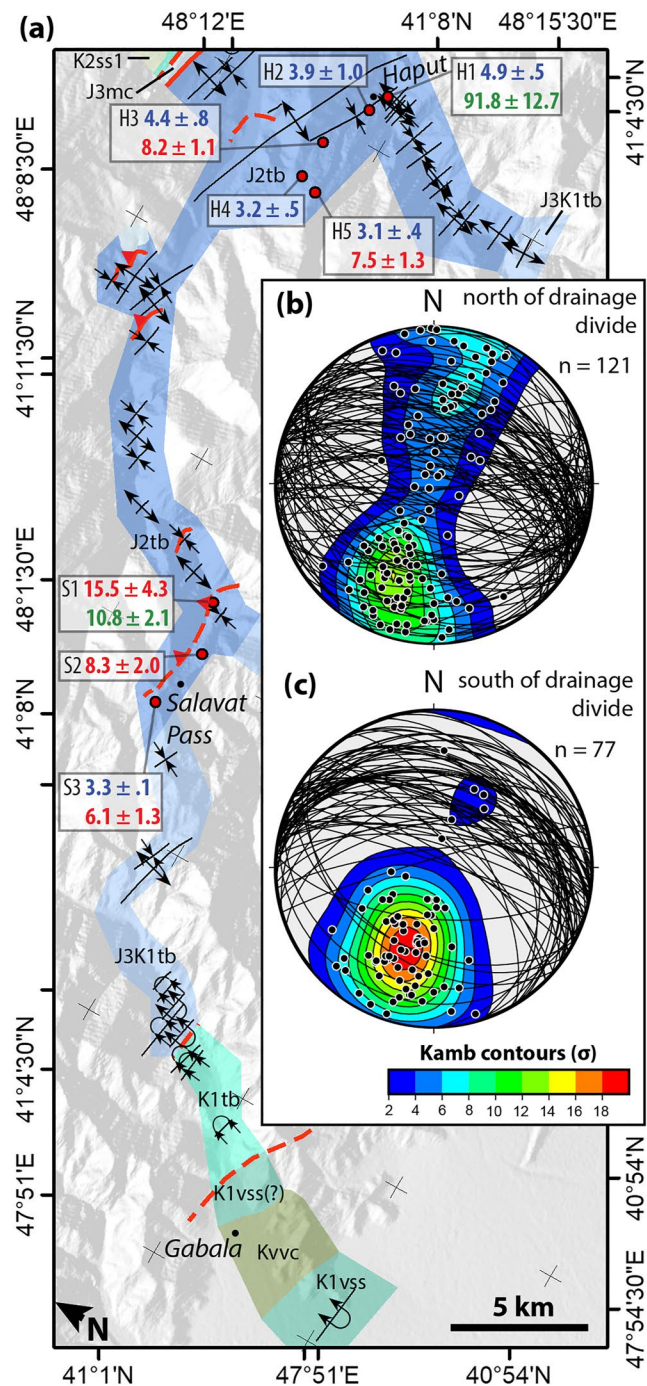


Figure 9. (a) Simplified geologic map and thermochronometric ages of the southern and central segments of the range-crest transect. See Figure 2b for location and <https://doi.org/10.6084/m9.figshare.19469873.v2> for the full size map with additional data. (b, c) Lower-hemisphere equal-area stereograms of bedding orientations in tightly folded sandstone and shale strata of the range-crest transect, including units J2tb, J3K1tb, and K1tb north (b) and south (c) of Salavat Pass, the range drainage divide. Great circles and points indicate bedding planes and their poles. Colors contour concentration of bedding plane poles (Kamb, 1959). Both plots include approximately the same number of measurements from north-younging and south-younging fold limbs. Bedding orientations are clustered south of Salavat, indicating that folds are nearly isoclinal, overturned, and southwest vergent. In contrast, bedding orientations north of Salavat define a broad girdle, indicating folds are more open. Plots were made using the Stereonet 11 software application (Cardozo & Allmendinger, 2013).

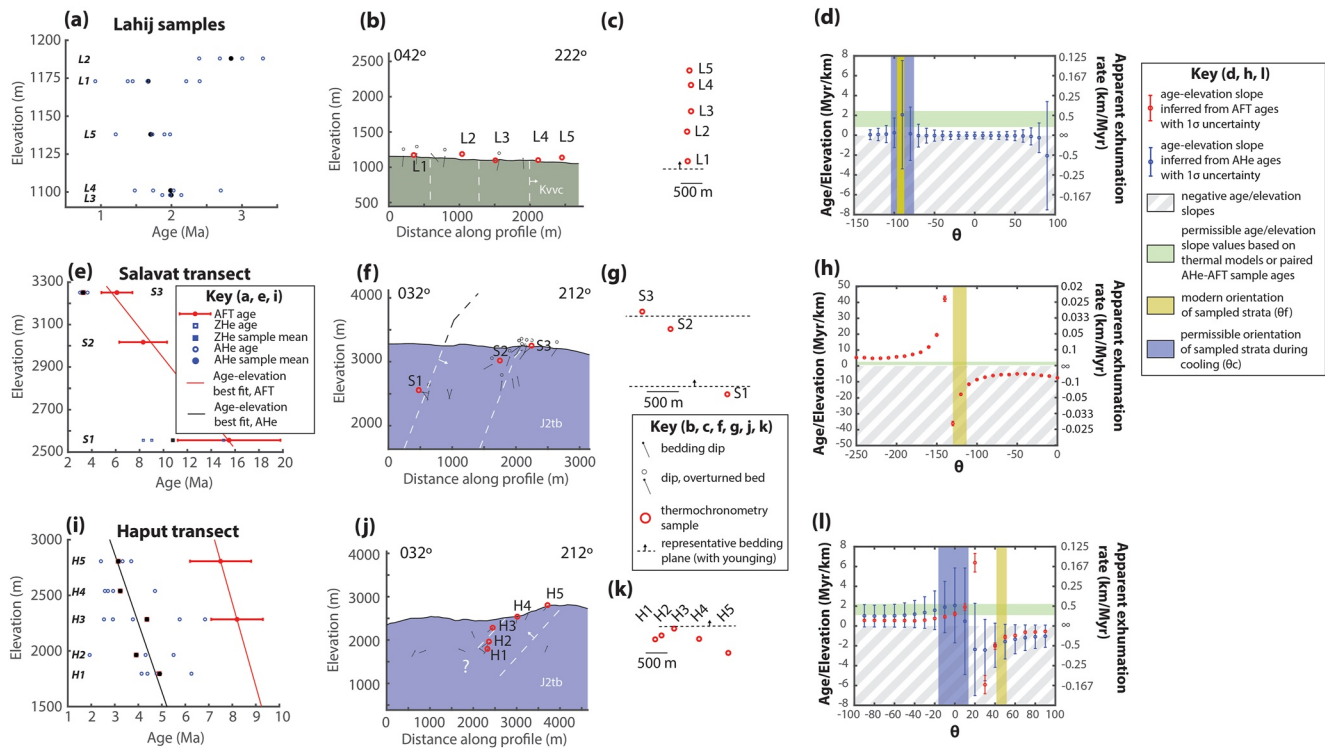


Figure 10. Paleo-rotation analysis of thermochronometry transects. (a, e, i) Age-elevation relationships for sample groups from Lahij, Salavat, and Haput. Pre-Cenozoic ages are not plotted. No age-elevation relationship is fit to the Lahij samples because they span <100 m elevation and thus do not define a vertical transect. (b, f, j) Cross-sections perpendicular to regional fold axes showing sample locations, topographic profiles, and bedding plane orientations. Azimuths listed in the upper left and right are the orientation of lines of cross section. (c, g, k) Analysis setup: sample locations and bedding in cross-sectional space rotated so that bedding is horizontal ($\theta = 0$). (d, h, l) Slope of the age-elevation relationship, which is equivalent to an apparent exhumation rate, plotted as a function of block rotation angle θ . Mean and standard deviation of age-elevation slopes are shown with symbols and error bars. Note that error bars in (h) are mostly smaller than symbols. Permissible late Cenozoic exhumation rates from thermal modeling (d; Lahij) or single-sample thermochronometric age differences (h, l; Salavat, Haput) are shown as green bars. Orientation values θ for which the age-elevation slope matches the values shown in green are marked with blue bars and are interpreted as permissible block orientations during cooling (θ_c). Modern observed orientations from bedding dip measurements (θ_p) are shown with yellow bars. See Figure 5 and Appendix A for further discussion.

Nalivkin, 1976) and an angular unconformity (Khain & Shardanov, 1960). In addition, Early Cretaceous submarine mass transport events are inferred to have displaced many km-scale blocks of J3mc that crop out in this area (Cumberpatch et al., 2021), in which case the J2tb-J3mc contact could be the slip surface of a massive submarine landslide. Our field observations are not sufficient to distinguish between these scenarios.

4.3.2.2. Thermochronometric Results and Interpretation

Thermochronometry samples collected from the central segment of the range-crest transect constitute two nearly vertical transects, one near Salavat Pass and a second near the village of Haput (Figures 2, 9a, and 10; Table 2). Both transects sampled the Middle Jurassic, organic-rich sandstone-shale succession (J2tb; Figure 9a). The shapes of analyzed mineral grains, especially apatite, reflect significant abrasion during sediment transport.

The Salavat thermochronometry transect (Figures 9a and 10e; Table 2, Tables S1 and S2) includes three samples that span ~800 m of elevation. Due to a dearth of mineral grains of sufficient size for (U-Th)/He dating, only the AFT system yielded ages from multiple samples. Sample S1 is the lowest in elevation and yielded a mean ZHe age of 10.8 ± 2.1 Ma and a central AFT age of 15.5 ± 4.3 Ma (Figure 10e; Table 2, Tables S1 and S2). Sample S2 is in the middle of the transect and yielded a central AFT age of 8.3 ± 2.0 Ma. Sample S3 is the highest in elevation and yielded a central AFT age of 6.1 ± 1.3 Ma and a mean AHe age of 3.3 ± 0.13 Ma. Note that the AFT ages have a negative age-elevation relationship. In sample S3, dividing the difference between the AHe and AFT ages by the difference in nominal closure temperatures of the two systems yields a cooling rate estimate of 12–33°C/Myr, equivalent to an exhumation rate of 0.4–1.7 mm/yr for possible geothermal gradients of 20–30°C/km.

Sample S1 yielding a ZHe age, 10.8 Ma, less than its AFT age, 15.5 Ma, is unexpected because the closure temperature of the ZHe system ($\sim 160^{\circ}\text{C}$ – 200°C) is greater than the AFT annealing temperature ($\sim 80^{\circ}\text{C}$ – 120°C ; Donelick et al., 2005; Reiners, 2005; Reiners et al., 2004). We interpret the young ZHe ages to result from a reduction in closure temperature due to radiation damage in the zircon crystals (e.g., Guenthner et al., 2013). Zircons in the Mesozoic sedimentary rocks of the eastern Greater Caucasus commonly have crystallization ages of 300–600 Ma (Tye et al., 2021). Given this age range and their compositions (U concentrations 200–1,200 ppm; Table S1), the range of potential alpha doses of these zircons is $\sim 5 \times 10^{17}$ – 4×10^{18} α/g , consistent with closure temperature reduction (Guenthner et al., 2013; Reiners, 2005).

Thermal modeling in QTQt (Gallagher, 2012) was carried out for sample S3 (see Table S3 for parameters). Thermal modeling of AHe and AFT ages from sample S3 reveals T-t paths with cooling from temperatures at or above the AFT annealing temperature (105°C – 195°C) at ca. 9 Ma to temperatures at or below the AHe closure temperature (10°C – 60°C) at ca. 4 Ma, at an average cooling rate of 11– $37^{\circ}\text{C}/\text{Myr}$. This cooling was followed by an apparent episode of minor reheating and cooling (Figure 8b). The modeled cooling rate from ca. 9–4 Ma is similar to the rate of 12– $33^{\circ}\text{C}/\text{Myr}$ inferred from the difference between the AFT and AHe ages and equates to exhumation rates of 0.37–1.85 mm/yr for geothermal gradients of 20– $30^{\circ}\text{C}/\text{km}$.

The Haput thermochronometry transect (Figures 9a and 10i; Table 2) is located to the north of the Salavat thermochronometry transect. The Haput transect consists of five samples spanning ~ 1 km of elevation, from H1 at the bottom to H5 at the top (Figure 10i; Table 2, Tables S1 and S2). Sample H1 has AHe and ZHe sample mean ages and standard errors of 4.9 ± 0.5 Ma and 91.8 ± 12.7 Ma, respectively; the AHe age for H2 is 3.9 ± 1.0 Ma; AHe and AFT ages for H3 are 4.4 ± 0.8 Ma and 8.2 ± 1.1 Ma, respectively; the AHe age for H4 is 3.2 ± 0.5 Ma; and AHe and AFT ages for H5 are 3.1 ± 0.4 Ma and 7.5 ± 1.3 Ma, respectively. Note that the AHe ages and the 2 AFT ages (H3 and H5) show a negative age-elevation relationship. Single-sample age differences between AHe and AFT ages from Haput transect samples provide first-order estimates of cooling (exhumation) rates of 10– $21^{\circ}\text{C}/\text{Myr}$ (0.33–1.05 mm/yr) for H3 and 9– $17^{\circ}\text{C}/\text{Myr}$ (0.3–0.85 mm/yr) for H5 (Table 1).

Thermal modeling was carried out using QTQt (Gallagher, 2012; parameters in Table S3) for sample H3. Modeling of AFT and AHe ages for sample H3 indicates well-constrained cooling since ca. 6 Ma at rates of $\sim 16^{\circ}\text{C}/\text{Myr}$ (Figure 8c). The cooling histories modeled for H3 are consistent with the long-term cooling rates implied by age differences between AFT and AHe thermochronometers for the Haput samples of ~ 10 – $20^{\circ}\text{C}/\text{Myr}$.

4.3.3. Northern Segment of the Range-Crest Transect

The northern segment of the range-crest transect extends northward from near the village of Jek (Figures 2 and 11a). Because the tectonic transport direction of thrusts in this segment is to the north, we proceed from north to south in discussing the geology. Results from one thermochronometric sample are reported from this transect.

4.3.3.1. Geological Description

Exposure is poor at the north end of the northern segment. Prior mapping indicates a north-dipping fold limb composed of Cenozoic strata in depositional (Khain & Shardanov, 1960) or fault (Nalivkin, 1976) contact with north-dipping Cretaceous strata to the south, although we did not observe this contact due to poor exposure and difficult access (Figure 11a). Exposed Lower Cretaceous strata (K1bc) consist of oolitic carbonate and interbedded gray shale (Figure 11a). This unit is exposed throughout much of the northern segment of the range-crest transect where it varies significantly, transitioning from >2 m thick carbonate beds with minor shale in the north to dominantly mudstone with irregularly spaced, discontinuous oolitic carbonate beds and lenses in the south. The unit contains submarine mass transport blocks of Upper Jurassic carbonate (J3mc; Figure 4g; Bochud, 2011; Cumberpatch et al., 2021). In the northern part of the northern segment, unit K1bc is deformed by a series of asymmetric folds with 0.5–1 km wavelength and northward vergence, as indicated by steeply north-dipping to overturned limbs containing strata that young to the north and moderately south-dipping limbs containing strata that young to the south (Figure 11a).

In the middle part of the northern segment, Jurassic to Cretaceous strata crop out in a structurally complex area containing several faults, steep angular unconformities, and km-scale submarine mass transport blocks emplaced during deposition (Cumberpatch et al., 2021; Gavrilov, 2018). A thrust sheet including Upper Jurassic massive carbonate (J3mc) and Lower Cretaceous bedded carbonate (K1bc) is thrust to the north along a fault, as mapped by previous workers (Bochud, 2011; Khain & Shardanov, 1960; Nalivkin, 1976), which we refer to as

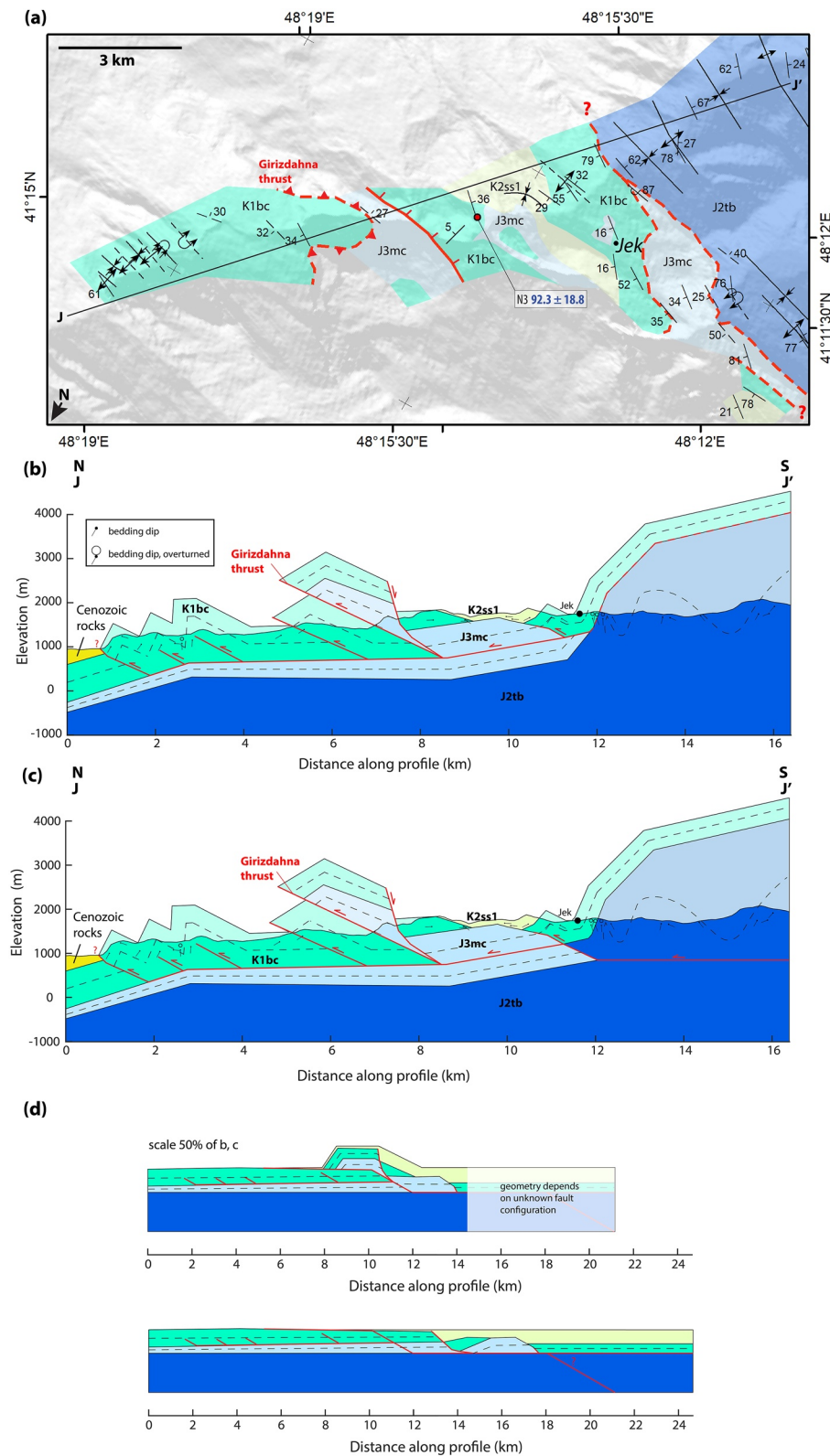


Figure 11. (a) Simplified geologic map and thermochronometric ages of the range-crest transect, northern segment. See Figure 2b for location and <https://doi.org/10.6084/m9.figshare.19469873.v2> for the full size map with additional data. (b, c) Cross sections showing two alternative structural interpretations of the fold-thrust belt exposed in the map area. The detachment could either remain on the K1bc-J2tb contact and not dip beneath the range core (b) or root into unit J2tb in the range core (c). (d) Sequentially retrodeformed cross sections with both fault geometries, shown at 50% scale of deformed sections.

the Girizdahna thrust. Units J3mc and K1bc in the hanging wall of the Girizdahna thrust are cut by a normal fault (Figures 4h and 11a) and unconformably overlain by Upper Cretaceous red to gray sandstone and mudstone of unit K2ss1 (Figures 4g and 11a; Khain & Shardanov, 1960; Nalivkin, 1976). The normal fault is well-exposed, dips to the south, and juxtaposes Upper Jurassic massive carbonate (J3mc) in the footwall against the overlying Lower Cretaceous succession (K1bc) in the hanging wall (Figures 4h and 11a).

At the south end of the northern segment, the Upper Jurassic (J3mc) and Lower Cretaceous strata (K1bc) are in contact with Middle Jurassic organic-rich shale and sandstone of unit J2tb. As noted above in the description of the central segment, this contact is disputed and has been mapped both as an unconformity (Khain & Shardanov, 1960) and a fault (Bairamov et al., 2008; Bochud, 2011; Nalivkin, 1976). Proposed km-scale Cretaceous olistolith emplacement in the vicinity may contribute to the complex geology (Bochud, 2011; Cumberpatch et al., 2021), though the presence of km-scale olistoliths is not the consensus view of all workers (Gavrilov, 2018).

4.3.3.2. Structural Interpretation

We interpret the asymmetric folds in unit K1bc in the northern part of the segment (Figure 11) as fault-propagation folds above north-vergent thrusts that root into a shared detachment near the base of K1bc (Figures 11b and 11c). To the south, the Girizdahna thrust places Upper Jurassic massive carbonate (J3mc) over unit K1bc and likely roots into this same detachment (Figures 11b and 11c). Retrodeforming this thrust system indicates a minimum of ~6 km of shortening (35%) within Upper Jurassic and younger strata (Figure 11d). We note that superposition relationships along this transect may be complicated by inferred motion of km-scale olistoliths near its southern margin, and slip planes of some particularly large olistoliths may have a similar field expression to faults (Bochud, 2011; Cumberpatch et al., 2021). Slip on the Girizdahna thrust is likely to be associated with tectonic faulting, rather than olistolith transport, because Lower Cretaceous strata in the footwall of the thrust (Figure 11) are observed to onlap, and thus post-date, a hypothesized olistolith to the south (Cumberpatch et al., 2021; Figure 4g). It is possible that the subsurface portion of unit J3mc may consist of discontinuous submarine mass transport blocks, rather than a continuous section, as we depict (Figures 11b and 11c). However, the presence and geometry of proposed olistoliths does not affect our minimum shortening estimates, which are based on fault-propagation folding of unit K1bc and offset on the Girizdahna thrust (Figures 11b and 11c).

Two basic geometries can be envisioned for the southern continuation of the basal thrust detachment, depending on the disputed contact relations between unit J2tb and overlying units J3mc and K1bc. If the exposed contact is an unconformity (Khain & Shardanov, 1960), then the thrust detachment roots into the core of the orogen (Figure 11c) and a thrust flat can be inferred to extend southwards in the subsurface for >6 km, from near the village of Jek to near the village of Haput (Figure 11c). Alternatively, if the exposed J2tb-J3mc/K1bc contact is a fault (Bairamov et al., 2008; Nalivkin, 1976), then it may be the basal thrust (Figure 11b). Localization of thrusting along the J2tb-J3mc/K1bc contact could result from lithologically controlled differences in deformation mechanisms, with short-wavelength folding in the underlying sandstone-shale package (J2tb; Figures 4c and 4d), and longer-wavelength fault-propagation folding of more mechanically competent strata in overlying units J3mc and K1bc. Alternatively, the difference in structural style across the contact could reflect unconformable deposition, with folding of the underlying sandstone-shale package prior to deposition of J3mc and thrust deformation.

The timing of slip on the normal fault is uncertain. Movement on the fault post-dates Early Cretaceous time, based on the age of the youngest observed faulted unit, K1bc. Early to Late Cretaceous slip would be consistent with inferred rifting in the Caucasus region (e.g., Nikishin et al., 1998, 2001). The geometries of the observed fault and hanging-wall bedding are consistent with a listric structure that soles into a detachment beneath the Upper Jurassic massive carbonate (J3mc; Figure 11), although other fault geometries are likely permissible.

4.3.3.3. Thermochronometric Results and Interpretation

We report a single AHe age from the northern segment of the range-crest transect (Figures 2 and 11a; Table 2). Sample N3 was collected from a sandstone within the Lower Cretaceous succession of predominantly oolitic carbonate and gray shale (K1bc; Figure 11a) and yielded a mean AHe age and standard error of 92.3 ± 18.8 Ma (Figure 11a; Table 2). We interpret this AHe age to indicate residence of the sample within 2–3 km of the surface since Cretaceous time, prior to formation of the Greater Caucasus (e.g., Adamia et al., 2011; Vincent et al., 2007).

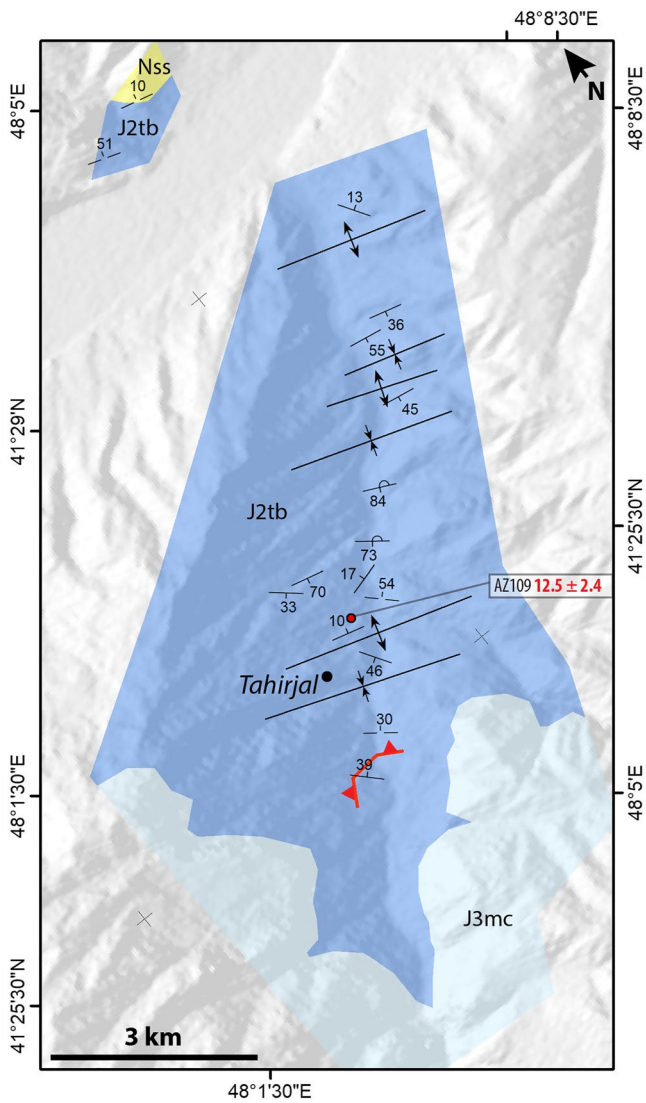


Figure 12. Simplified geologic map and thermochronometric ages of the Tahirjal transect. See Figure 2b for location and <https://doi.org/10.6084/m9.figshare.19469873.v2> for the full size map with additional data.

4.4. Tahirjal Transect Structural and Thermochronometric Data

The Tahirjal transect is ~30 km northwest of the northern end of the range-crest transect, on the eastern margin of a portion of the Greater Caucasus that is significantly wider across strike than the portion of the range that is the main subject of this study (Figures 2 and 12). Thermochronometric results have been previously reported (Bochud, 2011) for one sample from within the Tahirjal transect.

4.4.1. Geological Description

Strata exposed along the Tahirjal transect (Figure 12) are similar in lithology to those observed on the northern segment of the range-crest transect (Figure 11a). The oldest exposed unit is the Middle Jurassic, organic-rich, sandstone-shale succession (J2tb; Figure 12; Golubjatnikov & Dubogryzova, 1959; Nalivkin, 1976). Along the Tahirjal transect, this unit is deformed by tight (interlimb angles <90°), short wavelength (0.5–1 km) folds and small-offset thrusts (Figure 12). In the northern part of the transect, unit J2tb is unconformably overlain by Pliocene (Golubjatnikov & Dubogryzova, 1959) or Quaternary (Nalivkin, 1976) sandstone (Nss; Figure 12). In the southern part of the transect, unit J2tb is overlain by the Upper Jurassic massive carbonate succession (J3mc; Figure 12). In contrast to the pervasive folding and faulting of unit J2tb, the overlying J3mc has only gently inclined bedding and is relatively undeformed. The strong contrast in deformation style between these units is also observed in the northern segment of the range-crest transect (Figures 11a and 12). Bochud (2011) proposed the J2tb-J3mc contact is an angular unconformity in the Tahirjal area. If correct, such contact relations imply a phase of Middle to Late Jurassic shortening in this area.

4.4.2. Thermochronometric Results and Interpretation

The Tahirjal transect contains a single, previously reported AFT age of 12.5 ± 2.4 Ma from sample AZ109 of Middle Jurassic sandstone (J2tb; Figure 12; Table 2; Bochud, 2011). Thermal modeling of this age conducted by Bochud (2011) suggests that the Middle Jurassic sandstone-shale succession (J2tb) was exhumed during latest Miocene to Quaternary time.

4.5. Thermochronometric Data From Samples Outside Structural Transects

Several samples from outside the boundaries of our mapping transects have been analyzed for thermochronometric ages by Avdeev (2011; Table 2, Tables S1 and S2) and Bochud (2011). These samples are distributed along a roughly strike-parallel trend north of the Haput transect, near the northern exposed extent of the Middle Jurassic sandstone-shale succession (J2tb; Figure 2b). Three samples yielded sample mean AHe ages that range from 3.3 Ma to 6.3 Ma, similar to or slightly older than the AHe ages of the Haput transect (Figure 2b; Table 2, Table S1). Seven samples yielded AFT central ages ranging from 14 to 89.8 Ma, with five samples clustered between 30 and 50 Ma (Figure 2b; Table 2). It is important to note that all seven AFT samples failed the chi-square test for homogeneous age (Table 2, Table S2), suggesting the presence of more than one true fission track age population within the samples (Galbraith, 2005). Such populations reflect distinct, compositionally controlled annealing kinetics or inheritance of pre-depositional thermal histories (e.g., Galbraith, 2005). AFT ages of samples AZ089, AZ083 (Bochud, 2011), and N1 (Avdeev, 2011) decrease systematically southwards across strike, from 89.8 ± 9.8 Ma in the north (AZ089), to 41.8 ± 5.4 Ma in the middle (AZ083), to 14 ± 1.6 Ma in the south (N1). The stratigraphic distance between these samples is probably 1–2 km, based on our mapping of a structurally analogous area along strike. Although Bochud (2011) interpreted the age difference between AZ089 and AZ083 as evidence of fault offset between the samples, a plausible alternative hypothesis is that the three samples together reflect a fossil

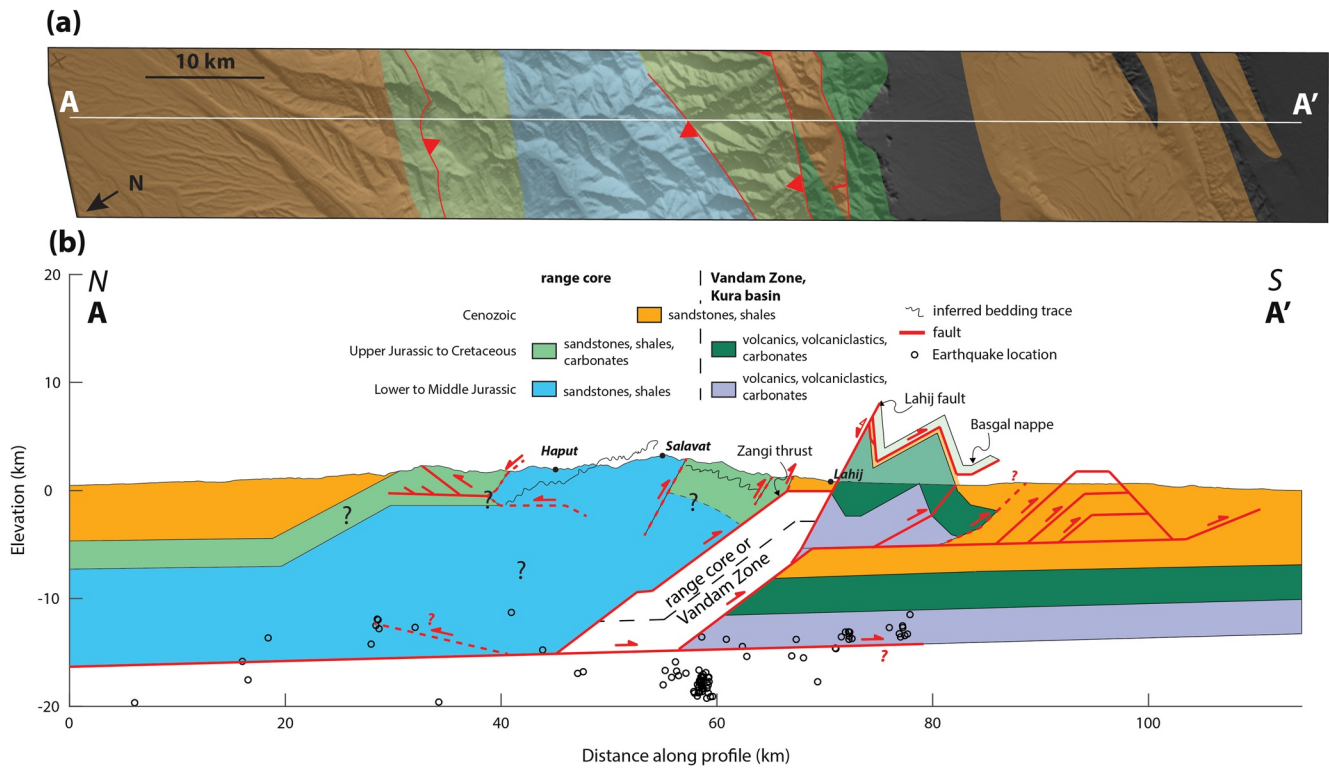


Figure 13. (a) Strip map along line A-A' (geology modified from Figure 2b). (b) Interpretive cross section of the structure of the entire range along the line A-A', based on compilation of observations and interpretations shown in Figures 7 and 11. Lithologic symbology is distinct from other figures in the paper. Deformation depicted within the southern foreland and within the fold-thrust belt on the northern margin of the range is balanced, as shown in Figures 7 and 11. Earthquake locations from within 20 km of line A-A' (Gunnels et al., 2021) are projected onto the cross section.

AFT partial annealing zone (e.g., Gleadow et al., 1986), based on the age gradient, estimated stratigraphic separation, and failure of the chi-square test (Table 2).

Thermal modeling of sample N1 provides additional insight into the exhumation history of the northern portion of the orogen (Figures 8d and 8e). Visual examination of a radial plot (Figure 8e) and mixture modeling (Galbraith, 1988; Galbraith & Green, 1990) indicate the presence of two separate AFT age populations in sample N1. Ages are poorly correlated with apatite composition (Figure 8e) and may reflect inheritance of differing age signals from sediment sources for the sampled sandstone, consistent with hypothesized residence of the sample in the AFT partial annealing zone before exhumation. We conducted thermal modeling of the two age populations separately, in each case together with available AHe data (Figure 8d). Each of the two separate AFT age populations passed the chi-square test for homogeneity (see Supporting Information for details). The models show initiation of cooling between ca. 9 and 3 Ma at rates of $\sim 10^{\circ}$ – 18° C/Myr (Figure 8d), broadly similar to the timing and cooling rates indicated by thermal models of the Salavat and Haput samples (Figures 8b and 8c).

5. Large-Scale Structure of the Eastern Greater Caucasus

Our mapping and cross sections, together with prior work, reveal the existence of two major faults, the Zangi and Vandam thrusts, which structurally bound the top and base, respectively, of the Vandam Zone package (Figures 7b and 13). As shown here, shortening of the Vandam Zone package was accommodated by fault offset of stratigraphically coherent thrust sheets (Figure 7b). Both the Vandam and Zangi thrusts have accommodated significant slip in the eastern Greater Caucasus (Figures 7b and 13).

On the Vandam thrust, we infer that large-magnitude slip was accommodated by shortening in the foreland thrust systems of Langabiz and Garmaryam ridges (Figures 7b and 13; Forte et al., 2013). In addition, the distribution of earthquake hypocenters beneath the eastern Greater Caucasus (Gunnels et al., 2021) suggests the presence of an additional seismogenic fault beneath the Vandam thrust (Figure 13). If the net offset on this deeper fault is

small, it may either connect updip to the Vandam thrust or terminate in a propagating fault tip (Figure 13), or the fault may continue beneath the Kura Basin (Mosar et al., 2010). These scenarios would be consistent with recent propagation of the orogenic wedge via forward breaking of the basal detachment (Figure 13).

On the Zangi thrust, the magnitude of slip is not directly constrained in the study area by preserved offset features, such as matching hanging-wall and footwall cutoffs. However, net slip on the Zangi thrust may be qualitatively assessed based on the approximate paleogeographic distance between the range-core succession and the Vandam Zone succession prior to deformation. Such an assessment depends primarily on interpretation of the paleogeographic position of the Vandam Zone, because we follow prior workers (e.g., Cumberpatch et al., 2021) in interpreting the northern flank and range-core successions as the ancient continental shelf and slope environments of Eurasia (Figure 3). The volcanic and volcanoclastic strata of the Vandam Zone and Kura basin may either represent sediment derived from the coeval Lesser Caucasus volcanic arc (e.g., Kopp & Shcherba, 1985; Rolland et al., 2011; Sosson et al., 2010), or rift magmatic sources between the Lesser Caucasus arc and Eurasia. If Vandam Zone sediment was derived from the Lesser Caucasus arc, then the Zangi thrust may accommodate significant offset related to the closure of a wide rift or oceanic basin (e.g., Cowgill et al., 2016). Likewise, geophysical evidence of subduction beneath the eastern Greater Caucasus (Mellors et al., 2012; Mumladze et al., 2015) suggests that the Zangi thrust may have served as a subduction zone megathrust with large-magnitude slip while it was active. However, if Vandam Zone volcanic detritus was derived from a rift source, the lithologic differences between the range-core and Vandam Zone successions may reflect structurally controlled bathymetry and local volcanic centers (e.g., Mosar et al., 2022). In the western Greater Caucasus, some authors hypothesize that thrusts juxtaposing distinct tectono-stratigraphic packages are re-activated, basin-forming normal faults of the Greater Caucasus Basin (e.g., Mosar et al., 2022; Saintot, Brunet, et al., 2006; Vincent et al., 2016; although Trexler et al., 2022, demonstrated that the structure of the western Greater Caucasus is consistent with that expected for an imbricate fan built from a stack of large-slip thrusts). Similarly, it is plausible that the Zangi thrust was the southern bounding fault of the eastern portion of the Greater Caucasus Basin, into which the range-core succession was deposited. In this case, net offset on the Zangi thrust could be relatively small.

The shale-rich rocks that constitute the core of the eastern Greater Caucasus are structurally above the Zangi thrust and have a structural style dominated by short wavelength folding and axial-planar cleavage development (Figures 4c–4f and 9a). The upright geometry of many of these folds (Figure 9b) is inconsistent with a fault-propagation folding mechanism, and the correlation of fold wavelength with bedding thickness in some locations suggests buckling as a dominant folding mechanism. These observations demonstrate that a significant fraction of shortening within the core of the range is accommodated by pervasive folding rather than by fault displacement within a typical fold-thrust system.

The structure of the northern flank of the orogen is more poorly constrained than the southern flank (Figure 13). It is unclear how the exposed, north-vergent fold-thrust belt is connected to deeper structures of the orogen (Figures 11 and 13). The structural relief between the folded Mesozoic strata and the buried, correlative strata north of the Greater Caucasus is constrained by the thickness of the Cenozoic section, interpreted west of the study area from seismic images to be ~4–6 km (Sobornov, 2021; Figure 13). Interpreted seismic sections from eastern Dagestan, 50–100 km NW of the study area (Sobornov, 2021) and the Apsheon Sill, a subaqueous fold-thrust belt parallel to the Greater Caucasus in the Caspian Sea (T. Green et al., 2009; see Figure 2a for approximate locations) find poorly developed north-vergent thrust systems with few faults and net offset \lesssim 10 km. We infer that a similar, simple thrust system is likely to exist beneath the northern flank of the eastern Greater Caucasus in our study area, although its geometry is poorly constrained (Figure 13).

5.1. Minimum Shortening Estimate for the Eastern Greater Caucasus

Combining the amount of slip inferred on major thrusts with the magnitude of shortening interpreted to be accommodated by folding in the intensely deformed strata in the core of the eastern Greater Caucasus yields a minimum estimate of upper-crustal shortening in the study area. As discussed above, slip on the Zangi and Vandam thrusts, together with shortening within the Vandam Zone, is inferred to accommodate >34 km shortening (Figure 7b). On the northern flank of the orogen, thrusts shorten Mesozoic strata by >6 km (Figure 11). In sum, >40 km of shortening is attributed to recognized fault systems in the eastern Greater Caucasus.

In the core of the range, we estimate fold-related shortening by reconstructing an approximate bedding trace drawn parallel to orientations observed at the surface, which yields >35% horizontal shortening (Figure 13). We ignore faulting for the purpose of calculating shortening within the range core because our field observations from the area do not constrain the magnitude of macro-scale fault slip. The exposed belt of folded and faulted Jurassic to Middle Cretaceous shale-rich strata of the range core is ~30 km wide across-strike within the study area (Figure 13). Thus, folding in the range core potentially accounts for at least 16 km of shortening (Figure 13). In addition, development of pervasive axial-planar cleavage in the orogen core (Figure 4f) can be reasonably attributed to 10%–20% volume loss (e.g., Ramsay & Wood, 1973; Sorby, 1908), accounting for another 5–11 km of shortening. Therefore, we estimate at least 21–27 km of shortening by folding and cleavage formation in the central to northern part of the range (Figure 13). Combining these estimates indicates >61 km of total shortening in the eastern Greater Caucasus.

6. Thermochronometric Block-Rotation Modeling

We applied a novel thermochronometric block-rotation analysis (Figure 5; Appendix A) to three thermochronometric sampling transects in the eastern Greater Caucasus, the Lahij, Salavat, and Haput transects (Figures 2 and 10), to infer spatial variations in the timing and rates of exhumation and deformation. The block-rotation analysis method permits inference of the relative ages of exhumation and tilting (Figure 5), which we use to better constrain the deformation histories of specific parts of the orogen. This block-rotation modeling supplements the inverse thermal modeling conducted for selected samples, described above.

6.1. Lahij Thermochronometric Transect

The Lahij samples were collected along a horizontal transect within the northern limb of an overturned syncline (Figure 7). To explore the temporal relationship between folding and cooling, we compare the exhumation rate implied by the age-elevation relationship of the samples as a function of rigid-block fold limb rotation (Figure 5; Appendix A) with the exhumation rate obtained independently from thermal modeling of sample L2 (0.4–1.25 mm/yr; Figure 8a). Lahij samples L1, L2, L3, L4, and L5 have sample mean AHe ages between 1.5 and 3.0 Ma, and elevations from which they were collected vary by <100 m (Figure 10a). These samples were collected from an approximately horizontal transect from bedrock of unit K_{vvc} that has been tilted during folding such that bedding is subvertical (Figure 10b). Rotating a rigid block containing these sample locations relative to an initially horizontal bedding orientation (Figure 10c) results in a range of apparent exhumation rates, solved for via least squares fit of the age-elevation relationship (Figure 10d). For rotation of the Lahij samples, modeled age-elevation relationships are compatible with exhumation rates inferred from thermal modeling only for the present orientation of the samples, $\pm 20^\circ$ (Figure 10d). In the case of these samples, because of the narrow range of AHe ages and sample elevations, other orientations for the sampled block result in very large elevation-age gradients, which are inconsistent with thermal modeling of sample L2 (Figure 10d). The model results for the Lahij samples suggest that the sampled block was in its current orientation during cooling and are consistent with the hypothesis that fault propagation folding rotated the sampled block into its present orientation prior to exhumation, which began between ca. 8 and 3 Ma (Figure 14a).

6.2. Salavat Thermochronometric Transect

Salavat samples are arrayed in a vertical transect and show a negative age-elevation gradient (Figures 2 and 10e), the opposite of that expected for an exhuming rigid block (Figure 5; e.g., Brandon et al., 1998; Farley et al., 2001). Because the samples are located on the overturned limb of a fold (Figures 10f and 10g), we use our block rotation model to determine if the negative age-elevation gradient can be explained by fold-related tilting of the sampled strata after cooling.

Applying our block-rotation modeling approach (Figure 5; Appendix A) to the Salavat AFT ages helps to explain age-elevation relationships, but the results are somewhat more ambiguous than for the Lahij or Haput transects. Positive age-elevation gradients are obtained for paleo-orientations $\theta_c < -140^\circ$, which is equal to a <40° NNE overturned bedding dip (Figure 10h). However, the age-elevation gradients obtained by rotating the AFT samples (<0.15 mm/yr; Figure 10h) do not overlap with exhumation rates inferred from AHe-AFT age differences and thermal modeling of sample S3 (>0.37 mm/yr; Figure 8b). This discrepancy indicates either that

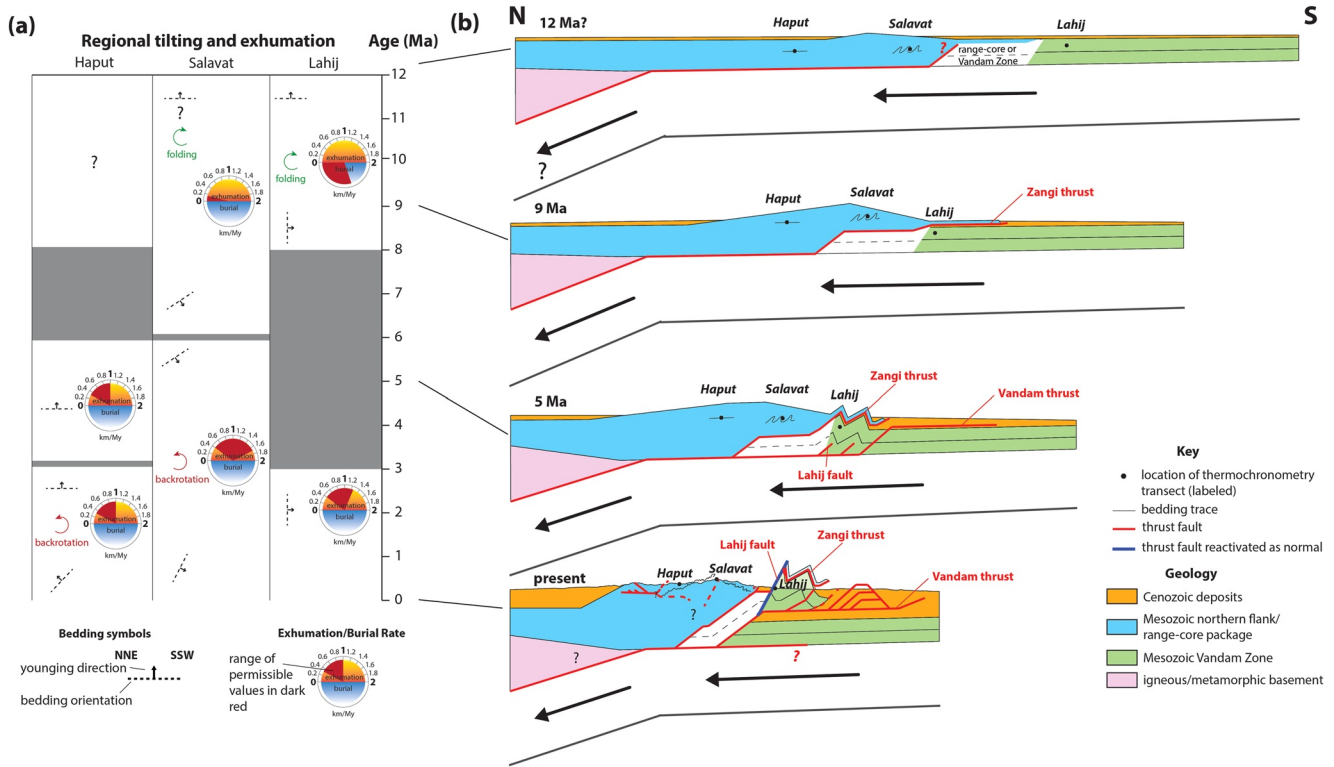


Figure 14. (a) Constraints from thermochronometry on the structural development of the regions of the Lahij, Salavat, and Haput transects, based on thermochronometry data and paleo-rotation analyses. For each of the three thermochronometry transects, a tilting and exhumation history is constructed that satisfies constraints from thermal modeling (Figure 8) and constraints on block orientation during cooling (Figure 10). Distinct periods of exhumation are delineated over time for each transect, with tilting depicted using arrows and initial (upper) and final (lower) bedding orientations in a NNE-SSW cross-sectional view. Exhumation and/or burial rates are depicted using an odometer, where the dark red area represents permissible exhumation or burial rate. Gray bars separate resolvable periods of distinct tilting and exhumation trends. Note that timing of the initial folding of Salavat transect strata into an overturned position is poorly constrained, and such folding may have occurred before 12 Ma. (b) Diagram of the structural evolution of the eastern Greater Caucasus orogen based on thermochronometric data and the structural model shown in Figure 13. The Vandam Zone strata are line-balanced, and the range-core strata, excluding the Basgal nappe, are approximately area balanced, but the evolution of finite shortening over time in the orogen is not well constrained. Approximate locations of three thermochronometric transects at Haput, Salavat, and Lahij, are marked over time.

the age-elevation slope of AFT samples is not indicative of exhumation rates or that exhumation rates changed over time. In either case, any paleo-orientation angle θ_c that corresponds with a negative age-elevation gradient ($\theta_c \geq -130^\circ$; Figure 10h) can be rejected. Although the constraints on the paleo-orientation angle are poor, they are consistent with the following geologically reasonable interpretation. The sampled Salavat block may have cooled at a paleo-orientation angle of $\theta_c = -140^\circ$ to -150° , equal to a 40° – 30° NNE overturned bedding dip, which corresponds with a positive age-elevation gradient (Figure 10h) and differs only 20° – 30° from the modern orientation (θ_p) of -121° (59° NNE, overturned bedding dip; Figure 10f). Such a paleo-orientation is comparable with the bedding dip of many overturned fold limbs observed in the Jurassic to Cretaceous strata of the range core (Figures 4 and 7). Following cooling, 20° – 30° top-to-the-north rotation would be required for the Salavat transect to reach its current orientation (Figure 10h). Such top-to-the-north rotation is consistent with passive rotation above a thrust ramp, such as a ramp in the Vandam thrust that may underlie the transect (Figure 13). The block-rotation analysis for the Salavat samples suggests slow exhumation (<0.05 mm/yr) or isothermal holding in the partial annealing zone in an overturned position during the interval from ca. 15 to ca. 6 Ma (Figures 10e and 10h), and thermal modeling of sample S3 indicates the initiation or acceleration of cooling between ca. 9 and 6 Ma (Figure 8b). These results can be reconciled by a deformation history that includes slow exhumation or isothermal holding and folding into an overturned, north-dipping orientation prior to ca. 6 Ma, followed by exhumation of 0.4–1.7 mm/yr and passive back-rotation above the Vandam thrust after exhumation through the partial annealing zone (Figure 14a).

6.3. Haput Thermochronometric Transect

The AHe and AFT ages of the Haput transect decrease with increasing elevation (Figures 9a and 10i; Table 2). Because all Haput samples were collected from the northern limb of an anticline (Figure 10j), we use our block-rotation modeling approach to explore whether post-cooling tilting during folding explains the unexpected age-elevation distribution. The Haput vertical thermochronometric transect sampled beds that presently dip 47°NNE (Figure 10j). Rotation of a rigid block containing the sample locations of the Haput transect relative to an initially horizontal bedding dip (Figure 10k) yields a range of age-elevation gradients, which can be compared to independent estimates of exhumation rates (Figure 10l). Syn-cooling paleo-orientations from $\theta_c = 10^\circ$ to $\theta_c = -20^\circ$, which correspond with low-angle bedding dips from 10°NNE to 20°SSW, yield AHe and AFT age-elevation relationships consistent with the exhumation rates of ~0.3–1.0 mm/yr inferred from single-sample AHe and AFT age differences in samples H3 and H5 (Figure 10l) and thermal modeling of sample H3 (Figure 8c). Thus, the observed ages of the Haput transect are consistent with cooling when the sampled strata were approximately flat lying, followed by post-cooling tilting after ca. 3 Ma, which is the youngest AHe age from this transect (Figure 14a). Such a deformation history may reflect tilt within the forelimb of a fault-bend fold if the sampled rock package is underlain by a north-vergent thrust system (Figures 11c and 13), although ongoing pervasive folding within the wedge interior may also have caused the inferred tilting.

7. Timing and Rates of Exhumation and Deformation

New and previously published thermochronometric and structural data constrain the timing of initial exhumation in the eastern Greater Caucasus, accretion of the Vandam Zone tectonostratigraphic package, and folding within the range interior. The constraints discussed in this section contribute to a schematic model of the structural evolution of the range (Figure 14).

7.1. Pre-Orogenic Thermal Evolution and Initiation of Deformation Within the Eastern Greater Caucasus

Contractional deformation within the eastern Greater Caucasus began during Paleogene time or later, following a dominantly extensional regime that lasted from Mesozoic until Paleogene time (Mosar et al., 2022; Nikishin et al., 1998; Vincent et al., 2016; Zonenshain & Pichon, 1986). As described above, pre-Neogene thermochronometric ages can be attributed to insufficient burial for complete age resetting. Thermal modeling of sample S3, from the range core, suggests initiation of cooling by ca. 9 Ma (Figure 8b), and AFT ages as old as 15.5 ± 4.3 Ma may reflect ongoing exhumation by that time (Figures 10e and 10h). Thus, the thermochronometric data suggest that deformation and exhumation were ongoing by Middle to Late Miocene time (Figure 14).

The earliest phase of Cenozoic deformation in the eastern Greater Caucasus preceded accretion of the Vandam Zone package (Figure 14b). Prior to accretion of the Vandam Zone, shortening within the orogen was likely accommodated by slip on the Zangi thrust, which developed a damage zone >500 m thick (Figure 7b). Given its structural position immediately above the Vandam Zone package, the Zangi thrust is likely to have been the basal detachment of the orogen prior to Vandam Zone accretion (Figure 14b).

7.2. Vandam Accretion and Initiation of Slip on the Vandam Thrust

Geological and thermochronometric data constrain the timing of accretion and deformation of the Vandam Zone. Deformation of the Vandam Zone package passively folded the structurally overlying Zangi thrust, which was emplaced after 12.7 Ma (Khain & Shardanov, 1960), into a configuration unlikely to accommodate additional slip (Figure 7b). Thermochronometric data and modeling indicate that exhumation of the Vandam Zone within the eastern Greater Caucasus orogen began between ca. 8 and 3 Ma, after folding into its modern orientation (Figures 8a and 10a–10d). Available ages thus bracket accretion of the Vandam Zone package and initiation of slip on the Vandam thrust to between 12.7 Ma and ca. 3 Ma (Figure 14b).

The initiation of slip on the Vandam thrust between 12.7 Ma and ca. 3 Ma suggests that slip on the thrust may have begun prior to initiation of deformation in the foreland fold-thrust belt at ca. 2 Ma (Forte et al., 2010, 2013). This inconsistency suggests that from the age of Vandam accretion until 2 Ma, shortening may have been accommodated via out-of-sequence deformation in the prism interior or potentially via an unrecognized fault.

7.3. Out-of-Sequence Deformation Within the Prism Interior, Lahij Normal Faulting, and Foreland Thrust Belt Initiation Following Vandam Zone Accretion

Our thermochronometric data show evidence of out-of-sequence deformation in the prism interior. In particular, the AHe ages of the Haput transect suggest that the sampled strata were approximately flat lying when they cooled sometime following ca. 6 Ma (Figure 8c), after which they were tilted into their present orientation, dipping 47°NNE (Figure 10j), after ca. 3 Ma (Figure 14a). This folding could accommodate as much as 32% horizontal shortening, based in the difference in horizontal extent between a unit length and the same length tilted 47°. Thermal modeling of sample N1 (Figures 8d and 8e) indicates initiation or acceleration of cooling between ca. 8 and 3 Ma, coeval with exhumation of the Vandam Zone package (Figure 14b). Out-of-sequence deformation may explain an apparent northward shift in the locus of surface uplift inferred from river network geometry in the eastern Greater Caucasus (Forte et al., 2015).

We infer that the Lahij fault has accommodated normal slip (Figure 14b) based on younger-over-older unit juxtapositions (Figure 7b), reported fault kinematic data for nearby structures within the Vandam Zone package (Bochud, 2011), and an apparent normal shear-sense indicator (Figure 4b). Normal-sense Lahij fault slip likely followed accretion and contractional deformation of the Vandam Zone (Figures 14a and 14b). Slip on the fault was probably coeval with or postdated exhumation of the Vandam Zone thermochronometry samples, thus beginning <8 Ma (Figures 8a, 14a, and 14b). Extensional deformation has not been inferred from GPS measurements within the eastern Greater Caucasus (Kadirov et al., 2012, 2015) or upper-plate earthquake focal mechanisms (Gunnels et al., 2021) and so has likely ceased or is too minor to be recognized in existing geophysical data sets. Extension in the interior of an orogenic wedge has been proposed to accommodate heterogeneous thickening of the wedge by basal accretion (e.g., Grando & McClay, 2007; Platt, 1986). Malavieille et al. (2021) note the presence in Taiwan of normal faults that dip toward the orogenic hinterland on the margin of an antiformal thrust stack and explain these normal faults as accommodating focused exhumation above the antiformal stack. The setting of such faults is similar to the Lahij fault, which is above a ramp in the Vandam thrust (Figure 13). We hypothesize that normal-sense Lahij fault slip compensates for focused rock uplift above the Vandam fault footwall ramp.

Deformation of the foreland fold-thrust belt structures exposed at Langabiz and Garmaryam is inferred to have begun ca. 2 Ma based on cross cutting relationships with regional chronostratigraphic units (Forte et al., 2013). We infer that this deformation occurred in the hanging wall of the Vandam thrust (Figure 7) following accretion of the Vandam Zone package. Together, we infer that the out-of-sequence deformation in the orogen interior, localized extension within the thick, accreted Vandam Zone package, and propagation of thrusting into the foreland described here reflect heterogeneous effects of focused rock uplift on an orogenic wedge. Rock uplift above the Vandam thrust ramp, which disrupts the tapering profile of the wedge, corresponds spatially with normal-sense slip on the Lahij fault, whereas shortening persists in regions toward the foreland and hinterland of the wedge.

8. Discussion

8.1. Implications for Greater Caucasus and Arabia-Eurasia Tectonics

The magnitude and rate of convergence accommodated by subduction beneath, and shortening within, the Greater Caucasus have implications for the timing and evolution of Arabia-Eurasia collision (e.g., Cowgill et al., 2016; McQuarrie & van Hinsbergen, 2013). GPS data show significant along-strike variation in present-day convergence rate, from ~4 mm/yr in the west to >12 mm/yr in the east (Forte et al., 2014; Reilinger et al., 2006; Figure 2a). An along-strike variation in total convergence, from 200 to 280 km in the west to ~120 km in the east, is interpreted from paleomagnetic vertical-axis rotations attributed to lower plate oroclinal bending (van der Boon et al., 2018; Figure 15). Our findings, when combined with recent structural studies of the western Greater Caucasus (Figure 15; Trexler, 2018; Trexler et al., 2022), have implications for understanding these along-strike variations and the relationship between shortening and convergence.

8.1.1. Along-Strike Variation in Greater Caucasus Total Shortening and Convergence

Our estimated minimum horizontal shortening of >61 km in the eastern Greater Caucasus is lower than the 170–230 km minimum accommodated by thrusting in the western Greater Caucasus (Trexler, 2018; Trexler et al., 2022; Figure 15). This variation in shortening is consistent with along-strike differences in convergence

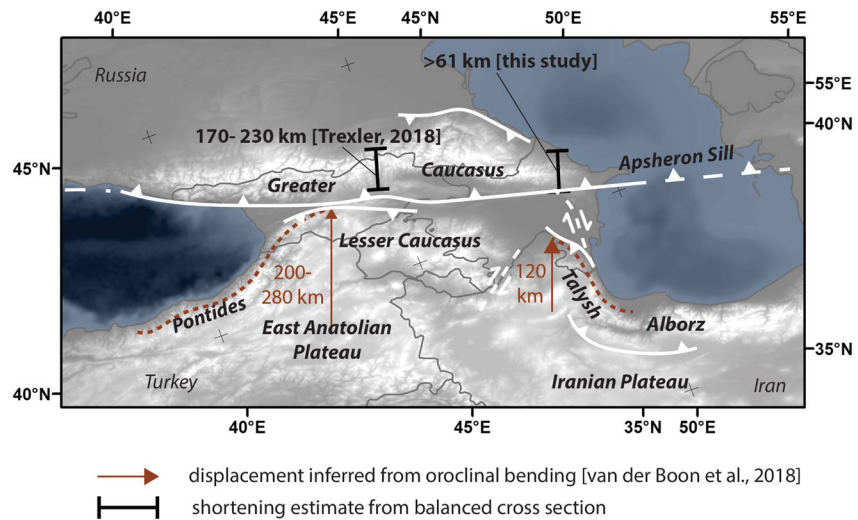


Figure 15. Map of the Caucasus region showing available constraints on Cenozoic shortening and convergence for different parts of the range. Tectonic components are labeled in black, faults are shown in white.

between the eastern Greater Caucasus (~120 km) and the western Greater Caucasus (200–280 km) inferred from paleomagnetic evidence of lower-plate oroclinal bending (van der Boon et al., 2018; Figure 15).

There are several potential causes for along-strike variations in shortening and convergence in the Greater Caucasus. One potential cause is a possible along-strike difference in the duration of deformation. Paleocurrent orientations (Vincent et al., 2007) and thermochronometric evidence (Avdeev & Niemi, 2011) suggest that western Greater Caucasus deformation and uplift began 35–30 Ma, whereas our thermochronometric data indicate that deformation-induced exhumation of the eastern Greater Caucasus may have commenced as late as ca. 15–9 Ma, as discussed above (Figure 14). Such a difference in duration could result in different finite shortening. Alternatively, some of the along-strike variation in shortening could be due to a difference in how total convergence is partitioned between subduction and upper-plate shortening (e.g., Cowgill et al., 2016; Gunnels et al., 2021). As noted above, it is possible that the Zangi thrust accommodated significant convergence via subduction that is not recorded by upper plate shortening, based on the structural juxtaposition of similarly aged rocks with distinct lithology between the range core and Vandam Zone (Figures 13 and 14b). Subduction along the Zangi thrust may help explain some of the difference between shortening (>61 km) and plate convergence (~120 km; van der Boon et al., 2018) in the eastern Greater Caucasus (Figure 15).

Along-strike differences in convergence and timing of deformation in the Greater Caucasus reflect along-strike differences in the spatio-temporal distribution of deformation within the Arabia-Eurasia collision zone (Figure 15). Initiation of deformation in the eastern Greater Caucasus (potentially as late as ca. 9 Ma) may coincide with changes in the style and rate of deformation in several other components of the Arabia-Eurasia collision zone. Extrapolating neotectonic slip rates of faults associated with subduction of the South Caspian Basin beneath the Apsheron Sill, which is located along strike from the eastern Greater Caucasus (Figure 15), suggests that ca. 10 Myr of slip is required to account for observed net offset (Hollingsworth et al., 2008). Deformation in the Alborz and Talysh mountain ranges, south of the eastern Greater Caucasus (Figure 15), is inferred from thermochronometric and stratigraphic records to have intensified at 12 Ma (Guest et al., 2006, 2007; Madanipour et al., 2017). At 12 Ma, deformation began or intensified in the Zagros Folded Belt on the southern margin of the Arabia-Eurasia collision zone (Mouthereau, 2011). Intraplate deformation in northwestern Iran began in Middle to Late Miocene time (Morley et al., 2009). Simultaneous with the initiation or intensification of shortening in these components of the Arabia-Eurasia collision zone, thermochronometric ages record a 12 Ma slowing of exhumation in the Sanandaj-Sirjan Zone, the suture zone between Arabia and Eurasia (Barber et al., 2018). Together, the available evidence indicates that around 12 Ma, deformation associated with Arabia-Eurasia collision migrated from the suture zone into other structural systems in the upper and lower plates (e.g., Barber et al., 2018), potentially including the eastern Greater Caucasus—Apsheron Sill system. This migration of deformation is hypothesized

to be related to changes in gravitational potential energy driven by breakoff of the Neotethys slab (Francois et al., 2014) and thinning of the lithosphere beneath the Iranian plateau (Hatzfeld & Molnar, 2010).

The initiation of convergence in the western-central Greater Caucasus around 35–30 Ma (Adamia et al., 2011; Avdeev & Niemi, 2011; Vincent et al., 2007) suggests that shortening may have been accommodated there since the initiation of Arabia-Eurasia collision (e.g., Allen & Armstrong, 2008; Barber et al., 2018; McQuarrie and van Hinsbergen, 2013). In contrast, at the longitude of the eastern Greater Caucasus and Apsheron Sill, deformation may have propagated from the Arabia-Eurasia suture to the north >20 Myr later. This difference in timing may be due to along-strike differences in pre-collisional margin geometry or the distribution of continental fragments involved in the collision zone (e.g., van Hinsbergen et al., 2020).

8.1.2. Effects of Greater Caucasus-Lesser Caucasus Collision

Structural and thermochronometric data are interpreted to suggest that thicker and more buoyant crust began subducting beneath the western Greater Caucasus beginning in Middle Miocene to Late Miocene time, initiating collision between the Greater Caucasus and the Lesser Caucasus in the western part of the orogen (Avdeev & Niemi, 2011; Cowgill et al., 2016; Philip et al., 1989; Tye et al., 2021). The initiation of collision in the western Greater Caucasus resulted in Late Miocene initiation or acceleration of deformation in foreland fold-thrust belts on the northern and southern flanks of the orogen (e.g., Banks et al., 1997; Gusmeo et al., 2021; Sobornov, 1994, 2021) and a Pliocene increase in upper-plate exhumation rates inferred from thermochronometry (Avdeev & Niemi, 2011; Vincent et al., 2020).

Our new thermochronometric and structural evidence indicate that beginning in Late Miocene time, the eastern Greater Caucasus was affected by accretion of the Vandam Zone package, out-of-sequence deformation and accelerating exhumation within the orogen interior, normal-sense slip on the Lahij fault (Figures 13 and 14b), and initiation of foreland fold-thrust belt deformation (Forte et al., 2013). The Late Miocene-Pliocene accretion and increased exhumation within the eastern Greater Caucasus are broadly similar to and coeval with fold-thrust belt development and accelerated exhumation in the western Greater Caucasus, which are interpreted to be caused by collision with the Lesser Caucasus (Cowgill et al., 2016; Tye et al., 2021). However, at the longitude of our study area, the Greater and Lesser Caucasus are separated by the subducting (Mellors et al., 2012; Mumladze et al., 2015), mafic to oceanic crust of the Kura Basin (Gunnels et al., 2021). Thus, the Late Miocene-Pliocene evolution of the eastern Greater Caucasus at the longitude of our study apparently cannot be attributed to entrance of lower-plate continental crust into the subduction zone. These results, together with the recent recognition that exhumation rates appear to be equivalent in both pre- and post-collisional portions of the orogen (Forte et al., 2022), underscore the need for further study of how continental collision affects the structural evolution of orogens.

8.2. Lithologic Control of Structural Style

A first-order observation from the eastern Greater Caucasus is that deformation mechanisms differ between the Vandam Zone, which is affected by fault offset of stratigraphically coherent thrust sheets (Figure 7), and the range core, which is affected by pervasive, complex, short-wavelength folding (Figures 4c–4f and 13). Because these two rock packages are part of the same orogenic wedge and share a single set of tectonic and erosional boundary conditions, the difference in deformation style likely relates to lithologic effects on the mechanical properties of the two packages. The pervasively folded range-core package is composed of thin-bedded (<10 cm) sandstone and shale, whereas the Vandam Zone package is dominated by sandstone and volcanic beds up to several meters thick with minor shale. Within the eastern Greater Caucasus, therefore, fold wavelength is broadly correlated with the thickness of folded sedimentary rock layers. Large-magnitude thrust slip seems mostly to occur in structural packages with larger-wavelength folds (Figure 13). A correlation between fold wavelength and bed thickness has been observed in mechanical experiments (Currie et al., 1962). In addition, differences in deformation style have been documented between lithologically distinct portions of orogenic wedges such as the Zagros orogen (Casciello et al., 2009) and the Mexican fold-thrust belt (Fitz-Diaz et al., 2012). Our observations add to the body of work demonstrating that lithologic contrasts can cause dramatic differences in structural style within a single orogen.

8.2.1. Different Modes of Accretion

Orogenic wedges are recognized to undergo two distinct modes of accretion, frontal accretion, in which accreted material is added to the toe of the wedge, and basal accretion, in which lower plate material is underthrust beneath the wedge prior to accretion (e.g., Gutscher et al., 1998; Malavieille, 2010; Platt, 1986). Repeated accretion of thrust sheets to the base of the orogenic wedge causes formation of antiformal thrust stacks (Malavieille, 2010; Malavieille et al., 2021; see Figure 1a Himalaya cross section for example). Many of Earth's orogens, including the Himalaya (Lavé & Avouac, 2000), Taiwan (Malavieille et al., 2021), and the Alps (Burkhard & Sommaruga, 1998), undergo basal accretion and contain large antiformal thrust stacks. In the eastern Greater Caucasus, Vandam Zone strata are added to the wedge via basal accretion after underthrusting (Figures 13 and 14). Future accumulation of slip on a new thrust beneath the Vandam thrust, which may have already formed (Figure 13), will result in the growth of an antiformal stack of Vandam Zone/Kura basin thrust sheets. In the deformed range-core succession, an apparent lack of large-offset thrusts suggests that frontal accretion was the dominant mode of addition of material (Figures 9a and 13). The accommodation of frontal accretion by pervasive folding is compatible with seismic images of active accretionary prisms that show progressive stratal thickening toward the hinterland with comparatively little net thrust slip (Figure 1b). Thus, incorporation of Vandam Zone material into the eastern Greater Caucasus orogenic wedge may have triggered a transition from dominantly frontal to dominantly basal accretion. We, therefore, hypothesize that the capacity of a structural package to accommodate shortening via pervasive folding versus fault offset can control the gross structural evolution of an orogenic wedge. The heterogeneous deformation mechanisms, including extension, that have affected the eastern Greater Caucasus since accretion of the Vandam Zone likely result from locally focused rock uplift within the wedge that is related to basal accretion (Figure 14b; e.g., Malavieille et al., 2021).

9. Conclusions

The structural and thermochronometric data presented here provide insight into the internal architecture and deformation history of the eastern Greater Caucasus orogen. Within the thin-bedded, shale-rich strata of the range core, distributed shortening is accommodated by pervasive folding with wavelengths of 100–1,000 m. These folds range in orientation from symmetric to overturned and many are neither fault-bend nor fault-propagation folds (Figures 4c–4e). In contrast, the accreted thrust sheet of Vandam Zone strata, which includes thick-bedded volcanic and volcanoclastic strata, is deformed by slip of stratigraphically coherent packages on major thrusts (Figure 7). The contrasting styles of deformation observed within a single orogenic wedge highlight the influence of sedimentary lithology on orogen structure.

Thermochronometric data and thermal modeling reveal a complex spatio-temporal evolution of deformation within the orogen. Exhumation began within the shale-rich range core during Middle to Late Miocene time. The Zangi thrust is inferred to have served as the basal detachment of the orogen during early deformation. Accretion of the Vandam Zone thrust sheet occurred between ca. 13 and 3 Ma, based on crosscutting relationships and thermal modeling of thermochronometric ages. Following accretion of the Vandam Zone, exhumation rates within the range core increased (Figures 8b–8d) and out-of-sequence folding occurred in previously undeformed areas (Figure 10). Extensional deformation is inferred to have occurred within the Vandam Zone thrust sheet following its accretion (Figure 7). Together, the data indicate diverse modes of deformation that functioned to increase prism thickness and maintain critical taper following accretion of a thrust sheet. We infer a change in the mode of accretion, from frontal to basal, coincident with addition of the Vandam Zone strata to the orogen (Figure 14b). Our observations suggest that the lithology of accreted material may be a first-order control on the structural evolution of the eastern Greater Caucasus. The dependence of deformation style on lithologic properties such as bedding thickness, and the diverse deformation processes induced by thrust sheet accretion, are likely to be observed in other convergent margin settings characterized by heterogeneous inherited stratigraphy.

Appendix A: Block Rotation Modeling of Thermochronometric Age Transects

Because of the negative age-elevation relationships observed in vertical thermochronometric transects of the eastern Greater Caucasus (Figures 10a, 10e and 10i) and the pervasive folding observed throughout the orogen (Figures 4c–4e), we use a block rotation model to test whether tilting after cooling is likely to have affected the spatial distribution of ages (Figures 5a and 5b). A simple test case shows that tilting a rock package after cooling

ages are set can dramatically affect the age-elevation relationship of a sample set (Figures 5a and 5b). Our method uses the geometric relationships between thermochronometry samples, as well as constraints on single-sample cooling histories, to infer the orientation of a rock package when thermochronometric ages were set, increasing the amount of information available about the deformation history of a rock package (Figure 5).

In our approach, the three-dimensional sample locations of a given thermochronometric transect are treated as being attached to a rigid block, in which the distances and angles between sample locations are preserved. The orientation of this rigid block is parameterized by θ , defined as the dominant bedding plane orientation within the block, in a given cross-sectional view (Figures 5a and 5c). $\theta = 0$ corresponds to horizontal, upright bedding, and positive θ corresponds to counter-clockwise rotation, in cross-section, of the sampled block (Figures 5a and 5c). We define several variables corresponding to values of θ that can be assumed, measured, or inferred. θ_f is the value of θ upon formation of a given sedimentary rock, which we assume to be zero throughout this paper. θ_i is the modern value of θ , which can be measured in the field. θ_c is the value of θ during the time interval in which cooling ages were set, which can be inferred using the spatial interrelationships between thermochronometry samples and independent constraints on cooling/exhumation histories.

For a given set of thermochronometric ages from samples within a transect, different values of θ result in different relative spatial positions of sample locations, and thus different age-elevation relationships (Figures 5c and 5d). In our modeling method, the slopes of these age-elevation relationships and their 95% confidence intervals are calculated using a built-in MATLAB® least squares function as a function of θ . For this fitting, each AHe grain age is treated as an individual datapoint; AFT age distributions are handled by fitting 1,000 points sampled from a Gaussian distribution defined by AFT sample central ages and uncertainties (see Table 2). AHe and AFT ages are fit separately and are shown using two separate sets of symbols on resulting plots (Figures 10d, 10h and 10l). Age versus elevation is fit (Figure 5e) instead of the more commonly displayed elevation versus age because thermochronometric age scatter in some transects causes inferred age-elevation slope distributions to encompass zero slope, equivalent to an elevation-age slope of infinity, which would complicate calculations.

Each calculated slope of an age-elevation relationship is mathematically equivalent to the inverse of an exhumation rate. The apparent exhumation rates that correspond with the modeled age-elevation relationships are compared with independently inferred exhumation rates from thermal modeling results or single-sample thermochronometric age differences (Figure 5e). Sample orientations θ for which the modeled apparent exhumation rates match with the independently inferred rates are considered to be permissible syn-cooling orientations (θ_c ; Figure 5e). Comparison of these paleo-orientations with modern geometries (θ_i) provides insight into the magnitude of tilting events and the age(s) of tilting relative to cooling.

The method is a first-order attempt to understand the cause of inverted age-elevation relationships in the study area and includes several simplifying assumptions that distinguish it from a true thermo-kinematic model. The first assumption is that tilting did not overlap in time with cooling but rather occurred either completely prior to or after the cooling history that determined the measured thermochronometric ages (Figure 5a). This assumption may or may not be correct, depending on the particular structures involved in tilting, their geometry, and tectonic evolution of the rocks. The second assumption is that the closure isotherms for the thermochronometric systems are horizontal (Figure 5a). Although horizontal isotherms are unrealistic, isotherm perturbation in the eastern Greater Caucasus is likely to be minor, given the spatial scale of topography and inferred exhumation rates (Stuwe et al., 1994; see discussion in Methods). Tilting may itself affect isotherm geometry, but the small spatial scale of folding that caused tilting in the eastern Greater Caucasus is likely to mute this effect. The third assumption is that sampled transects are within rock packages that underwent rigid-block tilting with no internal deformation. Given the shale-rich lithologies of the eastern Greater Caucasus, flexural slip folding is likely, although the magnitude of such slip and its effect on relative sample positions within a transect is unknown. Despite these assumptions, our block-rotation method yields informative and geologically reasonable results (Figure 10). Thus, we infer that violations of these assumptions in the eastern Greater Caucasus are not of a sufficient degree to invalidate the method.

Data Availability Statement

Full-size versions of the geologic maps shown in Figures 6, 7, 9, 11, and 12 are available at <https://doi.org/10.6084/m9.figshare.19469873.v2> (Tye et al., 2022). Thermochronometric data are available in the Supporting Information or at <https://doi.org/10.17632/54p84dj5jj.1> (Tye & Niemi, 2022).

Acknowledgments

The authors benefited from conversations with Adam Forte, Nikolas Midttun, Chad Trexler, and Dylan Vasey that contributed to our understanding of the eastern Greater Caucasus. Boris Avdeev, Megan Hendrick, Amanda Maslyn, and Stuart Thomson contributed to sample collection, preparation, and analysis. Discussions with Kendra Murray and Stuart Thomson were helpful in interpreting our thermochronometry data. The manuscript benefitted from careful reviews by Chelsea Mackaman-Lofland and Steve Vincent. This work was supported by the University of Michigan via an International Institute Individual Fellowship, a Rackham International Research Award, and a Rackham Predoctoral Fellowship (ART) and by NSF awards EAR-1524304 (NAN) and EAR-1524631 (ESC), which included support from the Office of International Science and Engineering.

References

- Adamia, S., Zakariadze, G., Chkhotua, T., Sadradze, N., Tsereteli, N., Chabukiani, A., & Gvantsadze, A. (2011). Geology of the Caucasus: A review. *Turkish Journal of Earth Sciences*, 20(5), 489–544. <https://doi.org/10.3906/yer-1005-11>
- Agabekov, M. G., & Moshashvili, A. B. (1978). Kyurdamir-Saatly buried uplift of the Kura basin, an integral part of the Lesser Caucasus geosyncline in Cretaceous time. *Doklady of the National Academy of Sciences of the USSR*, 232, 120–122.
- Alizadeh, A. A., Guliyev, I. S., Kadirov, F. A., & Eppelbaum, L. V. (2016). *Geosciences of Azerbaijan*. Springer.
- Alizadeh, A. A., Khain, V. E., & Ismailzadeh, A. D. (2000). *Saatly superdeep. Analysis of deep structure of the Kur intermontane depression by the data of Saatly superdeep Borehole SG-1 drilling*. Nafta-Press. (in Russian).
- Allen, M. B., & Armstrong, H. A. (2008). Arabia-Eurasia collision and the forcing of mid-Cenozoic global cooling. *Paleogeography, Paleoclimatology, Paleoecology*, 265(1–2), 52–58. <https://doi.org/10.1016/j.palaeo.2008.04.021>
- Allen, M. B., Morton, A. C., Fanning, C. M., Ismail-Zadeh, A. J., & Kroonenberg, S. B. (2006). Zircon age constraints on sediment provenance in the Caspian region. *Journal of the Geological Society*, 163(4), 647–655. <https://doi.org/10.1144/0016-764920-068>
- Avdeev, B. (2011). *Tectonics of the Greater Caucasus and the Arabia-Eurasia orogen (Doctoral dissertation)*. University of Michigan.
- Avdeev, B., & Niemi, N. A. (2011). Rapid Pliocene exhumation of the central Greater Caucasus constrained by low-temperature thermochronometry. *Tectonics*, 30(2). <https://doi.org/10.1029/2010tc002808>
- Azizbekov, S. A. (1968). Tectonic structure of Azerbaijan and the Caspian depression. In *International Geophysical Congress, Tectonic Maps of Europe and the World* (p. 4). Baku: Academy of Sciences of the Azerbaijan SSR, Department of Earth Sciences.
- Bairamov, A. A., Aliyev, G. I., Hasanov, G. M., Hasanov, H. Y., Hasanov, T. A., Ismail-Zadeh, A. J., et al. (2008). *Geological Map of Azerbaijan Republic*. National Academy of Sciences of Azerbaijan Republic, Geology Institute.
- Banks, C. J., Robinson, A. G., & Williams, M. P. (1997). AAPG Memoir 68: Regional and petroleum geology of the Black Sea and surrounding region. In *Chapter 17: Structure and regional tectonics of the Achara-Trialet Fold Belt and the Adjacent Rioni and Kartli Foreland Basins*.
- Barber, D. E., Stockli, D. F., Horton, B. K., & Koshnaw, R. I. (2018). Cenozoic exhumation and foreland basin evolution of the Zagros orogen during the Arabia-Eurasia collision, western Iran. *Tectonics*, 37(12), 4396–4420. <https://doi.org/10.1029/2018tc005328>
- Bochud, M. (2011). *Tectonics of the eastern Greater Caucasus in Azerbaijan (Ph.D. dissertation)*. University of Fribourg.
- Bonnet, C., Malavieille, J., & Mosar, J. (2007). Interactions between tectonics, erosion, and sedimentation during the recent evolution of the Alpine orogen: Analog modeling insights. *Tectonics*, 26(6). <https://doi.org/10.1029/2006tc002048>
- Boyer, S. E., & Elliott, D. (1982). Thrust systems. *AAPG Bulletin*, 66(9), 1196–1230. <https://doi.org/10.1306/03B5A77D-16D1-11D7-8645000102C1865D>
- Brandon, M. T., Roden-Tice, M. K., & Garver, J. I. (1998). Late Cenozoic exhumation of the Cascadia accretionary wedge in the Olympic Mountains, northwest Washington State. *The Geological Society of America Bulletin*, 110(8), 985–1009. [https://doi.org/10.1130/0016-7606\(1998\)110<0985:lceotc>2.3.co;2](https://doi.org/10.1130/0016-7606(1998)110<0985:lceotc>2.3.co;2)
- Burkhard, M., & Sommaruga, A. (1998). *Evolution of the Swiss Molasse basin: Structural relations with the Alps and the Jura belt: London* (Vol. 134, pp. 279–298). Geological Society Special Publication.
- Burmin, V. Y., Shemeleva, I. B., Avetisyan, A. M., & Kazaryan, K. S. (2019). Deep earthquakes in the Caucasus: Recalculation results. *Seismic Instruments*, 55(6), 650–660. <https://doi.org/10.3103/s074792391906001x>
- Butler, R. W. H. (1987). Thrust sequences. *Journal of the Geological Society*, 144(4), 619–634.
- Butler, R. W. H., Bond, C. E., Cooper, M. A., & Watkins, H. (2019). *Fold-thrust structures-where have all the buckles gone?* (Vol. 487). Geological Society, London, Special Publications. SP487-7.
- Cardozo, N., & Allmendinger, R. W. (2013). Spherical projections with OSXStereonet. *Computers & Geosciences*, 51, 193–205. <https://doi.org/10.1016/j.cageo.2012.07.021>
- Casciello, E., Vergés, J., Saura, E., Casini, G., Fernández, N., Blanc, E., et al. (2009). Fold patterns and multilayer rheology of the Lurestan Province, Zagros simply folded belt (Iran). *Journal of the Geological Society*, 166(5), 947–959. <https://doi.org/10.1144/0016-76492008-138>
- Chapple, W. M. (1978). Mechanics of thin-skinned fold-and-thrust belts. *The Geological Society of America Bulletin*, 89(8), 1189–1198. [https://doi.org/10.1130/0016-7606\(1978\)89<1189:motfb>2.0.co;2](https://doi.org/10.1130/0016-7606(1978)89<1189:motfb>2.0.co;2)
- Cowgill, E., Forte, A. M., Niemi, N., Avdeev, B., Tye, A., Trexler, C., et al. (2016). Relict basin closure and crustal shortening budgets during continental collision: An example from Caucasus sediment provenance. *Tectonics*, 35(12), 2918–2947. <https://doi.org/10.1002/2016tc004295>
- Cumberpatch, Z. A., Soutter, E. L., Kane, I. A., Casson, M., & Vincent, S. J. (2021). Evolution of a mixed siliciclastic-carbonate deep-marine system on an unstable margin: The Cretaceous of the Eastern Greater Caucasus, Azerbaijan. *Basin Research*, 33(1), 612–647. <https://doi.org/10.1111/bre.12488>
- Currie, J. B., Patnode, H. W., & Trump, R. P. (1962). Development of folds in sedimentary strata. *The Geological Society of America Bulletin*, 73(6), 655–673. [https://doi.org/10.1130/0016-7606\(1962\)73\[655:dofiss\]2.0.co;2](https://doi.org/10.1130/0016-7606(1962)73[655:dofiss]2.0.co;2)
- Dahlen, F. A. (1990). Critical taper model of fold-and-thrust belts and accretionary wedges. *Annual Review of Earth and Planetary Sciences*, 18(1), 55–99. <https://doi.org/10.1146/annurev.ea.18.050190.000415>
- Dahlen, F. A., Suppe, J., & Davis, D. (1984). Mechanics of fold-and-thrust belts and accretionary wedges: Cohesive Coulomb theory. *Journal of Geophysical Research: Solid Earth*, 89(B12), 10087–10101. <https://doi.org/10.1029/jb089ib12p10087>
- Dahlstrom, C. D. (1970). Structural geology in the eastern margin of the Canadian Rocky Mountains. *Bulletin of Canadian Petroleum Geology*, 18(3), 332–406.
- Dahlstrom, C. D. A. (1969). Balanced cross-sections. *Canadian Journal of Earth Sciences*, 6(4), 743–757. <https://doi.org/10.1139/e69-069>
- Davis, D., Suppe, J., & Dahlen, F. A. (1983). Mechanics of fold-and-thrust belts and accretionary wedges. *Journal of Geophysical Research: Solid Earth*, 88(B2), 1153–1172. <https://doi.org/10.1029/jb088ib02p01153>
- DeCelles, P. G., & Mitra, G. (1995). History of the Sevier orogenic wedge in terms of critical taper models, northeast Utah and southwest Wyoming. *The Geological Society of America Bulletin*, 107(4), 454–462. [https://doi.org/10.1130/0016-7606\(1995\)107<0454:hotsow>2.3.co;2](https://doi.org/10.1130/0016-7606(1995)107<0454:hotsow>2.3.co;2)
- Ditullio, L., & Byrne, T. (1990). Deformation paths in the shallow levels of an accretionary prism: The Eocene Shimanto belt of southwest Japan. *The Geological Society of America Bulletin*, 102(10), 1420–1438. [https://doi.org/10.1130/0016-7606\(1990\)102<1420:dptisl>2.3.co;2](https://doi.org/10.1130/0016-7606(1990)102<1420:dptisl>2.3.co;2)
- Donelick, R. A., O'Sullivan, P. B., & Ketcham, R. A. (2005). Apatite fission track analysis. *Reviews in Mineralogy and Geochemistry*, 58(1), 49–94. <https://doi.org/10.2138/rmg.2005.58.3>
- Ehlers, T. A., & Farley, K. A. (2003). Apatite (U-Th)/He thermochronometry: Methods and applications to problems in tectonic and surface processes. *Earth and Planetary Science Letters*, 206(1–2), 1–14. [https://doi.org/10.1016/s0012-821x\(02\)01069-5](https://doi.org/10.1016/s0012-821x(02)01069-5)
- Emerman, S. H., & Turcotte, D. L. (1983). A fluid model for the shape of accretionary wedges. *Earth and Planetary Science Letters*, 63(3), 379–384. [https://doi.org/10.1016/0012-821x\(83\)90111-5](https://doi.org/10.1016/0012-821x(83)90111-5)
- Erslev, E. A. (1991). Trishear fault-propagation folding. *Geology*, 19(6), 617–620. [https://doi.org/10.1130/0091-7613\(1991\)019<0617:tfpf>2.3.co;2](https://doi.org/10.1130/0091-7613(1991)019<0617:tfpf>2.3.co;2)

- Espina, R. G., Alonso, J. L., & Pulgar, J. A. (1996). Growth and propagation of buckle folds determined from syntectonic sediments (the Ubierna Fold Belt, Cantabrian Mountains, N Spain). *Journal of Structural Geology*, 18(4), 431–441. [https://doi.org/10.1016/0191-8141\(95\)00103-k](https://doi.org/10.1016/0191-8141(95)00103-k)
- Farley, K. A. (2002). (U-Th)/He dating: Techniques, calibrations, and applications. *Reviews in Mineralogy and Geochemistry*, 47(1), 819–844. <https://doi.org/10.2138/rmg.2002.47.18>
- Farley, K. A., Rusmore, M. E., & Bogue, S. W. (2001). Post-10 Ma uplift and exhumation of the northern Coast Mountains, British Columbia. *Geology*, 29(2), 99–102. [https://doi.org/10.1130/0091-7613\(2001\)029<0099:pmuao>2.0.co;2](https://doi.org/10.1130/0091-7613(2001)029<0099:pmuao>2.0.co;2)
- Fitz-Díaz, E., Tolson, G., Hudleston, P., Bolaños-Rodríguez, D., Ortega-Flores, B., & Serrano, A. V. (2012). The role of folding in the development of the Mexican fold-and-thrust belt. *Geosphere*, 8(4), 931–949.
- Flowers, R. M., & Kelley, S. A. (2011). Interpreting data dispersion and “inverted” dates in apatite (U-Th)/He and fission track data sets: An example from the US midcontinent. *Geochimica et Cosmochimica Acta*, 75(18), 5169–5186. <https://doi.org/10.1016/j.gca.2011.06.016>
- Flowers, R. M., Ketcham, R. A., Enkelmann, E., Gautheron, C., Reiners, P. W., Metcalf, J. R., et al. (2022). (U-Th)/He chronology: Part 2. Considerations for evaluating, integrating, and interpreting conventional individual aliquot data. *GSA Bulletin*. <https://doi.org/10.1130/B36268.1>
- Flowers, R. M., Ketcham, R. A., Shuster, D. L., & Farley, K. A. (2009). Apatite (U-Th)/He thermochronometry using a radiation damage accumulation and annealing model. *Geochimica et Cosmochimica Acta*, 73(8), 2347–2365. <https://doi.org/10.1016/j.gca.2009.01.015>
- Forté, A. M., Cowgill, E., Bernardin, T., Kreylos, O., & Hamann, B. (2010). Late Cenozoic deformation of the Kura fold-thrust belt, southern Greater Caucasus. *Bulletin*, 122(3–4), 465–486. <https://doi.org/10.1130/b26464.1>
- Forté, A. M., Cowgill, E., Murtuzayev, I., Kangarli, T., & Stoica, M. (2013). Structural geometries and magnitude of shortening in the eastern Kura fold-thrust belt, Azerbaijan: Implications for the development of the Greater Caucasus mountains. *Tectonics*, 32(3), 688–717. <https://doi.org/10.1002/tect.20032>
- Forté, A. M., Cowgill, E., & Whipple, K. X. (2014). Transition from a singly vergent to doubly vergent wedge in a young orogen: The Greater Caucasus. *Tectonics*, 33(11), 2077–2101. <https://doi.org/10.1002/2014tc003651>
- Forté, A. M., Gutterman, K. R., Van Soest, M. C., & Gallagher, K. (2022). Building a Young Mountain Range: Insight into the growth of the Greater Caucasus mountains from detrital zircon (U-Th)/He thermochronology and ¹⁰Be erosion rates. *Tectonics*, 41(5), e2021TC006900. <https://doi.org/10.1029/2021tc006900>
- Forté, A. M., Whipple, K. X., & Cowgill, E. (2015). Drainage network reveals patterns and history of active deformation in the eastern Greater Caucasus. *Geosphere*, 11(5), 1343–1364. <https://doi.org/10.1130/ges01121.1>
- François, T., Burov, E., Agard, P., & Meyer, B. (2014). Buildup of a dynamically supported orogenic plateau: Numerical modeling of the Zagros/Central Iran case study. *Geochemistry, Geophysics, Geosystems*, 15(6), 2632–2654. <https://doi.org/10.1002/2013GC005223>
- Galbraith, R. F. (1988). Graphical display of estimates having differing standard errors. *Technometrics*, 30(3), 271–281.
- Galbraith, R. F. (2005). *Statistics for fission track analysis*. Chapman and Hall/CRC.
- Galbraith, R. F., & Green, P. F. (1990). Estimating the component ages in a finite mixture. *International Journal of Radiation Applications and Instrumentation—Part D: Nuclear Tracks and Radiation Measurements*, 17(3), 197–206. [https://doi.org/10.1016/1359-0189\(90\)90035-v](https://doi.org/10.1016/1359-0189(90)90035-v)
- Gallagher, K. (2012). Transdimensional inverse thermal history modeling for quantitative thermochronology. *Journal of Geophysical Research: Solid Earth*, 117(B2). <https://doi.org/10.1029/2011j008825>
- Gavrilov, Y. O. (2018). Architecture of the Southern Marginal Zone of the Upper Jurassic-Valanginian carbonate platform of the northeastern Caucasus (Dagestan, Shakhdag Massif). *Lithology and Mineral Resources*, 53(6), 460–472. <https://doi.org/10.1134/s0024490218060032>
- Ghisetti, F. C., Barnes, P. M., Ellis, S., Plaza-Faverola, A. A., & Barker, D. H. (2016). The last 2 Myr of accretionary wedge construction in the central Hikurangi margin (North Island, New Zealand): Insights from structural modeling. *Geochemistry, Geophysics, Geosystems*, 17(7), 2661–2686. <https://doi.org/10.1002/2016gc006341>
- Gleadow, A. J., Duddy, I. R., Green, P. F., & Hegarty, K. A. (1986). Fission track lengths in the apatite annealing zone and the interpretation of mixed ages. *Earth and Planetary Science Letters*, 78(2–3), 245–254. [https://doi.org/10.1016/0012-821x\(86\)90065-8](https://doi.org/10.1016/0012-821x(86)90065-8)
- Golubjatnikov, V. D., & Dubogryzova, A. G. (1959). *Geological map of the USSR, Caucasus series sheet K-39-XIX, scale 1:200,000*. Ministry of Geology and Mineral Protection USSR.
- Gradstein, F. M., Ogg, J. G., Schmitz, M. D., & Ogg, G. M. (Eds.) (2012). *A geologic time scale 2012* (p. 1144). Elsevier.
- Grando, G., & McClay, K. (2007). Morphotectonics domains and structural styles in the Makran accretionary prism, offshore Iran. *Sedimentary Geology*, 196(1–4), 157–179. <https://doi.org/10.1016/j.sedgeo.2006.05.030>
- Graveleau, F., Malavieille, J., & Dominguez, S. (2012). Experimental modeling of orogenic wedges: A review. *Tectonophysics*, 538, 1–66. <https://doi.org/10.1016/j.tecto.2012.01.027>
- Green, P. F., Duddy, I. R., Gleadow, A. J. W., Tingate, P. R., & Laslett, G. M. (1986). Thermal annealing of fission tracks in apatite: I. A qualitative description. *Chemical Geology: Isotope Geoscience section*, 59, 237–253. [https://doi.org/10.1016/0168-9622\(86\)90074-6](https://doi.org/10.1016/0168-9622(86)90074-6)
- Green, T., Abdullayev, N., Hossack, J., Riley, G., & Roberts, A. M. (2009). Sedimentation and subsidence in the South Caspian Basin, Azerbaijan. *Geological Society, London, Special Publications*, 312(1), 241–260. <https://doi.org/10.1144/sp312.12>
- Guenther, W. R., Reiners, P. W., Ketcham, R. A., Nasdala, L., & Giester, G. (2013). Helium diffusion in natural zircon: Radiation damage, anisotropy, and the interpretation of zircon (U-Th)/He thermochronology. *American Journal of Science*, 313(3), 145–198. <https://doi.org/10.2475/03.2013.01>
- Guest, B., Axen, G. J., Lam, P. S., & Hassanzadeh, J. (2006). Late Cenozoic shortening in the west-central Alborz Mountains, northern Iran, by combined conjugate strike-slip and thin-skinned deformation. *Geosphere*, 2(1), 35–52. <https://doi.org/10.1130/ges00019.1>
- Guest, B., Horton, B. K., Axen, G. J., Hassanzadeh, J., & McIntosh, W. C. (2007). Middle to late Cenozoic basin evolution in the western Alborz Mountains: Implications for the onset of collisional deformation in northern Iran. *Tectonics*, 26(6). <https://doi.org/10.1029/2006tc002091>
- Gulick, S. P., Meltzer, A. M., & Clarke, S. H., Jr. (1998). Seismic structure of the southern Cascadia subduction zone and accretionary prism north of the Mendocino triple junction. *Journal of Geophysical Research: Solid Earth*, 103(B11), 27207–27222. <https://doi.org/10.1029/98jb02526>
- Gunnels, M., Yetirmishli, G., Kazimova, S., & Sandvol, E. (2021). Seismotectonic evidence for subduction beneath the eastern Greater Caucasus. *Geophysical Journal International*, 224(3), 1825–1834.
- Gusmeo, T., Cavazza, W., Alania, V. M., Enukidze, O. V., Zattin, M., & Corrado, S. (2021). Structural inversion of back-arc basins—The Neogene Adjara-Trialeti fold-and-thrust belt (SW Georgia) as a far-field effect of the Arabia-Eurasia collision. *Tectonophysics*, 803, 228702. <https://doi.org/10.1016/j.tecto.2020.228702>
- Gutscher, M. A., Kukowski, N., Malavieille, J., & Lallemand, S. (1998). Episodic imbricate thrusting and underthrusting: Analog experiments and mechanical analysis applied to the Alaskan accretionary wedge. *Journal of Geophysical Research: Solid Earth*, 103(B5), 10161–10176. <https://doi.org/10.1029/97jb03541>
- Hatzfeld, D., & Molnar, P. (2010). Comparisons of the kinematics and deep structures of the Zagros and Himalaya and of the Iranian and Tibetan plateaus and geodynamic implications. *Reviews of Geophysics*, 48(2). <https://doi.org/10.1029/2009rg000304>

- Hollingsworth, J., Jackson, J., Walker, R., & Nazari, H. (2008). Extrusion tectonics and subduction in the eastern South Caspian region since 10 Ma. *Geology*, *36*(10), 763–766. <https://doi.org/10.1130/g25008a.1>
- Hosseini-Barzi, M., & Talbot, C. J. (2003). A tectonic pulse in the Makran accretionary prism recorded in Iranian coastal sediments. *Journal of the Geological Society*, *160*(6), 903–910. <https://doi.org/10.1144/0016-764903-005>
- House, M. A., Wernicke, B. P., & Farley, K. A. (1998). Dating topography of the Sierra Nevada, California, using apatite (U-Th)/He ages. *Nature*, *396*(6706), 66–69. <https://doi.org/10.1038/23926>
- Hubbard, J., Barbot, S., Hill, E. M., & Tapponnier, P. (2015). Coseismic slip on shallow décollement megathrusts: Implications for seismic and tsunami hazard. *Earth-Science Reviews*, *141*, 45–55. <https://doi.org/10.1016/j.earscirev.2014.11.003>
- Huntington, K. W., Ehlers, T. A., Hodges, K. V., & Whipp, D. M., Jr. (2007). Topography, exhumation pathway, age uncertainties, and the interpretation of thermochronometer data. *Tectonics*, *26*(4). <https://doi.org/10.1029/2007tc002108>
- Kadirov, F. A., Floyd, M., Alizadeh, A., Guliev, I., Reilinger, R., Kuleli, S., et al. (2012). Kinematics of the eastern Caucasus near Baku, Azerbaijan. *Natural Hazards*, *63*(2), 997–1006. <https://doi.org/10.1007/s11069-012-0199-0>
- Kadirov, F. A., Floyd, M., Reilinger, R., Alizadeh, A. A., Guliyev, I. S., Mammadov, S. G., & Safarov, R. T. (2015). Active geodynamics of the Caucasus region: Implications for earthquake hazards in Azerbaijan. *Proceedings of Azerbaijan National Academy of Sciences, the Sciences of Earth*, *3*, 3–17.
- Kamb, W. B. (1959). Ice petrofabric observations from Blue Glacier, Washington in relation to theory and experiment. *Journal of Geophysical Research*, *64*, 1891–1909. <https://doi.org/10.1029/jz064i011p01891>
- Ketcham, R. A., Carter, A., Donelick, R. A., Barbarand, J., & Hurford, A. J. (2007). Improved modeling of fission-track annealing in apatite. *American Mineralogist*, *92*(5–6), 799–810. <https://doi.org/10.2138/am.2007.2281>
- Ketcham, R. A., Gautheron, C., & Tassan-Got, L. (2011). Accounting for long alpha-particle stopping distances in (U–Th–Sm)/He geochronology: Refinement of the baseline case. *Geochimica et Cosmochimica Acta*, *75*(24), 7779–7791. <https://doi.org/10.1016/j.gca.2011.10.011>
- Khain, V. E. (1975). Structure and main stages in the tectono-magmatic development of the Caucasus: An attempt at geodynamic interpretation. *American Journal of Science*, *275*, 131–156.
- Khain, V. E. (2007). Mesozoic-Cenozoic accretionary complexes of the Greater Caucasus. In *Doklady Earth Sciences* (Vol. 413, No. 2, pp. 376–379). MAIK Nauka/Interperiodica.
- Khain, V. E., & Shardanov, A. (1960). *Geological map of the USSR, Caucasus series sheet K-39-XXV, scale 1:200,000*. Ministry of Geology and Mineral Protection USSR.
- Kopp, M. L. (1985). Age and nature of deformations of sediments comprising the Lagich Syncline. *Moscow University Geology Bulletin*, *40*(1), 23–32.
- Kopp, M. L., & Shcherba, I. G. (1985). Late Alpine development of the east Caucasus. *Geotectonics*, *19*(6), 497–507.
- Lavé, J., & Avouac, J. P. (2000). Active folding of fluvial terraces across the Siwaliks Hills, Himalayas of central Nepal. *Journal of Geophysical Research: Solid Earth*, *105*(B3), 5735–5770.
- Madanipour, S., Ehlers, T. A., Yassaghi, A., & Enkelmann, E. (2017). Accelerated middle Miocene exhumation of the Talesh Mountains constrained by U-Th/He thermochronometry: Evidence for the Arabia-Eurasia collision in the NW Iranian Plateau. *Tectonics*, *36*(8), 1538–1561. <https://doi.org/10.1002/2016tc004291>
- Malavieille, J. (2010). Impact of erosion, sedimentation, and structural heritage on the structure and kinematics of orogenic wedges: Analog models and case studies. *Geological Society of America Today*, *20*(1), 4–10. <https://doi.org/10.1130/gsatg48a.1>
- Malavieille, J., Dominguez, S., Lu, C. Y., Chen, C. T., & Konstantinovskaya, E. (2021). Deformation partitioning in mountain belts: Insights from analog modeling experiments and the Taiwan collisional orogen. *Geological Magazine*, *158*(1), 84–103. <https://doi.org/10.1017/s0016756819000645>
- McQuarrie, N. (2004). Crustal scale geometry of the Zagros fold-thrust belt, Iran. *Journal of Structural Geology*, *26*(3), 519–535. <https://doi.org/10.1016/j.jsg.2003.08.009>
- McQuarrie, N., & van Hinsbergen, D. J. (2013). Retrodeforming the Arabia-Eurasia collision zone: Age of collision versus magnitude of continental subduction. *Geology*, *41*(3), 315–318. <https://doi.org/10.1130/g33591.1>
- Mellors, R. J., Jackson, J., Myers, S., Gok, R., Priestley, K., Yetirmishli, G., et al. (2012). Deep earthquakes beneath the northern Caucasus: Evidence of active or recent subduction in western Asia. *Bulletin of the Seismological Society of America*, *102*(2), 862–866. <https://doi.org/10.1785/0120110184>
- Moore, G. F., Park, J. O., Bangs, N. L., Gulick, S. P., Tobin, H. J., Nakamura, Y., et al. (2009). Structural and seismic stratigraphic framework of the NanTroSEIZE Stage 1 transect. NanTroSEIZE Stage 1: Investigations of seismogenesis, Nankai Trough, Japan. *Proceedings of the Integrated Ocean Drilling Program*. <https://doi.org/10.2204/iodp.proc.314315316.102.2009>
- Moore, J. C., & Vrolijk, P. (1992). Fluids in accretionary prisms. *Reviews of Geophysics*, *30*(2), 113–135. <https://doi.org/10.1029/92rg00201>
- Morley, C. K. (1988). Out-of-sequence thrusts. *Tectonics*, *7*(3), 539–561. <https://doi.org/10.1029/tc007i003p00539>
- Morley, C. K., Kongwung, B., Julapour, A. A., Abdolghafourian, M., Hajian, M., Waples, D., et al. (2009). Structural development of a major late Cenozoic basin and transpressional belt in central Iran: The Central Basin in the Qom-Saveh area. *Geosphere*, *5*(4), 325–362. <https://doi.org/10.1130/ges00223.1>
- Mosar, J., Kangarli, T., Bochud, M., Glasmacher, U. A., Rast, A., Brunet, M. F., & Sosson, M. (2010). Cenozoic-recent tectonics and uplift in the Greater Caucasus: A perspective from Azerbaijan. *Geological Society, London, Special Publications*, *340*(1), 261–280. <https://doi.org/10.1144/sp340.12>
- Mosar, J., Mauvilly, J., Koiava, K., Gamkrelidze, I., Enna, N., Lavrishev, V., & Kalberguenova, V. (2022). Tectonics in the Greater Caucasus (Georgia-Russia): From an intracontinental rifted basin to a doubly verging fold-and-thrust belt. *Marine and Petroleum Geology*, *140*, 105630. <https://doi.org/10.1016/j.marpetgeo.2022.105630>
- Moutherau, F. (2011). Timing of uplift in the Zagros belt/Iranian plateau and accommodation of late Cenozoic Arabia-Eurasia convergence. *Geological Magazine*, *148*(5–6), 726–738. <https://doi.org/10.1017/s0016756811000306>
- Mulugeta, G., & Koyi, H. (1992). Episodic accretion and strain partitioning in a model sand wedge. *Tectonophysics*, *202*(2–4), 319–333. [https://doi.org/10.1016/0040-1951\(92\)90117-o](https://doi.org/10.1016/0040-1951(92)90117-o)
- Mumladze, T., Forte, A. M., Cowgill, E. S., Trexler, C. C., Niemi, N. A., Yıkmaz, M. B., & Kellogg, L. H. (2015). Subducted, detached, and torn slabs beneath the Greater Caucasus. *GeoResJ*, *5*, 36–46. <https://doi.org/10.1016/j.grj.2014.09.004>
- Nalivkin, D. V. (1976). *Geologic map of the Caucasus*. Ministry of Geology.
- Niemi, N. A., & Clark, M. K. (2018). Long-term exhumation rates exceed paleoseismic slip rates in the central Santa Monica Mountains, Los Angeles County, California. *Geology*, *46*(1), 63–66. <https://doi.org/10.1130/g39388.1>
- Nikishin, A. M., Cloetingh, S. A. P. L., Brunet, M. F., Stephenson, R. A., Bolotov, S. N., & Ershov, A. V. (1998). Scythian platform, Caucasus and Black Sea region: Mesozoic-Cenozoic tectonic history and dynamics. *Peri-Tethys Memoir*, *3*, 163–176.

- Nikishin, A. M., Ziegler, P., Panov, D. I., Nazarevich, B. P., Brunet, M.-F., Stephenson, R. A., et al. (2001). Mesozoic and Cenozoic evolution of the Scythian Platform—Black Sea—Caucasus domain. In P. Ziegler, W. Cavazza, A. H. F. Robertson, & S. Crasquin-Soleau (Eds.), *Peri-Tethys Memoir 6—Peri-Tethyan rift/wrench basins and passive margins. Mémoires du Muséum national d'Histoire naturelle, Paris* (Vol. 186, pp. 295–346).
- Philip, H., Cisternas, A., Gvishiani, A., & Gorshkov, A. (1989). The Caucasus: An actual example of the initial stages of continental collision. *Tectonophysics*, *161*(1–2), 1–21. [https://doi.org/10.1016/0040-1951\(89\)90297-7](https://doi.org/10.1016/0040-1951(89)90297-7)
- Platt, J. P. (1986). Dynamics of orogenic wedges and the uplift of high-pressure metamorphic rocks. *The Geological Society of America Bulletin*, *97*(9), 1037–1053. [https://doi.org/10.1130/0016-7606\(1986\)97<1037:doowat>2.0.co;2](https://doi.org/10.1130/0016-7606(1986)97<1037:doowat>2.0.co;2)
- Platt, J. P., Leggett, J. K., Young, J., Raza, H., & Alam, S. (1985). Large-scale sediment underplating in the Makran accretionary prism, southwest Pakistan. *Geology*, *13*(7), 507–511. [https://doi.org/10.1130/0091-7613\(1985\)13<507:lsuim>2.0.co;2](https://doi.org/10.1130/0091-7613(1985)13<507:lsuim>2.0.co;2)
- Ramsay, J. G., & Wood, D. S. (1973). The geometric effects of volume change during deformation processes. *Tectonophysics*, *16*(3–4), 263–277. [https://doi.org/10.1016/0040-1951\(73\)90015-2](https://doi.org/10.1016/0040-1951(73)90015-2)
- Reilinger, R., McClusky, S., Vernant, P., Lawrence, S., Ergintav, S., Cakmak, R., et al. (2006). GPS constraints on continental deformation in the Africa-Arabia-Eurasia continental collision zone and implications for the dynamics of plate interactions. *Journal of Geophysical Research: Solid Earth*, *111*(B5). <https://doi.org/10.1029/2005jb004051>
- Reiners, P. W. (2005). Zircon (U-Th)/He thermochronometry. *Reviews in Mineralogy and Geochemistry*, *58*(1), 151–179. <https://doi.org/10.2138/rmg.2005.58.6>
- Reiners, P. W. (2007). Thermochronologic approaches to paleotopography. *Reviews in Mineralogy and Geochemistry*, *66*(1), 243–267. <https://doi.org/10.2138/rmg.2007.66.10>
- Reiners, P. W., & Brandon, M. T. (2006). Using thermochronology to understand orogenic erosion. *Annual Review of Earth and Planetary Sciences*, *34*(1), 419–466. <https://doi.org/10.1146/annurev.earth.34.031405.125202>
- Reiners, P. W., & Nicolescu, S. (2006). Measurement of parent nuclides for (U-Th)/He chronometry by solution sector ICP-MS, ARHDL Report 1. Retrieved from <http://www.geo.arizona.edu/~reiners/arhdl/arhdl.htm>
- Reiners, P. W., Spell, T. L., Nicolescu, S., & Zanetti, K. A. (2004). Zircon (U-Th)/He thermochronometry: He diffusion and comparisons with ⁴⁰Ar/³⁹Ar dating. *Geochimica et Cosmochimica Acta*, *68*(8), 1857–1887. <https://doi.org/10.1016/j.gca.2003.10.021>
- Rolland, Y., Sosson, M., Adamia, S., & Sadradze, N. (2011). Prolonged Variscan to Alpine history of an active Eurasian margin (Georgia, Armenia) revealed by ⁴⁰Ar/³⁹Ar dating. *Gondwana Research*, *20*, 798–815. <https://doi.org/10.1016/j.gr.2011.05.007>
- Saintot, A., Brunet, M. F., Yakovlev, F., Sébrier, M., Stephenson, R., Ershov, A., et al. (2006). The Mesozoic-Cenozoic tectonic evolution of the Greater Caucasus. *Geological Society, London, Memoirs*, *32*(1), 277–289. <https://doi.org/10.1144/gsl.mem.2006.032.01.16>
- Saintot, A., Stephenson, R. A., Stovba, S., Brunet, M. F., Yegorova, T., & Starostenko, V. (2006). The evolution of the southern margin of Eastern Europe (Eastern European and Scythian platforms) from the latest Precambrian-Early Paleozoic to the Early Cretaceous. *Geological Society, London, Memoirs*, *32*(1), 481–505. <https://doi.org/10.1144/gsl.mem.2006.032.01.30>
- Sample, J. C., & Fisher, D. M. (1986). Duplex accretion and underplating in an ancient accretionary complex, Kodiak Islands, Alaska. *Geology*, *14*(2), 160–163. [https://doi.org/10.1130/0091-7613\(1986\)14<160:daauia>2.0.co;2](https://doi.org/10.1130/0091-7613(1986)14<160:daauia>2.0.co;2)
- Şengör, A. C. (1984). The Cimmeride orogenic system and the tectonics of Eurasia.
- Singh, S. C., Carton, H., Tapponnier, P., Hananto, N. D., Chauhan, A. P., Hartoyo, D., et al. (2008). Seismic evidence for broken oceanic crust in the 2004 Sumatra earthquake epicentral region. *Nature Geoscience*, *1*(11), 777–781. <https://doi.org/10.1038/ngeo336>
- Singh, S. C., Hananto, N., Mukti, M., Permana, H., Djajadhardja, Y., & Harjono, H. (2011). Seismic images of the megathrust rupture during the 25 October 2010 Pagai earthquake, SW Sumatra: Frontal rupture and large tsunami. *Geophysical Research Letters*, *38*(16). <https://doi.org/10.1029/2011gl048935>
- Skobeltsyn, G., Mellors, R., Gök, R., Türkelli, N., Yetirmishli, G., & Sandvol, E. (2014). Upper mantle S wave velocity structure of the East Anatolian-Caucasus region. *Tectonics*, *33*(3), 207–221. <https://doi.org/10.1002/2013tc003334>
- Sobornov, K. O. (1994). Structure and petroleum potential of the Dagestan thrust belt, northeastern Caucasus, Russia. *Bulletin of Canadian Petroleum Geology*, *42*(3), 352–364.
- Sobornov, K. O. (2021). Structure and evolution of the Terek-Caspian fold-and-thrust belt: New insights from regional seismic data. *Journal of Petroleum Geology*, *44*(3), 259–286. <https://doi.org/10.1111/jpg.12793>
- Sokhadze, G., Floyd, M., Godoladze, T., King, R., Cowgill, E. S., Javakishvili, Z., et al. (2018). Active convergence between the lesser and Greater Caucasus in Georgia: Constraints on the tectonic evolution of the Lesser-Greater Caucasus continental collision. *Earth and Planetary Science Letters*, *481*, 154–161. <https://doi.org/10.1016/j.epsl.2017.10.007>
- Sorby, H. C. (1908). On the application of quantitative methods to the study of the structure and history of rocks. *Quarterly Journal of the Geological Society*, *64*(1–4), 171–233. <https://doi.org/10.1144/gsl.jgs.1908.064.01-04.12>
- Sosson, M., Rolland, Y., Müller, C., Danelian, T., Melkonyan, R., Kekelia, S., et al. (2010). Subductions, obduction, and collision in the Lesser Caucasus (Armenia, Azerbaijan, Georgia), new insights. *Geological Society, London, Special Publications*, *340*, 329–352. <https://doi.org/10.1144/sp340.14>
- Stampfli, G. M. (2013). Response to the comments on “The formation of Pangea” by DA Ruban. *Tectonophysics*, *608*, 1445–1447. <https://doi.org/10.1016/j.tecto.2013.09.004>
- Stüwe, K., White, L., & Brown, R. (1994). The influence of eroding topography on steady-state isotherms. Application to fission track analysis. *Earth and Planetary Science Letters*, *124*(1–4), 63–74.
- Suppe, J. (1981). Mechanics of mountain building and metamorphism in Taiwan. *Memoir of the Geological Society of China*, *4*(6), 67–89.
- Suppe, J., & Medwedeff, D. A. (1990). Geometry and Kinematics of fault-propagation folding. *Eclogae Geologicae Helveticae*, *87*, 33–46.
- Thomson, S. N., Reiners, P. W., Hemming, S. R., & Gehrels, G. E. (2013). The contribution of glacial erosion to shaping the hidden landscape of East Antarctica. *Nature Geoscience*, *6*(3), 203–207. <https://doi.org/10.1038/ngeo1722>
- Tibaldi, A., Tsereteli, N., Varazanashvili, O., Babayev, G., Barth, A., Mumladze, T., et al. (2020). Active stress field and fault kinematics of the Greater Caucasus. *Journal of Asian Earth Sciences*, *188*, 104108. <https://doi.org/10.1016/j.jseaes.2019.104108>
- Trexler, C. C. (2018). *Structural investigations of the tectonic history of the western Greater Caucasus mountains, Republic of Georgia (Ph.D. dissertation)*. University of California.
- Trexler, C. C., Cowgill, E., Niemi, N. A., Vasey, D. A., & Godoladze, T. (2022). Tectonostratigraphy and major structures of the Georgian Greater Caucasus: Implications for structural architecture, along-strike continuity, and orogen evolution. *Geosphere*, *18*(1), 211–240. <https://doi.org/10.1130/ges02385.1>
- Tye, A. R., & Niemi, N. (2022). Eastern Greater Caucasus thermochronometry. Mendeley Data. <https://doi.org/10.17632/54p84dj5jj.1>
- Tye, A. R., Niemi, N., Cowgill, E., Kadirov, F., & Babayev, G. (2022). Geological swath maps of the eastern Greater Caucasus, Azerbaijan, with GIS data. *Figshare*. <https://doi.org/10.6084/m9.figshare.19469873.v2>

- Tye, A. R., Niemi, N. A., Safarov, R. T., Kadirov, F. A., & Babayev, G. R. (2021). Sedimentary response to a collision orogeny recorded in detrital zircon provenance of Greater Caucasus foreland basin sediments. *Basin Research*, 33(2), 933–967. <https://doi.org/10.1111/bre.12499>
- Uba, C. E., Kley, J., Strecker, M. R., & Schmitt, A. K. (2009). Unsteady evolution of the Bolivian Subandean thrust belt: The role of enhanced erosion and clastic wedge progradation. *Earth and Planetary Science Letters*, 281(3–4), 134–146. <https://doi.org/10.1016/j.epsl.2009.02.010>
- Van der Boon, A., van Hinsbergen, D. J. J., Rezaeian, M., Gürer, D., Honarmand, M., Pastor-Galán, D., et al. (2018). Quantifying Arabia-Eurasia convergence accommodated in the Greater Caucasus by paleomagnetic reconstruction. *Earth and Planetary Science Letters*, 482, 454–469. <https://doi.org/10.1016/j.epsl.2017.11.025>
- Van Hinsbergen, D. J., Torsvik, T. H., Schmid, S. M., Mañenco, L. C., Maffione, M., Vissers, R. L., et al. (2020). Orogenic architecture of the Mediterranean region and kinematic reconstruction of its tectonic evolution since the Triassic. *Gondwana Research*, 81, 79–229. <https://doi.org/10.1016/j.gr.2019.07.009>
- Vasey, D. A., Cowgill, E., & Cooper, K. M. (2021). A preliminary framework for magmatism in modern continental back-arc basins and its application to the Triassic-Jurassic tectonic evolution of the Caucasus. *Geochemistry, Geophysics, Geosystems*, 22(6), e2020GC009490. <https://doi.org/10.1029/2020gg009490>
- Vasey, D. A., Cowgill, E., Roeske, S. M., Niemi, N. A., Godoladze, T., Skhirtladze, I., & Gogoladze, S. (2020). Evolution of the Greater Caucasus basement and formation of the Main Caucasus Thrust, Georgia. *Tectonics*, 39(3), e2019TC005828. <https://doi.org/10.1029/2019tc005828>
- Vermeesch, P. (2009). RadialPlotter: A Java application for fission track, luminescence and other radial plots. *Radiation Measurements*, 44(4), 409–410. <https://doi.org/10.1016/j.radmeas.2009.05.003>
- Vincent, S. J., Braham, W., Lavrishchev, V. A., Maynard, J. R., & Harland, M. (2016). The formation and inversion of the western Greater Caucasus Basin and the uplift of the western Greater Caucasus: Implications for the wider Black Sea region. *Tectonics*, 35(12), 2948–2962. <https://doi.org/10.1002/2016tc004204>
- Vincent, S. J., Morton, A. C., Carter, A., Gibbs, S., & Barabazde, T. G. (2007). Oligocene uplift of the western Greater Caucasus: An effect of initial Arabia-Eurasia collision. *Terra Nova*, 19(2), 160–166. <https://doi.org/10.1111/j.1365-3121.2007.00731.x>
- Vincent, S. J., Somin, M. L., Carter, A., Vezzoli, G., Fox, M., & Vautravers, B. (2020). Testing models of Cenozoic exhumation in the western Greater Caucasus. *Tectonics*, 39(2), e2018TC005451. <https://doi.org/10.1029/2018tc005451>
- Voronin, M. P., Gavrilov, M. D., & Khain, V. E. (1959). *Geological map of the USSR, Caucasus series sheet K-39-XXXI, scale 1:200,000*. Ministry of Geology and Mineral Protection USSR.
- Westbrook, G. K., & Smith, M. J. (1983). Long decollements and mud volcanoes: Evidence from the Barbados Ridge Complex for the role of high pore-fluid pressure in the development of an accretionary complex. *Geology*, 11(5), 279–283. [https://doi.org/10.1130/0091-7613\(1983\)11<279:ldamve>2.0.co;2](https://doi.org/10.1130/0091-7613(1983)11<279:ldamve>2.0.co;2)
- Willett, S. D. (1999). Orogeny and orography: The effects of erosion on the structure of mountain belts. *Journal of Geophysical Research: Solid Earth*, 104(B12), 28957–28981. <https://doi.org/10.1029/1999jb900248>
- Willett, S. D., & Brandon, M. T. (2002). On steady states in mountain belts. *Geology*, 30(2), 175–178. [https://doi.org/10.1130/0091-7613\(2002\)030<0175:ossimb>2.0.co;2](https://doi.org/10.1130/0091-7613(2002)030<0175:ossimb>2.0.co;2)
- Wolf, R. A., Farley, K. A., & Kass, D. M. (1998). Modeling of the temperature sensitivity of the apatite (U-Th)/He thermochronometer. *Chemical Geology*, 148(1–2), 105–114. [https://doi.org/10.1016/s0009-2541\(98\)00024-2](https://doi.org/10.1016/s0009-2541(98)00024-2)
- Yamada, Y., Yamashita, Y., & Yamamoto, Y. (2010). Submarine landslides at subduction margins: Insights from physical models. *Tectonophysics*, 484(1–4), 156–167. <https://doi.org/10.1016/j.tecto.2009.09.007>
- Zonenshain, L. P., & Pichon, X. (1986). Deep basins of the Black Sea and Caspian Sea as remnants of Mesozoic back-arc basins. *Tectonophysics*, 123(1–4), 181–211. [https://doi.org/10.1016/0040-1951\(86\)90197-6](https://doi.org/10.1016/0040-1951(86)90197-6)

References From the Supporting Information

- Galbraith, R. F., & Laslett, G. M. (1993). Statistical models for mixed fission track ages. *Nuclear Tracks*, 21, 459–470. [https://doi.org/10.1016/1359-0189\(93\)90185-c](https://doi.org/10.1016/1359-0189(93)90185-c)
- Gleadon, A. J. W. (1981). Fission track dating methods: What are the real alternatives? *Nuclear tracks* (Vol. 5, pp. 3–14).
- Hurford, A. J. (1990). Standardization of fission track dating calibration: Recommended by the Fission Track Working Group of the I.U.G.S. Subcommittee on geochronology. *Chemical Geology*, 80, 171–178. [https://doi.org/10.1016/0168-9622\(90\)90025-8](https://doi.org/10.1016/0168-9622(90)90025-8)
- Hurford, A. J., & Green, P. F. (1983). The Zeta-age calibration of fission track dating. *Isotope Geoscience*, 1, 285–317. [https://doi.org/10.1016/s0009-2541\(83\)80026-6](https://doi.org/10.1016/s0009-2541(83)80026-6)